E.O. Paton Electric Welding Institute of the National Academy of Science of Ukraine
International Association “Welding”

The Paton Welding Journal

11
2025

International Scientific-Technical and Production Journal ♦ Founded in January 2000 (12 Issues Per Year)

Address of Editorial Office:
E.O. Paton Electric Welding Institute, 11 Kazymyr Malevych Str., 03150, Kyiv, Ukraine
E-mail: office@paton.kiev.ua; https://paton.org.ua/en/

Address of Publisher:
International Association “Welding”, 11 Kazymyr Malevych Str., 03150, Kyiv, Ukraine
Tel.: (38044) 205 23 90, E-mail: patonpublishinghouse@gmail.com; journal@paton.kiev.ua
https://patonpublishinghouse.com/eng/journals/tpwj

The Journal was registered by the National Council of Ukraine on Television and Radio Broadcasting on 09.05.2024, carrier identifier R30-04569
ISSN 0957-798X (Print), ISSN 3041-2293 (Online)
DOI: https://doi.org/10.37434/tpwj, from #01, 2020 to now; DOI: https: //doi.org/10.15407/tpwj from #01, 2014 to #12, 2019.

Subscriptions, 12 issues per year:
348 Euro — annual subscription for the printed (hard copy) version, air postage and packaging included;
288 Euro — annual subscription for the electronic version (sending issues in pdf format or providing access to IP addresses).

Representative Offices of “The Paton Welding Journal”:

BRAZIL, Arc Dynamics
Address: Nova Iguacu, Rio de Janeiro, Brazil
Daniel Adolpho, Tel.: +55 21 9 6419 5703,
E-mail: dadolpho@arcdynamics.com.br

CHINA, China-Ukraine Institute of Welding, Guangdong Academy of Sciences
Address: Room 210, No. 363 Changxing Road, Tianhe, Guangzhou, 510650, China
Zhang Yupeng, Tel.: +86-20-61086791,
E-mail: patonjournal@gwi.gd.cn

BULGARIA, Bulgarian Welding Society
Address: Blvd. Asen Yordanov No.10, Sofia 1592, Bulgaria
Pavel Popgeorgiev, Tel.: +359 899 96 22 20,
E-mail: office@bws-bg.org

POLAND, PATON EUROPE Sp. z o. o.
Address: ul. Kapitałowa 4, 35-213, Rzeszów, Poland
Anton Stepakhno, Tel.: +38067 509 95 67,
E-mail: Anton.Stepakhno@paton.ua

The content of the Journal includes articles received from authors from around the world in the field of welding, cutting, cladding, soldering, brazing, coating, 3D additive technologies, electrometallurgy, material science, NDT and selectively includes translations into English of articles from the following journals, published in Ukrainian:

- «Avtomatychne Zvaryuvannya» (Automatic Welding), https://patonpublishinghouse.com/eng/journals/as;
- «Suchasna Elektrometalurhiya» (Electrometallurgy Today), https://patonpublishinghouse.com/eng/journals/sem;
- «Tekhnichna Diahnostyka ta Neruinivnyi Kontrol» (Technical Diagnostics & Nondestructive Testing), https://patonpublishinghouse.com/eng/journals/tdnk.

CONTENTS

ORIGINAL ARTICLES

*Translated Article(s) from “Avtomatychne Zvaryuvannya” (Automatic Welding), No. 5, 2025.

**Translated Article(s) from “Tekhnichna Diahnostyka ta Neruinivnyi Kontrol” (Technical Diagnostics & Nondestructive Testing), No. 3, 2025.

Indexing: The electronic edition of the Journal is stored in the V.I. Vernadsky National Library of Ukraine (eVerLib), included in the OPEN UKRAINIAN CITATION INDEX database and international databases: CROSSREF, EBSCO, Google Scholar, INDEX COPERNICUS, ULRICHSWEB.

DOI: https://doi.org/10.37434/tpwj2025.11.01

OPTIMIZATION OF THE PULSED CURRENT WAVEFORM AND PARAMETERS IN HFPC TIG WELDING

I. Krivtsun[1], **V. Demchenko**[1], **D. Nomirovskii**[2], **D. Kovalenko**[1], **U. Reisgen**[3], **O. Mokrov**[3], **R. Sharma**[3]

[1]E.O. Paton Electric Welding Institute of the NASU
11 Kazymyr Malevych Str., 03150, Kyiv, Ukraine
[2]Taras Shevchenko National University of Kyiv
60Volodymyrska Str., 01033 Kyiv, Ukraine
[3]RWTH Aachen University, ISF – Welding and Joining Institute
Pontstr. 49, 52062 Aachen, Germany

ABSTRACT

Experimental studies have shown that high-frequency pulsed modulation of welding current allows for an increase in penetration capacity of the welding process with tungsten electrode. This effect is attributed to intensified convective flows in the weld pool, excited by a high-frequency electromagnetic field. The article examines the problem of determining the shape and parameters of welding current pulses that maximizes the force exerted by the modulated current on the weld pool metal. The square of the effective value of the welding current is taken as an integral measure of the force action of the electromagnetic field on the molten metal of the weld pool. The difference between the squares of the effective and average values of the modulated current, which characterizes the excess of the force action of the arc with pulsed current modulation over the force action of the direct current arc, is taken as a criterion for optimizing the shape of the current pulse. The problem of variational calculus on finding such a current pulse shape, at which the maximum of the specified difference is achieved, is solved. Two optimization methods are considered: at a given modulation amplitude and at a given average value of the modulated current. It is rigorously shown mathematically that in the first case the optimal pulse shape is a square wave, in the second case — a rectangular current pulse, the duty cycle and amplitude of which are determined by the value of the maximum current of the welding generator. The optimization of parameters of current pulses of trapezoidal and triangular shapes generated by existing welding current generators has been carried out. The proposed theory can serve as a guideline in the development of effective pulse current generators, as well as in the design the modes of the tungsten inert gas welding process with high-frequency pulsed modulation of welding current in order to increase the penetration depth and improve welding productivity.

KEYWORDS: TIG welding, arc plasma, weld pool, electromagnetic force, direct current, pulsed current, mean and RMS values, wave form, duty cycle, amplitude, frequency

INTRODUCTION

In modern industrial production, the tungsten inert gas arc welding (TIG process) is used in the manufacture of critical structures in various industries. In order to increase the penetration ability of TIG welding, various activation methods are applied: the use of various shielding gases and their mixtures [1, 2], the application of special activating fluxes to the surface of the welded metal [3, 4], TIG welding in the keyhole mode (K-TIG process) [5], high-frequency pulse (HFP) modulation of the welding current [6–10]. Figure 1 shows the sections of welds obtained during TIG welding of a 5 mm thick plate made of 1.4301 (AISA 304) stainless steel using direct and modulated currents. Experimental conditions were as follows: arc length of 1.5 mm; direct current of 150 A, current modulation frequency of 6 kHz, average modulated current of 153 A, trapezoidal pulse shape with front duration of 55 μs; base current of 44 A, modulated current amplitude of 204 A.

With minor deviations of the average value of the modulated current and the average arc power from the corresponding parameters of direct current, the depth of penetration and the volume of molten metal during TIG welding with HFP modulation of the welding current (HFP TIG process) are noticeably greater than during TIG welding with direct current. A similar effect of increased penetration capacity of the HFP TIG process was also experimentally discovered earlier in works [7, 8, 10]. This effect can be explained by the fact that the effective value of the modulated current exceeds the direct current by 30 %.

The efficiency of high-frequency pulsed modulation of the arc current as a means of increasing the depth of penetration in TIG welding depends on such parameters as the shape of the current pulse, the duty cycle, the amplitude and the modulation frequency. With the optimal choice of these parameters, the force action of the electromagnetic field of the current on the metal of the weld pool is increased, the convective heat exchange in the molten metal is intensified, and thereby the penetration capacity of the arc with

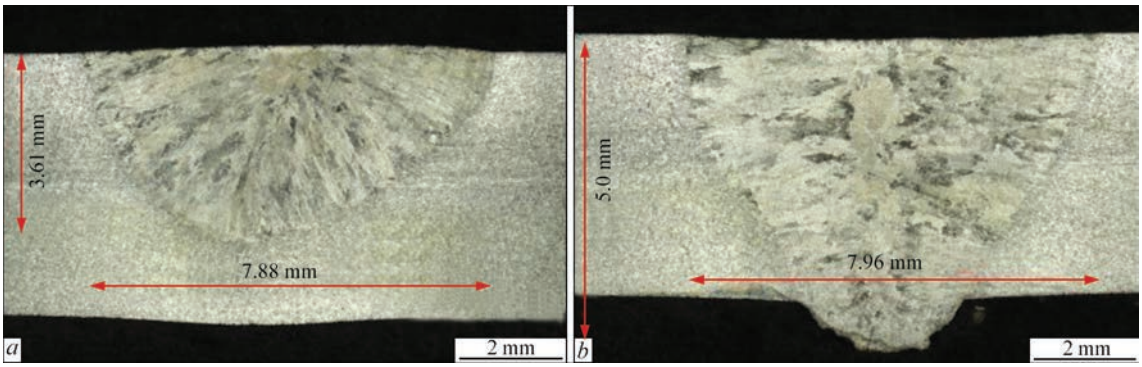

Figure 1. Shapes of welds in TIG welding. *a* — with direct current; *b* — with HFP modulation of the welding current

a refractory cathode increases. The purpose of this work is to determine the shape and parameters of the welding current pulses that are optimal according to the criterion of the maximum force action of the modulated current on the metal of the weld pool.

OPTIMIZATION OF THE SHAPE AND PARAMETERS OF CURRENT PULSES

We will assume that the modulated welding current $I(t)$ is unipolar ($I(t \geq 0)$ and periodically changing in time t with a period T. The average I_{av} and effective I_{eff} values of current are determined as follows: $I_{av} = \langle I(t) \rangle; I_{eff} = \sqrt{\langle I^2(t) \rangle}$, where $\langle f(t) \rangle = \frac{1}{T}\int_0^T f(t)dt$ is the integral average value of the periodic function $f(t)$ on the segment $t \in [0; T]$.

In work [11] it is shown that during TIG welding with HFP current modulation, the volume density of the electromagnetic force exciting the magnetohydrodynamics of the weld pool depends on the averaged value of the square of the current $\bar{I}^2(r, z)$ over one modulation period, flowing within a circle of radius r in an arbitrary axial section z of the pool. The greater the effective value of the modulated welding current I_{eff}, the greater its distributed characteristic $\bar{I}^2(r, z)$ and, accordingly, the greater the force effect of the modulated welding current on the molten metal. Therefore, as an integral measure of such effect, we will take the square of the effective value of the welding current. The force effect of the modulated current arc on the metal of the weld pool will be compared with the force effect of the direct current arc, equal in magnitude to the average value I_{av} of the modulated current.

Let $I_1 < I(t) < I^2$, $t \in [0; T]$, where I_1 is the base value of the current; $A = I_2 - I_1$ is the amplitude, T is the modulation period. On the segment [0; 1] of dimensionless time $\tau = \frac{t}{T}$, the law of current change can be written as:

$$I(\tau) = I_1 + A\eta(\tau), \qquad (1)$$

where $\eta(\tau)$ is the normalized shape of the current pulse.

We will consider in the general case, the set M of Lebesgue measurable functions as functions $\eta(\tau)$, such that $0 \leq \eta(\tau) \leq 1$, $\tau \in [0; 1]$. For the squares of the effective and average values of the modulated current, the following expressions hold:

$$\begin{aligned} I_{eff}^2 &= I_1^2 + 2AI_1\langle \eta(\tau) \rangle + A^2 \langle \eta^2(\tau) \rangle; \\ I_{av}^2 &= I_1^2 + 2AI_1\langle \eta(\tau) \rangle + A^2 \langle \eta(\tau) \rangle^2. \end{aligned} \qquad (2)$$

Subtracting the right- and left-hand parts of equalities (2), we obtain

$$\Delta = I_{eff}^2 - I_{av}^2 = A^2\left(\langle \eta^2(\tau) \rangle - \langle \eta(\tau) \rangle^2\right). \qquad (3)$$

Consider the problem of finding the normalized pulse shape $\eta(\tau) \in M$, which provides $\max\limits_{\eta(\tau)\in M} \Delta$. Two formulations of such a problem are possible. In the first one we assume that current pulses (1) are generated by normalized shapes of $\eta(\tau)$, as long as amplitude A remains constant and independent on the pulse shape $\eta(\tau)$. In this case, it follows from (3) that the optimal shape of the current pulse $\eta(\tau)$ delivers a maximum to the functional $\Phi[\eta(\tau)] = \int_0^1 \eta^2(\tau)d\tau - \left(\int_0^1 \eta(\tau)d\tau\right)^2$.

The following assertion holds

THEOREM

Let $\eta(\tau) \in M$ be the normalized shape of the current pulse such that for all $\tau \in [0; 1]$ the following inequalities hold $0 \leq \eta(\tau) \leq 1$. Then, $\Phi[\eta(\tau)] \leq \frac{1}{4}$, and equality is achieved if and only if there exists measurable set $B \subset [0; 1]$, $\mu(B) = \frac{1}{2}$, where μ is the Lebesgue measure on a straight line, such that the following equalities hold for almost all $\tau \in [0; 1]$

$$\eta(\tau) = \begin{cases} 1, & \tau \in B; \\ 0, & \tau \notin B. \end{cases} \qquad (4)$$

PROOF

As long as $0 \le \eta(\tau) \le 1$, the inequality $\langle\eta^2(\tau)\rangle \le \langle\eta(\tau\rangle$ holds. Hence, $\Phi[\eta(\tau)] \le \langle\eta(\tau\rangle - \langle\eta(\tau\rangle^2$. Function $\langle\eta(\tau\rangle - \langle\eta(\tau\rangle^2$ reaches its maximum at $\langle\eta(\tau)\rangle = \frac{1}{2}$, and this maximum is equal to $\frac{1}{4}$. Thus, $\Phi[\eta(\tau)] \le \frac{1}{4}$. In the latter condition, the equality is achieved if and only if $\langle\eta(\tau)\rangle = \langle\eta^2(\tau)\rangle = \frac{1}{2}$. Condition $\langle\eta(\tau\rangle = \langle\eta^2(\tau\rangle$ implies that for almost all $\tau \in [0; 1]$ the following equality holds: $\eta(\tau) = \eta^2(\tau)$. Hence, $\eta(\tau) = 0$ or $\eta(\tau) = 1$ for almost all $\tau \in [0; 1]$. Let $B \subset [0; 1]$ be a set of such values of $\tau \in [0; 1]$ that $\eta(\tau) = 1$. Now we have $\langle\eta(\tau)\rangle = \int_0^1 \eta(\tau)\, d\tau = \mu(B)$. Taking into account the equality $\langle\eta(\tau)\rangle = \frac{1}{2}$, we obtain $\mu(B) = \frac{1}{2}$, i.e. equalities (4) are true. It suffices to note that equality $\Phi[\eta(\tau)] = \frac{1}{4}$ is valid for the found function $\eta(\tau)$. The theorem is proved.

The considered problem about the maximum of functional $\Phi[\eta(\tau)]$ in the class of Lebesgue measurable functions has a non-unique solution, and there are infinitely many equivalent functions $\eta(\tau)$ such that the sets of points of [0;1] for which $\eta(\tau) = 0$ and $\eta(\tau) = 1$, have the same Lebesgue measure $\mu(B) = \langle\eta(\tau)\rangle = \frac{1}{2}$. In practical applications of pulsed modulation of welding current, function $\eta(\tau)$ in the form of a unit jump (rectangular pulses in the form of a square wave) is of greatest interest

$$\eta(\tau) = \begin{cases} 1, & 0 \le \tau < \frac{1}{2}; \\ 0, & \frac{1}{2} \le \tau \le 1; \end{cases} \quad \Delta_1 = \frac{1}{4}A^2. \qquad (5)$$

The optimum shape of current pulse (5), determined at fixed modulation amplitude A, leaves arbitrariness in the average and effective current values. To eliminate it, we must additionally set another current parameter, for example, value of base current I_1. In this case, $I_{av} = I_1 + \frac{1}{2}A$, $I_{eff} = \sqrt{I_{av}^2 + \frac{1}{4}A^2}$, and the expression for Δ_1 can be written in the following form $\Delta_1 = \widehat{I}_{av}^2$, where $\widehat{I}_{av} = I_{av} - I_1$.

Let us consider another possibility of finding $\max_{\eta(\tau)\in M} \Delta = \Delta_2$ without the assumption that current modulation amplitude A is fixed. Instead, in (1) we will assume that current pulses $I = I(\tau)$ are generated, provided the current value $\widehat{I}_{av}$ is kept constant at all $\eta(\tau) \in M$. If I_1 is given this method of current pulse shape optimization is convenient for assessment of the effectiveness of force action of modulated current, compared to the impact of direct current equal to I_{av}.

With this approach of optimization, the current amplitude becomes dependent on pulse shape and, as it follows from (1), this dependence has the form of $A[\eta(\tau)] = \frac{\widehat{I}_{av}}{\langle\eta(\tau)\rangle}$. Then, $\Delta = \widehat{I}_{av}^2 \frac{\langle\eta^2(\tau)\rangle - \langle\eta(\tau)\rangle^2}{\langle\eta(\tau)\rangle^2}$ and the problem arises of finding the maximum of functional $F[\eta(\tau)] = \left[\int_0^1 \eta^2(\tau)d\tau \Big/ \left(\int_0^1 \eta(\tau)d\tau\right)^2 - 1\right]$ in the class of functions $\eta(\tau) \in M$.

We denote by $M_\delta \subset M$ the subset of such functions $\eta(\tau)_\delta \in M$, for which $\langle\eta_\delta(\tau\rangle = \delta$, where $\delta \in [0; 1]$ is a certain fixed parameter. It is obvious that $\bigcup_{\delta\in[0;1]} M_\delta = M$. Similarly to the proof of the theorem, the estimate $F[\eta_\delta(\tau)] \le \frac{1}{\delta} - 1$ is valid, and the equality holds for those and only for those functions $\eta_\delta(\tau) \in M_\delta$ for which a measurable set $B_\delta \subset [0; 1]$, $\mu(B_\delta) = \delta$ exists, such that equalities (4) hold for almost all $\tau \in [0; 1]$. For example, function

$$\eta_\delta(\tau) = \begin{cases} 1, & 0 \le \tau < \delta; \\ 0, & \delta \le \tau \le 1, \end{cases} \qquad (6)$$

delivers maximum to functional $F[\eta_\delta(\tau)]$ and defines the pulses of a rectangular shape with duty cycle δ.

In welding generators, the maximum possible current is limited by the maximum current of the generator. In this connection, we will further assume $A[\eta(\tau)] \le A_{max}$. This condition, given the selected value $\widehat{I}_{av}$, imposes a lower limit on $\langle\eta(\tau)\rangle$, i.e.: $\langle\eta(\tau)\rangle \ge \frac{\widehat{I}_{av}}{A_{max}} = \delta_{min}$. Thus for $\eta_\delta(\tau) \in M_\delta$ inequality $\delta \ge \delta_{min}$ holds, and, therefore, $\max_{\eta_\delta\in M_\delta} F[\eta_\delta(\tau)]$ is achieved on functions $\eta_\delta(\tau) \in M_\delta$ when $\delta \ge \delta_{min}$, and this maximum is equal to $\frac{1}{\delta_{min}} - 1$. Then, for maximum difference of the squares of effective and average values of modulated current in the second optimization method, we have

Table 1. Optimal parameters of current modulation by rectangular pulses at different (set) values of $\widehat{I}_{av}$

$\widehat{I}_{av}$, A	50	100	150	200	250	300	350	400
δ_{min}	0.1	0.2	0.3	0.4	0.5	0.6	0.7	0.8
I_{eff}, A	158	224	274	316	354	387	418	447
Δ^2, 10^3 A^2	22.5	40.0	52.5	60.0	62.5	60.0	52.5	40.0

$$\Delta_2 = \widehat{I}_{av}^2\left(\frac{1}{\delta_{min}} - 1\right). \qquad (7)$$

It means that the optimum method of current modulation at the set values of average I_{av} and base I_1 current is modulation by rectangular pulses with minimum possible duty cycle δ_{min} for the set value of $\widehat{I}_{av}$ at the selected value of A_{max}. It follows from the alternative form of writing expression (7) $\Delta_2 = \widehat{I}_{av}\left(A_{max} - \widehat{I}_{av}\right)$ that the right-hand side of this equality has a maximum, which is achieved with $\widehat{I}_{av} = \frac{1}{2}A_{max}$, $\delta_{min} = 0.5$ that corresponds to pulses in the form of a meander (5).

Let us give numerical estimates of optimal parameters of rectangular current pulses, assuming A_{max} = 500 A (maximum power source current in [8]). Table 1 gives the calculated data on the change of the minimum possible value of duty cycle δ_{min}, effective current value I_{eff}(at I_1 = 0), as well as maximum difference Δ_2 of the squares of the effective and average current values, depending on the value of $\widehat{I}_{av}$.

Figure 2 shows a comparison of two methods of optimization of the shape and parameters of current pulses, considered above: 1) at fixed modulation amplitude $A \le A_{max}$ = 500 A (dashed curve); 2) at fixed current $\widehat{I}_{av}$ and given above maximum amplitude value (solid curve). Note that in the first case at $\widehat{I}_{av} > \frac{1}{2}A_{max}$, current modulation amplitude A exceeds the accepted restriction, therefore we will perform comparison of the above optimization methods in the domain of $\widehat{I}_{av} \le 250$ A.

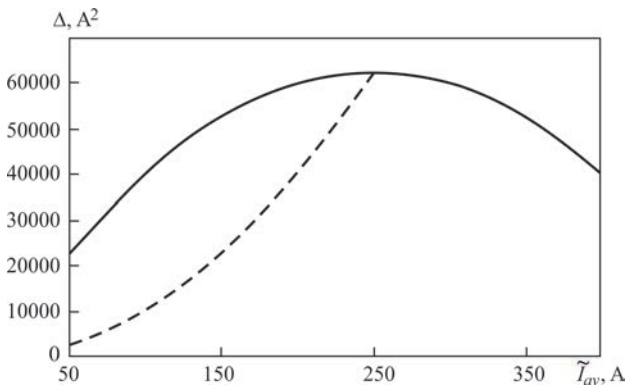

Figure 2. Change of (dashed curve) and (solid curve), depending on at A_{max} = 500 A

It follows from the calculated data presented in this Figure that excess of force action of modulated current over the impact of direct current, equal to average value of modulated current, is significantly higher with the second method of optimization, and both the variants become equivalent only in the point of maximum ($\widehat{I}_{av}$ = 250 A).

As it follows from the definition of $\widehat{I}_{av}$ $I_{av} - I_1$, increase of base current at constant average value of current leads to decrease of $\widehat{I}_{av}$ and to decrease of Δ_1, Δ_2 in the domain of $\widehat{I}_{av} \le 250$ A, respectively (see Figure 2), thus lowering the effectiveness of force impact of modulated current.

OPTIMIZATION OF PARAMETERS OF TRAPEZOIDAL AND TRIANGULAR CURRENT PULSES

The creation of arc power sources with high-frequency current modulation, which are capable of generating rectangular pulses in a wide frequency range, is a complex engineering task [8, 12]. In this case, the rate of current rise/fall at the pulse fronts that can actually be achieved in the welding circuit is of the order of 20–50 A/μs, which, for example, with a current modulation amplitude of 500 A will correspond to a total front duration of the order of 20–50 μs. Therefore, for practical applications, it is of interest to consider current pulses of trapezoidal and, as a special case, triangular shape, which can potentially be implemented using existing welding power sources for TIG welding with HFP current modulation.

Let us first consider a trapezoidal current pulse, shown in Figure 3, with the following time parameters: t_1 — duration of the leading edge; $t_2 - t_1$ — duration of the "peak" of the pulse;$t_3 - t_2$ — duration of the trailing edge; t_3 — pulse duration; $T - t_3$ — pause duration.

We will put dimensionless parameters $\tau_1 = \frac{t_1}{T}$, $\tau_2 = \frac{t_2}{T}$, $\tau_3 = \frac{t_3}{T}$ into correspondence with the dimensional time parameters of the pulse and will introduce the following designations: $\tau_{21} = \tau_2 - \tau_1$ — dimensionless duration of the "peak"; $\tau_f = \tau_1 + \tau_3 - \tau_2$ — total dimensionless duration of the pulse fronts.

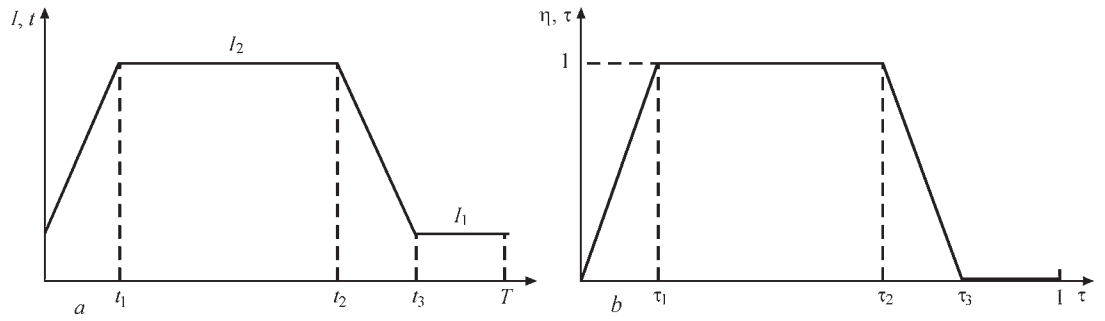

Figure 3. Trapezoidal current pulse (*a*) and its normalized form (*b*)

For the normalized form of a trapezoidal current pulse it is easy to obtain: $\langle\eta(\tau)\rangle = \tau_{21} + \frac{\tau_f}{2}$; $\langle\eta^2(\tau)\rangle = \tau_{21} + \frac{\tau_f}{3}$. These expressions depend only on the total dimensionless duration of the fronts. As before, we will consider two options for optimizing the pulse parameters.

Let us first assume that the trapezoidal current pulses are generated at fixed modulation amplitude A. Then, $\Phi(\tau_{21}, \tau_f) = \tau_{21} + \frac{\tau_f}{3} - \left((\tau_{21} + \frac{\tau_f}{2})^2\right)$ function of dimensioless time parameters τ_{21}, τ_f corresponds to $\Phi[\eta(\tau)]$ functional. For a given value of τ_f, which is determined by the characteristics of the power source, $\max\limits_{\tau_{21}} \Phi(\tau_{21}, \tau_f) = \frac{1}{4} - \frac{\tau_f}{6}$ is achieved at

$$\tau_{21} = \frac{1}{2}(1 - \tau_f). \tag{8}$$

The maximum excess of the force action of a trapezoidal pulse over the force action of a direct welding current equal to I_{av} is determined by the value

$$\Delta_1 = \frac{A^2}{4}\left(1 - \frac{2}{3}\tau_f\right). \tag{9}$$

Note that for $\tau_f = 0$ (rectangular pulses) formula (9) corresponds to (5).

A triangular pulse is a special case of a trapezoidal pulse. In the expressions for $\langle\eta(\tau)\rangle$, $\langle\eta^2(\tau)\rangle$ we set $\tau_{21} = 0$, and we will identify τ_f with the duration of the triangular pulse. As a result we get: $\Phi(\tau_f) = \frac{1}{3}\tau_f - \frac{1}{4}\tau_f^2$. Analyzing this function for the extremum, we find that $\max\limits_{\tau_f} \Phi(\tau_f) = \frac{1}{9}$ is reached at $\tau_f = \frac{2}{3}$.

This means that a triangular current pulse is optimal if two-thirds of the period are taken by the pulse itself (leading and trailing edges), and one-third is the pause. The maximum excess of the force action of such a pulse over the force action of a direct current equal to $\hat{I}_{av}$, is determined by the value

$$\Delta_1 = \frac{A^2}{9}. \tag{10}$$

Let us now assume that the trapezoidal current pulses are generated at fixed values of I_{av} and I_1, i.e. the value of $\hat{I}_{av}$ is kept constant, and let us accept the constraint of $A \le A_{\max}$. Similarly to what was done in Section 1, it can be shown that for trapezoidal pulses $\max\left(I_{eff}^2 - I_{av}^2\right)$ is achieved at the minimum possible duty cycle $\delta_{\min} = \frac{av}{\max} + -\tau$ and is

$$\Delta_2 = \hat{I}_{av}^2\left[\frac{\delta_{\min} - 2\tau_f/3}{\left(\delta_{\min} - \tau_f/2\right)^2} - 1\right].$$

Table 2. Optimal parameters of current modulation by trapezoidal and triangular pulses at different values of $\hat{I}_{av}$

$\hat{I}_{av}$, A		50	100	150	200	250	300	350
Trapezoidal pulses	$\delta_{\min}$	0.25	0.35	0.45	0.55	0.65	0.75	0.85
	I_{eff}, A	112	194	250	296	332	371	403
	Δ_2, 10^3 A^2	10.0	27.5	40.0	47.5	50.0	47.5	40.0
Triangular pulses	$\delta_{\min}$	0.2	0.4	0.6	0.8	1.0	–	–
	I_{eff}, A	129	180	224	258	289	–	–
	Δ_2, 10^3 A^2	14.17	22.33	27.50	26.67	20.83	–	–

Table 3. Optimal parameters of rectangular, trapezoidal and triangular current pulses for two optimization methods.

Current pulse shape	A = const		$\hat{I}_{av}$ = const, $A \le A_{\max}$	
	δ	Δ_1	δ	Δ_2
Rectangular pulses	$\frac{1}{2}$	$\frac{1}{4}A^2$	$\frac{\hat{I}_{av}}{A_{\max}}$	$\hat{I}_{av}^2\left(\frac{1}{\delta}-1\right)$
Trapezoidal pulses	$\frac{1}{2}(1+\tau_f)$	$\frac{A^2}{4}\left(1-\frac{2}{3}\tau_f\right)$	$\frac{\hat{I}_{av}}{A_{\max}}+\frac{1}{2}\tau_f$	$\hat{I}_{av}^2\left[\frac{\delta-2\tau_f/3}{\left(\delta-\tau_f/2\right)^2}-1\right]$
Triangular pulses	$\frac{2}{3}$	$\frac{A^2}{9}$	$\frac{2\hat{I}_{av}}{A_{\max}}$	$\hat{I}_{av}^2\left[\frac{4}{3\delta}-1\right]$

At $\tau_f = 0$, the resulting expression coincides with formula (8) for rectangular pulses. In the case of triangular pulses, the expressions for Δ_2 and $\Delta_{\min}$ take the form of

$$\Delta_2 = \hat{I}_{av}^2\left[\frac{4}{3\delta_{\min}}-1\right], \delta_{\min} = \frac{2\hat{I}_{av}}{A_{\max}}.$$

Table 2 shows the quantitative characteristics of the optimal parameters of trapezoidal and triangular current pulses, calculated for $A_{\max}$ = 500 A, $I_1 = 0, \tau f = 0.3$.

The theory presented remains valid for current pulses whose normalized form does not depend on the modulation frequency (isomorphic pulses). The force effect of modulated current with non-isomorphic trapezoidal pulses (for example, with a fixed front duration) decreases with increasing modulation frequency.

CONCLUSIONS

1. In TIG welding, the difference between the squares of the effective and average values of the modulated current can be taken as an approximate measure of the excess of the force effect of the modulated welding current over the effect of direct current. The maximum of this difference serves as a criterion for optimizing the shape of the welding current pulses, ensuring the maximum force effect of the modulated current on the metal of the weld pool and, as a consequence, increasing the penetration capacity of the arc in TIG welding with high-frequency pulse current modulation.

2. The optimal shapes and parameters of welding current pulses defined in Section 1 for the general case of functions $\eta(\tau) \in L_1(0.1)$ form equivalence classes in which the seminorms of the elements included in them coincide. The mean value $\langle\eta(\tau)\rangle$ of the normalized pulse shape, which is equal to 0.5 for the conditions of the theorem, acts as $\|\eta\|$. In the equivalence class with $\langle\eta(\tau)\rangle = \frac{1}{2}$, in addition to square wave pulses with a frequency of F, it is possible to consider options for modulating the current with a finite number of subpulses such that their total relative duration is equal to 0.5, for example, rectangular pulses with frequencies nF, where $n > 1$ is an integer. Similarly, in the second optimization method, the value $\langle\eta(\tau)\rangle = \delta_{\min}$ can be achieved by generating a finite number of subpulses whose total relative duration is equal to $\delta_{\min}$. Such options are indistinguishable from the point of view of the considered integral criterion of force impact $I_{eff}^2 - I_{av}^2$.

3. Expressions for the parameters of optimal rectangular, trapezoidal and triangular current pulses are summarized in Table 3.

These parameters can serve as a guideline for designing welding modes, as well as for developing more advanced pulse current generators capable of providing increased penetration capacity of the HF TIG process.

4. When conducting experimental studies of the penetration capacity of modulated current and unambiguous interpretation of their results, it is important to use pulse current generators stabilized by a normalized pulse shape in a wide frequency range. In many existing modulated current generators, pulse shape stabilization is maintained only in a limited frequency range. Therefore, when analyzing the effect of current modulation frequency on the penetration capacity of the arc in TIG welding, it is necessary to take into account not only the modulation frequency, but also the change in the pulse shape depending on their repetition frequency. Attention to this was first drawn in [6].

REFERENCES

1. Lucas, W. (1992) Shielding gases for arc welding — Part I. *Welding and Metal Fabrication,* **6**, 218–225.
2. Lu, S., Fujii, H., Nogi, K. (2004) Marangoni convection and weld shape variations in Ar–O_2 and Ar–CO_2 shielded GTA welding. *Materials Sci. and Eng. A*, 380(**1–2**), 290–297.

3. Lucas, W. (2000) Activating flux — Improving the performance of the TIG process. *Welding and Metal Fabrication*, **2**, 7–10.
4. Yushchenko, K.A., Kovalenko, D.V., Kovalenko, I.V. (2001) Application of activators for TIG welding of steels and alloys. *The Paton Welding J.*, **7**, 37–43.
5. Jarvis, B., Ahmed, N. (2000) Development of keyhole mode gas tungsten arc welding process. *Sci. and Techn. of Welding and Joining*, 5(**1**), 1–7.
6. Omar, A.A., Lundin, C.D. (1979) Pulsed plasma — Pulsed GTA arcs: A study of the process variables. *Welding J., Res. Suppl.*, **4**, 97s–105s.
7. Saedi, H.R., Unkel, W. (1988) Arc and weld pool behavior for pulsed current GTAW. *Welding J., Res. Suppl.*, **11**, 247s–255s.
8. Onuki, J., Anazawa, Y., Nihei, M. et al. (2002) Development of a new high-frequency, high-peak current power source for high constricted arc formation. *Jpn. J. Appl. Phys.*, **41**, 5821–5826.
9. Qi, B.J., Yang, M.X., Cong, B.Q. et al. (2013) The effect of arc behavior on weld geometry by high-frequency pulse GTAW process with 0Cr18Ni9Ti stainless steel. *Int. J. Adv. Manuf. Technol.*, **66**, 1545–1553.
10. Yang, M., Yang, Z., Cong, B. et al. (2014) A study on the surface depression of the molten pool with pulsed welding. *Welding J., Res. Suppl.*, 93(**8**), 312s–319s.
11. Krivtsun, I., Demchenko, V., Krikent, I. et al (2024) Comparative numerical analysis of electromagnetic forces in DC and HFPC TIG welding. *Applied Mathematical Modelling*, **127**, 366–378.
12. Yang, M., Yang, Z., Qi, B. (2015) The effect of pulsed frequency on the plasma jet force with ultra high frequency pulsed arc welding. *Welding in the World*, **8**, 875–882.

ORCID
I.V. Krivtsun: 0000-0001-9818-3383,
V. Demchenko: 0009-0007-7785-1523,
D. Nomirovskii: 0000-0001-9482-776X
D. Kovalenko: 0000-0002-8544-588X,
U. Reisgen: 0000-0003-4920-2351,
O. Mokrov: 0000-0002-9380-6905,
R. Sharma: 0000-0002-6976-4530

CONFLICT OF INTEREST
The Authors declare no conflict of interest

CORRESPONDING AUTHOR
D. Kovalenko
E.O. Paton Electric Welding Institute of the NASU
11 Kazymyr Malevych Str., 03150, Kyiv, Ukraine.
E-mail: d_v_kovalenko@ukr.net

SUGGESTED CITATION
I. Krivtsun, V. Demchenko, D. Nomirovskii, D. Kovalenko, U. Reisgen, O. Mokrov, R. Sharma (2025) Optimization of the pulsed current waveform and parameters in HFPC TIG welding. *The Paton Welding J.*, **11**, 3–9.
DOI: https://doi.org/10.37434/tpwj2025.11.01

JOURNAL HOME PAGE
https://patonpublishinghouse.com/eng/journals/tpwj

Received: 12.05.2025
Received in revised form: 24.07.2025
Accepted: 11.11.2025

DOI: https://doi.org/10.37434/tpwj2025.11.02

RESEARCH INTO TECHNOLOGICAL PROCESSES OF TREATMENT OF METALS, ALLOYS AND WELDED JOINTS USING ELECTROMAGNETIC FIELD (REVIEW)

L.M. Lobanov[1], L.I. Nyrkova[1], M.O. Pashchyn[1], O.L. Mikhodui[1], O.M. Tymoshenko[1], N.L. Todorovych[1], O.M. Syzonenko[3], I.P. Kondratenko[2], V.V. Chopyk[2], O.M. Karlov[2]

[1] E.O. Paton Electric Welding Institute of the NASU
11 Kazymyr Malevych Str., 03150, Kyiv, Ukraine
[2]Institute of Electrodynamics of the NASU
56 Beresteiskyi Prosp., 03057, Kyiv, Ukraine
[3]Institute of Pulse Processes and Technologies of the NASU
43a Bohoyavlensky Prosp., 54018, Mykolaiv, Ukraine

ABSTRACT

An analysis of promising technologies for improving the mechanical characteristics and the stress states of metal materials and welded joints based on the use of electromagnetic fields and their derivatives, such as electrodynamic pressure force, eddy currents, and shock waves, was carried out. The process of electrohydropulse treatment by high-energy discharge (EPT HED EHIPD) using a hydrocarbon liquid for the production of polydisperse mixtures used for alloying the weld metal of welded joints as part of flux-cored wires is considered. The positive effect of micro-additives of the Ti–TiC system modifier obtained by EPT HED on the operational properties of the deposited metal of the 25Kh5FMS tool steel type was determined. It is shown that treatment with a pulsed electromagnetic field (PEMF) improves the residual stress states of welded joints. New process diagrams for the application of electrodynamic treatment (EDT) of welded joints are considered. The advantages of PEMF and EDT of the weld metal in the welding process in comparison with treatment at room temperature are proved. The mechanism of surface hardening of 25KhGNMT steel as a result of its pulsed barrier discharge treatment (PBD) was investigated. It is proved that the PBD increases the dislocation density and disperses the microstructure, which has a positive effect on the mechanical characteristics of steel. The prospects for the use of PBD for non-destructive testing of residual stress states of welded joints are considered.

KEYWORDS: welded joint, electromagnetic field treatment, electrodynamic treatment, residual stresses, fusion welding, surface hardening, titanium carbide, polydisperse mixtures, residual deformations, aluminium alloys, structural steels, dislocation density

INTRODUCTION

The development of high-tech engineering industries stimulates the development of new technologies for extending the service life of welded structures based on the use of advanced electrophysical phenomena, including electromagnetic fields, electric currents of various configurations and electrodynamic forces. The research results give reason to believe that new technologies for treatment of welded structures can be based on the principles of controlling the mechanical properties of metal alloys and welded joints using electrophysical phenomena [1, 2].

THE AIM

of the study is to analyse promising technologies for improving the mechanical characteristics and stress state of metal alloys and welded joints based on the use of electromagnetic fields and their derivatives (electrodynamic pressure force, eddy currents, shock waves, etc.).

A high-voltage pulse discharge in a conductive liquid is used in the industrial technology of electrohydropulse treatment as a source of dynamic pressure, under the effect of which the materials being treated can change their size, structure and mechanical characteristics. Such treatment involves the impact of a dynamic load on the object initiated by a high-voltage electric discharge of a pulsed electric current in an aqueous medium. This is a cyclic process characterized by the release of energy in the discharge channel within microseconds and accompanied by the action of compression waves (which under certain conditions are transformed into shock waves), powerful hydroflows, cavitation, electromagnetic and thermal fields. Studies of the impact of the mentioned treatment on the stress-strain state of welded joints have shown that it reduces tensile stresses in welded structures by up to 90 % [3]. However, the technologies of such high-voltage electric discharge treatment have not been widely used in metal-working because of the

low process performance and significant metal and energy consumption of the equipment.

The use of electrohydropulse treatment with a high-voltage electric discharge using a hydrocarbon liquid (instead of water) for the production of polydisperse mixtures containing nanoparticles with special properties used for alloying the weld metal of welded joints is promising. This treatment variant allows implementing an energy-efficient method of grinding metal alloys — discharge-pulse preparation of powders by using a high-voltage electric discharge in the liquid-powder dispersion system. Its cyclic action enables fine grinding by pressure waves due to the formation of a large number of defects in the powder, which helps to reduce the energy of crystal destruction, the formation of a large number of active centres and facilitates chemical interaction between the elements of the system under conditions of dynamic loading. The use of a hydrocarbon liquid as a working medium under such processing of powder mixtures not only provides elimination of their oxidation, but also creates thermodynamic conditions for the pyrolysis of kerosene with the formation of solid-phase carbon, which is capable of entering into carbidization reactions with powder particles, forming nanostructured strengthening phases [4, 5].

For electrohydropulse treatment with high-voltage electric discharge [4, 5], specialized equipment is used, which, in addition to the power source, includes a chamber — a container, where the powder grinding process takes place and which must withstand significant dynamic and thermal loads (Figure 1).

To investigate the efficiency of using polydisperse mixtures produced by this treatment, the weld metal was alloyed with Al- and Ni-based alloys, into the melts of which powders were introduced.

The introduction of 0.01 wt.% of the Ti–TiC modifier, synthesized by this treatment of Ti-powder in kerosene and briquetted by spark plasma sintering, made it possible to reduce the grain size from 1–2 to 0.2–0.6 mm in all modified specimens of the Ni-based heat-resistant SM88U alloy [6]. Under these conditions, the ultimate tensile strength at 900 °C and long-term strength increased by 20 %. This indicates the prospects of using metal powders after treatment with a high-voltage electric discharge to modify the cast structure of welds of nickel alloy structures operating at elevated temperatures, as well as the effect of the Ti–Al–C system modifier after appropriate synthesis on the structure refinement and improvement of the properties of welded joints made of aluminium $AK7_{pch}$ (A357) alloy for the body parts of marine engines [7].

Polydispersed mixtures produced by applying a high-voltage electric discharge are used as part of the

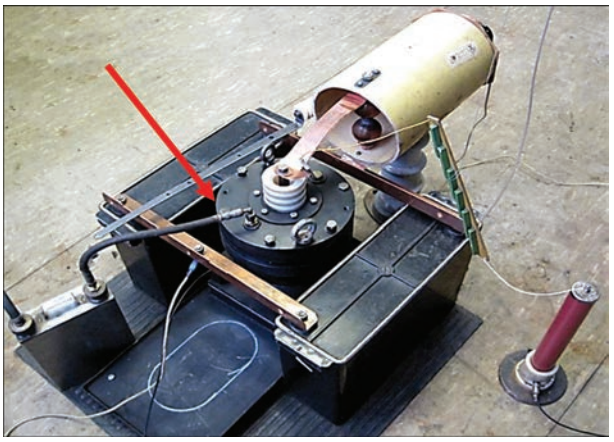

Figure 1. Appearance of equipment for electrohydropulse treatment using high-voltage electric discharge, where the arrow indicates the chamber in which powder grinding takes place [6]

charge of flux-cored wires for arc surfacing. This simplifies the process of introducing the powder into the weld pool during the phase of the filler liquid metal transfer. The positive effect of micro-additives of the Ti–TiC system modifier on the operational properties of the deposited metal of the 25Kh5FMS tool steel type has been determined. The modifying powders of the Ti–TiC system were produced by the above treatment of Ti-powder in kerosene. The modification of the deposited metal with Ti-carbides in the amount of ≈ 0.01 % does not deteriorate the quality of the formation of deposited beads and slag crust detachment. The introduction of micro-additives of Ti carbides in the amount of 0.01 % to the deposited metal leads to an increase in its heat and wear resistance under conditions of elevated temperatures by 15–50 %, depending on the type of used modifying additive [8]. The effect of boron and titanium carbides modifying the boron additives introduced in the same amount into the charge of PP-Np-25Kh5FMS powder electrode wire on the structure and properties of the deposited metal was compared. It is shown that the introduction of additives of both types of modifiers in the amount of 0.01 % significantly affects the structure of the deposited metal, and their effect on the structure is different. It was found that modification with boron leads to a significant reduction in the size of crystallites, redistribution of non-metallic inclusions, and an increase in the microhardness of the metal. The introduction of titanium carbide micro-additives into the weld pool affects the kinetics of metal crystallisation, which provides elimination of the columnar structure of crystallites and its transformation into a cellular structure. It has been shown that due to these structural changes, the wear resistance and heat resistance of the metal deposited using both types of modifiers increase [9].

The obtained results help to improve the characteristics of materials for surfacing parts of special equipment operating under conditions of abrasive

wear and cyclic thermomechanical loads. Thus, the use of polydisperse mixtures produced by a high-voltage electric discharge in a hydrocarbon liquid creates a new direction for optimizing the mechanical properties of deposited structural elements.

Based on the results of research in the field of materials science, the phenomenon of improving the ductility of a metal due to its active loading at the time of passing (through the metal) a high-density electric current pulse j ($j \geq 1.0$ kA/mm^2) was established. The phenomenon is called the electroplastic effect, and the deformation initiated by it is called electroplastic [10]. The practical use of this effect has opened up new opportunities for metal-working and welding technologies [11]. The accompanying heating with a pulsed electric current treatment ($j \geq 1.0$ kA/mm^2) of structural steel specimens that were previously subjected to uniaxial elastic tension leads to tensile stress relaxation [12]. However, under heating conditions without the use of such a current, the tensile stresses in the specimen returned to their initial level after cooling to room temperature. The effect from the pulses action decreased with an increase in their number. From the point of view of electron-dislocation interaction, this is explained by the fact that a single current pulse acts on a material with a significant dislocation potential. Under the conditions of repeated impact of electric current pulses, the previous pulses remove some dislocations from the relaxation processes and the electroplastic strain decreases as a result of the electroplastic effect [13].

Changing the polarity of current pulses also affects the manifestation of this effect, and with the same amplitude (when studying a loaded specimen), bipolar pulses cause a smaller relaxation (jump) of stresses than monopolar ones [14], since electric current pulses of different polarity, initiating the movement of dislocations in opposite directions, counteract each other and their resulting effect is smaller than under conditions of monopolar electric current pulses. Their effect on the metal occurs in the plastic deformation area, accompanied by the release of the deforming force, while in the elastic deformation region, the electroplastic effect is not observed. Paper [15] discusses the mechanism by which stress relaxation is possible in the elastic region of loads and is caused by the action of current pulses. In [16], a procedure was developed for determining the part of the energy of ECP current pulses that is spent on the operation of electroplastic deformation.

Based on the results of studies of the electromagnetic effect of pulsed current on the mechanical characteristics of metals and alloys, technological processes of metal-working have been developed. Changes in the duration and energy of such a current and pulsed electromagnetic field lead to the activation of a spectrum of dislocation, phase and other physical processes, i.e., it becomes possible to control the mechanical characteristics of metals and alloys. Both electromagnetic effects implemented in various metal-working technologies cause structural changes in metals and alloys [17–19], which affect their mechanical characteristics. An increase in tool wear resistance [20], corrosion resistance [21–23], reduction in stress concentration [24], elimination of fatigue cracks, and extension of service life of parts made of light and special alloys [25] are noted. It has been found that at optimal values of the pulsed electric current parameters, the tensile strength of material, endurance limit, and durability increase without reducing the ductile properties of the material [26].

Analysing the abovementioned, it should be noted that the effects of pulsed electric current and pulsed electromagnetic field can be used to improve the mechanical characteristics and extend the service life of welded joints, which are also covered by the results [17–26] obtained for metals and alloys.

The study of stress relaxation features in metals and alloys caused by electric current pulses and pulsed electromagnetic field treatment is a promising area of engineering practice for control of residual stress states of welded structures. The effect of a pulsed field on reducing residual stresses in butt welded joints of the aluminium AMg6 alloy was investigated. A system of two plane inductors rigidly fixed on the same vertical axis on the outer and back surfaces of the weld was used. The welded joint to be treated, the inductor system, and the pulsed field generator (capacitive energy storage) are part of the discharge circuit [27]. The conducted studies have shown the possibility of reducing welding stresses by up to 30 % under the effect of a pulsed electromagnetic field. The low efficiency of this treatment diagram is associated with the irrational arrangement of the inductors, in which the vectors of electromagnetic pressure (which are initiated by the action of this field) on the weld metal on both sides of the plate act in the opposite direction to each other. This leads to mutual annihilation of the pressure on the weld metal, and stress relaxation occurs exclusively due to electroplastic deformation under the condition of $j \geq 1$ kA/mm^2, which was met in [27]. A more rational diagram with a single plane inductor and a shield of nonferromagnetic material (disc of AMg6 alloy) located on the same axis on both sides of the specimen with a butt weld, respectively, is described in [28]. The shielding of the weld metal during the pulsed electromagnetic field treatment provides (due to the growth of the skin layer in the specimen metal at a certain pulsed current frequen-

cy) an increase in the volume of the current-carrying medium. Since the pressure force directly depends on the volume of the medium, its increase (with the use of a shield) contributes to a threefold increase in force (compared to pulsed electromagnetic field treatment without a shield) at constant values of the treatment mode parameters. This ensures a reduction in residual tensile welding stresses by up to 90 % with an eightfold reduction in displacements of the specimen surface points after treatment.

The effect of a pulsed electromagnetic field on the level of residual stresses in welded and deposited specimens of low-carbon steels, based on the intensification of the dynamic effect of magnetostriction [29], provided the reduction in stresses by up to 40 %.

The results of studies of the effect of this field on the change in residual welding stresses are shown in [30]: residual tensile stresses in specimens of welded joints made of St2(semi-killed) steel are reduced by 3–25 %, and there is a more uniform distribution of α-phase over the volume of the treated metal.

Comparison of the efficiency of pulsed electromagnetic field treatment on residual stresses in welded joints made of ferromagnetic and nonferromagnetic materials showed that its effect on the former is less influential. The obtained results can be explained by the fact that under the conditions of pulsed electromagnetic field treatment of ferromagnetic materials, the electromagnetic pressure force is consumed not only for stress relaxation, but also for magnetoelastic interaction of interdomain boundaries (Bloch walls) with dislocations [13, 31]. During this treatment of welded joints made of nonferromagnetic materials, the domain structure is absent, and the electromagnetic pressure force is used exclusively for stress relaxation.

The combined use of electropulsed and mechanical effects for the treatment of welded structures in order to extend their service life serves as the basis for the development of such a method of treatment of welded joints as the electrodynamic method [32]. It is based on the initiation of electrodynamic forces arising from the passage of a pulsed electric current in the material, provided that $j \geq 1$ kA/mm^2. During electrodynamic treatment, welded joint is subjected to a volumetric electrodynamic effect, which is characterized by the joint occurrence of electrical pulse and dynamic processes, their synergy in the treatment zone initiating the relaxation of welding stresses (according to the mechanism of electroplastic deformation) and dispersion of the metal structure.

The method of electrodynamic treatment has been widely used in engineering practice to eliminate local welding deformations such as "bulging" [33]. The effect of the diagrams for treating the outer surface of the bulging, such as "spot", "concentric circles", and "spiral", was investigated. It was proved that the least effective is the "spot" diagram, and the most effective is the "concentric circles" or "spiral" diagram, which allows to completely eliminate this defect. A comparative analysis has shown that the energy costs for removing the bulgings by this method are significantly lower than for thermal straightening.

The development of the abovementioned method for correcting local deformations of the "bulging" type when using the "concentric circles" diagram is also considered in [34]. The equipment for its implementation has an electromechanical electrode device and a power source with a pulsed electric current. The device for electrodynamic treatment is made in the form of at least one pair of identical mechanisms, each of which contains an electromechanical electrode-indenter (Figure 2). The devices are rigidly connected to each other through a clamping mechanism for fixing the indenters, each of which is equipped with an ultrasonic vibrator connected to a common power source.

The improved method of electrodynamic treatment can be used, for example, for technological support of the ongoing production of cladding plates for welded ship hull structures. During the straightening process, the treatment is performed simultaneously on at least one pair of bulging surface areas, and in conjunction with ultrasonic radiation concentrated in both treatment zones. The diagram of elements is shown in Figure 2, which shows the design of the electromechanical part of the device with an orientation towards the elimination of local deformations of the "bulging" type of thin-walled elements of welded structures. The combination of electrodynamic and mechanical (ultrasonic) effects allows achieving maximum efficiency of the process of electrodynamic treatment of welded joints.

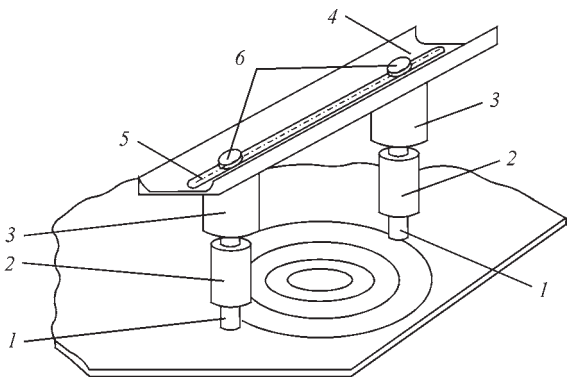

Figure 2. Design of a device for eliminating local deformations of the "bulging" type in plane elements of welded structures (discharge circuit branches are not indicated): *1* — movable electrode-indenter for electrodynamic treatment; *2* — ultrasonic exciter of mechanical oscillations (magnetostrictive or piezoelectric type); *3* — electromagnetic drive; *4* — traverse for mutual positioning of electrodes; *5* — linear groove; *6* — screw clamp [34]

Taking into account the results [14], which show that accompanying heating stimulates stress relaxation during electropulsed treatment of thin steel rods, research works on the efficiency of electrodynamic treatment of a cooling weld, performed during the thermodeformational welding cycle, are promising.

On the basis of [12–16], a hybrid technology "automatic welding + electrodynamic treatment" was developed, which allows lowering the energy intensity of the treatment process, reducing the working time for manufacturing a metal structure and simultaneously improving its quality [35]. The method of modernizing the process of electrodynamic treatment of welded joint metal differs in the fact that the weld on the root side is equipped with a sliding movable contact of the return terminal of the discharge circuit from the pulsed electric current power source. In the process of producing a welded joint, the movement of the movable contact is coaxial with the location of the contact zone of the electrode-indenter. The device for implementing the modernized method has an electrodynamic treatment unit with an electromechanical electrode-indenter and a pulsed electric current power source (Figure 3). The discharge circuit for the implementation of this treatment, in conjunction with the welding process by torch *8*, sequentially includes a movable indenter *2* and a part *14*, welded by weld *1* with a remote location of the reverse contact terminal *9*. The electromagnetic part of the indenter *4* and its movable impact mechanism are connected to the autonomous pulsed current power sources *5* and *6*, respectively, which is switched on at the electrode synchronously with the signals from the movable impact mechanism. The device contains a table *15* with a material sample in the weld location area *1* and a support traverse with a spring-loaded contact of a longitudinal slider *11* fixed below the table surface along the weld line, having an electrical connection to the return terminal of the pulsed power source of the corresponding electric current of the indenter impact mechanism (terminals I–II). This mechanism and the elastic contact of the slider have rigid mechanical connections with mechanisms for synchronizing the relative position of their axes. This modernization of the electrodynamic treatment method provides complete elimination of the effect of spark erosion of the treated material surface, as well as the possibility of a significant increase in the treatment efficiency based on the coordination of the phase characteristics of pulsed effects in the conditions of using a differentiator (synchronization device) in the pulsed electric current power source, i.e. in the pulsed power source (terminals III–IV).

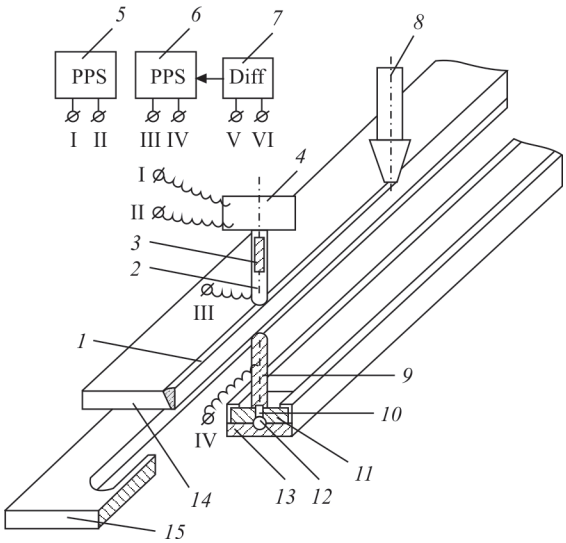

Figure 3. Diagram of the electrodynamic treatment method [35]: *1* — weld; *2* — movable part of the indenter; *3* — displacement sensor; *4* — electromagnetic part of the indenter; *5* — pulsed power source PPS (terminals I and II) of the electromagnetic part of the indenter; *6* — pulsed power source PPS (terminals III and IV) of the impact part of the indenter; *7* — differentiator Diff (terminals V and VI); *8* — welding torch; *9* — slider contact; *10* — rest spring; *11* — slider; *12* — roller slider rest; *13* — resting traverse; *14* — part to be welded; *15* — work table

A necessary condition for the implementation of this method is the synchronization of the pulsed electric current period with the time interval of dynamic pressure pulses based on a rational configuration of the discharge circuit, where the current pulse of the movable part of the electrode-indenter is controlled and transferred only when the signal is ready to propagate in the weld metal. The signals are synchronized by the element base using a differentiator *7*. The preceding action of the dynamic pressure pulse provides the necessary contact pressure for the passage of the pulsed electric current and eliminates the manifestation of spark-arc effects. Thus, the implementation of the electrodynamic treatment method is ensured by the design and composition of the equipment of the corresponding device. The mechanical equipment corresponds to one of the possible variants of the power layout of the equipment for this treatment with support for the function of stabilizing the relative positioning of the contact elements of the discharge circuit.

The method of "electrodynamic treatment + TIG welding" is implemented in an automated welding complex (Figure 4, *a*), whose design principles are based on the results of [35]. Testing of the method confirmed its efficiency in eliminating residual tensile stresses in butt joints of AMg6 alloy. The initial values of σ_x (along the weld) of membrane stresses (without electrodynamic treatment) reached up to 100 MPa in the centre of the weld. It was proved that while the above treatment after welding (at T = 20 °C) ensured the formation of membrane compressive stresses σ_x (along the weld) up to –50 MPa in the centre

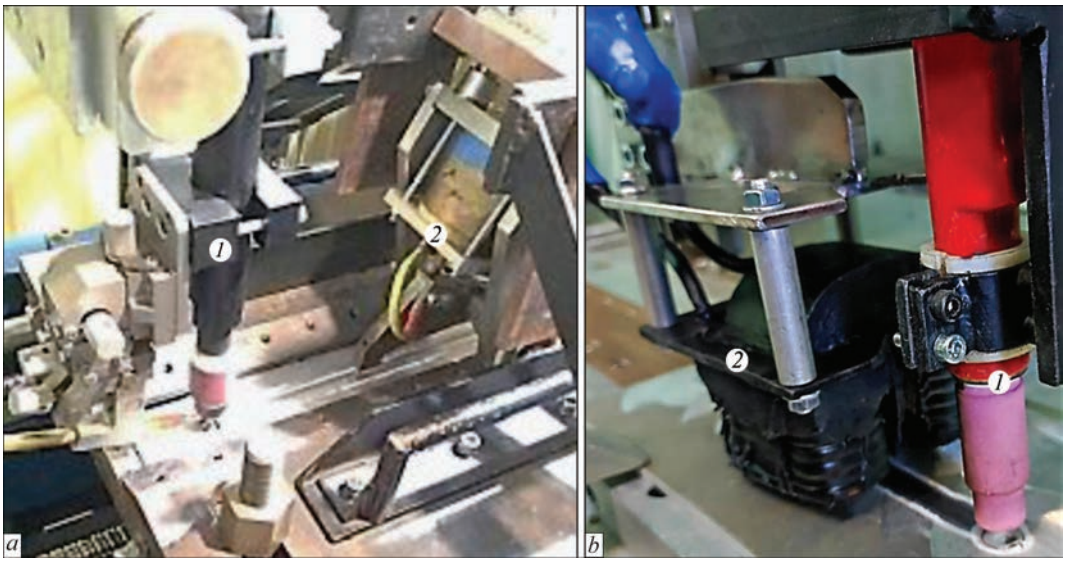

Figure 4. Appearance of equipment for hybrid welding technologies: *a* — "TIG welding + electrodynamic treatment" [36]: *1* — TIG torch; *2* — electrode system for this treatment [36]; *b* — "TIG welding + pulsed electromagnetic field treatment" [41]: *1* — TIG torch; *2* — inductor for this treatment [41]

of the weld, after it during welding (at T = 150 °C) σ_x = –100 MPa [36].

Among the recent methods of external effect on the quality of metal products is the study of the effect of pulsed electromagnetic fields and constant magnetic fields) applied to the melt during its solidification to produce cast billets and parts from nonferromagnetic materials, such as aluminium alloys. It has been determined that the effect of constant magnetic fields contributes to the evolution of their structure and increases resistance to corrosion damage. The mechanism of structure formation is based on the manifestations of the action of these fields — structural components decrease, a morphology of intermetallic phases changes, their microhardness increases, their sizes and configuration change, which are similar to the solidification processes at high cooling rates [37].

The liquid metal, which is the content of the weld pool, in fusion welding, under certain assumptions, is similar in properties (with a much smaller volume) to the metal during casting, i.e., suitable for treatment with a pulsed electromagnetic field and a constant magnetic field. Taking into account the results of [37], it should be noted that the abovementioned treatment of the cooling metal at the rear front of the weld pool is appropriate to improve the residual stress-strain state and structure of the welded joint metal. This led to the creation of a suitable method for treating welded joints during a thermodeformational welding cycle and a hybrid technology "automatic welding + constant magnetic field treatment" [38]. This method is advisable for welded joints made of nonferromagnetic metal alloys based on Al, Mg, Ti, which do not have domain structures. This results in a higher electromagnetic pressure force (compared to carbon steels) generated by a constant magnetic field.

As a tool to control the structure of the weld metal and the stress state of the welded joint, it is promising for energy reasons to use a pulsed electromagnetic field instead of a constant field with a set frequency to influence the rear front of the weld pool. The use of a pulsed field can significantly increase the energy and, as a result, the force of electromagnetic pressure on the weld metal compared to the use of a constant field. ECP generators based on components of modern power electronics provide a pulsed electromagnetic field frequency of ≤ 1/s [39, 40]. The frequency of its actions at standard TIG welding speeds V_w = 4 mm/s is comparable in efficiency to the effect of a constant magnetic field. A mathematical model of electrophysical processes under the action of a pulsed field on nonferromagnetic materials based on Al was developed and its positive effect on the structure and residual stresses of welded joints made of AMg6 alloy was proved [41, 46]. Based on the results of [39–41, 46], an automated welding complex was created (Figure 4,*b*), which implements the hybrid technology "pulsed electromagnetic field treatment + TIG welding".

A promising direction for the treatment of metal alloys and welded joints is the use of electro-pulse AOTs technologies, originally developed for the technical purification of aqueous solutions [42]. The generation of electric current pulses in AOTs occurs near the surface of the medium being treated and uses a pulsed barrier discharge that acts on the surface through a dielectric barrier.

The generation of electric current pulses on the surface of metal alloys has led to the creation of a new technological process — metal pulsed barrier discharge treatment (Figure 5) [43]. It generates low-temperature plasma on the surface of the metal being treated, and its application is a new approach to optimizing the mechanical properties of high-strength steels for welded

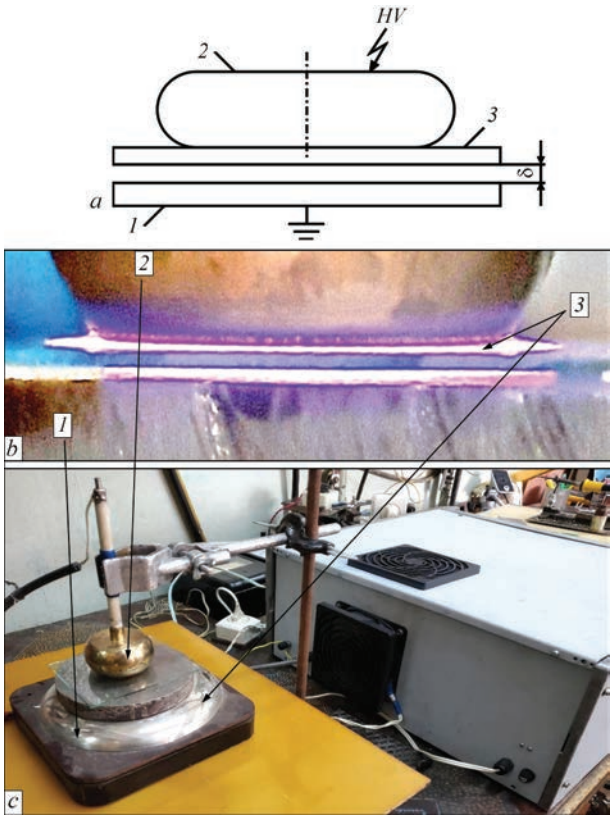

Figure 5. Treatment of metal alloys by pulsed barrier discharge (PBD) [44]: *a* — treatment diagram; *HV* — high voltage from the pulsed current generator; *1* — metal being treated; *2* — electrode; *3* — dielectric barrier (quartz glass); δ — air gap; *b* — structural steel treatment process; *1–3* correspond to Figure 5, *a*; *c* — hardware complex for treatment of metals and welded joints

structures, based on electrophysical processes. In [44], the strengthening of 25KhGNMT steel as a result of the action of such a discharge on its surface was investigated. Based on the transmission electron microscopy method, it was found that the HV hardness values after pulsed barrier discharge treatment increase from 420 to 505 kg/mm^2 and are accompanied by a general increase in dislocation density and microstructure dispersion. This has a positive effect on the mechanical properties of 25KhGNMT steel for welded structures operating under dynamic loads. The obtained results open up new possibilities for the application of pulsed barrier discharge treatment for the evolution of the structure of metal alloys and welded joints.

Figure 6 shows a structural diagram of electrophysical technologies based on processes using a pulsed electromagnetic field. One specific area of research is the study of the effect of pulsed barrier discharge treatment on the service life of metal alloys and welded joints, including light and non-ferrous alloys and structural steels, with the aim of evolving their structure to increase hardness and regulate stress states.

Studying the possibility of using pulsed barrier discharge treatment for local non-destructive evaluation of residual stress states in metals, alloys and welded joints is promising. Treatment of local areas (with a diameter of ≤ 1.0 mm) can be an alternative to drilling local holes on the metal surface, which is a necessary condition for the use of the electronic speckle interferometry method to determine stresses [45]. The disadvantage of this procedure is that it is conditionally destructive. This limits its use on full-scale critical metal structures that are intended for operation and on which even minimal surface point damages are excluded.

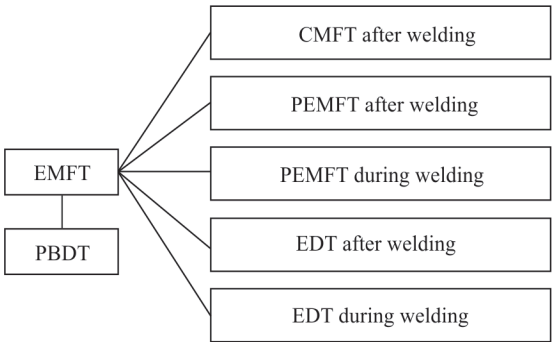

Figure 6. Structure of promising research on the effect of magnetic field treatment (EMFT) on the life of metal alloys and welded joints: CMFT — constant magnetic field treatment with a; PEMFT — pulsed electromagnetic field treatment; EDT — electrodynamic treatment; PBDT — pulsed barrier discharge treatment

Thus, the use of the speckle interferometry method is only possible on witness specimens or simulation structures. In the proposed procedure, pulsed barrier discharge treatment of a local surface area can be used for stress relaxation (instead of drilling a hole). Determining correlation dependence between the speckle-patterns of the surface around the treated area and around the drilled hole will allow using electronic speckle-interferometry as a non-destructive method for evaluating stress states on the surface of metal welded structures.

The experience in studying the impact of electromagnetic fields on metals and alloys proves the possibility of using electrophysical technologies to control stress states, improve the structure, tribological and mechanical characteristics of welded joints in structures of mechanical engineering, shipbuilding and aerospace industry.

CONCLUSIONS

1. Promising technologies for improving the mechanical properties and stress state of metal alloys and welded joints based on the use of electromagnetic fields and their derivatives, such as electrodynamic pressure force, eddy currents, and shock waves were analyzed.

2. The positive effect of microadditives of the Ti–TiC system modifier, obtained by electrohydropulsed treatment with high-energy discharge, on the operational properties of the deposited metal of the 25Kh5FMS tool steel type were proven.

3. It was shown that various methods of treatment with a pulsed electromagnetic field contribute to the reduction of residual stresses in welded joints. The advan-

tages of such treatment of weld metal during welding compared to treatment at room temperature were proven.

4. The mechanism of surface strengthening of 25KhGNMT steel as a result of its pulsed barrier discharge treatment was investigated. It was proven that it contributes to an increase in dislocation density and microstructure dispersion, i.e. it has a positive effect on the mechanical properties of steel. The prospects for using pulsed barrier discharge for non-destructive testing of residual stresses in welded joints was considered.

REFERENCES

1. Razmyshlyaev, A.D., Ageeva, M.V. (2018) On mechanism of weld metal structure refinement in arc welding under action of magnetic fields (Review). *The Paton Welding J.*, **3**, 25–28. DOI: https://doi.org/10.15407/tpwj2018.03.05
2. Dubodelov, V.I., Goryuk, M.S. (2018) The use of electromagnetic fields and magnetohydrodynamic phenomena to intensify the influence on metal systems: World and Ukrainian experience. In: *Science of materials: Achievements and prospects.* Vol. 2. Ed. by L.M. Lobanov et al. Kyiv, Akademperiodyka, 24–50 [in Ukrainian].
3. Opara, V.S., Reznikova, L.Y., Yurchenko, E.S., Petushkov, V.G. (1984) Influence of welded joint stiffness on reduction of residual stresses during electrohydroimpulse processing. *Avtomaticheskaya Svarka*, **7**, 70–71 [in Russian].
4. Sizonenko, O., Vovchenko, A. (2014) Pulsed discharge technologies of processing and obtainment of new materials (Review). *Machines. Technologies. Materials*, 8(**12)**, 41–44. https://stumejournals.com/journals/mtm/2014/12/41
5. Lipyan, E.V., Sizonenko, O.N., Torpakov, A.S., Zhdanov, A.A. (2015) Thermodynamic analysis of heterogeneous chemical reactions in the system "mixture of Fe–Ti powders–hydrocarbon liquid" under the influence of high-voltage electric discharges. *Visnyk NTU "KhPI". Seriia: Tekhnika ta Elektrofizyka Vysokykh Napruh: Zb. Nauk. Prats*, 51(**1160**), 59–65 [in Russian].
6. Syzonenko, O.M., Prokhorenko, S.V., Lypyan, E.V. et al. (2020) Pulsed discharge preparation of a modifier of Ti–TiC system and its influence on the structure and properties of the metal. *Materials Sci.*, 56(**2**), 232–239. DOI: https://doi.org/10.1007/s11003-020-00421-1
7. Lobanov, L.M., Syzonenko, O.M., Holovko, V.V. et al. (2021) Pulsed-disharge treatment of the Al–Ti–C system modifier. *The Paton Welding J.*, **5**, 24–29. DOI: https://doi.org/10.37434/tpwj2021.05.04
8. Lobanov, L.M., Ryabtsev, I.O., Pashchyn, M.O. et al. (2023) Wear resistance of titanium carbide-modified 25Kh5FMS deposited metal. *Strength of Materials*, 55(**3**), 469–474. DOI: https://doi.org/10.1007/s11223-023-00539-y
9. Ryabtsev, I.O., Babinets, A.A., Pashchin, M.O. et al. (2023) Influence of different types of modifiers on the structure and properties of deposited metal of the type of 25Kh5MFS tool steel. *The Paton Welding J.*, **5**, 11–14. DOI: https://doi.org/10.37434/tpwj2023.05.02
10. Sprecher, A.F., Mannan, S.L., Conrad, H. (1986) Overview no. 49: On the mechanisms for the electroplastic effect in metals. *Acta Metallurgica*, 34(**7**), 1145–1162. DOI: https://doi.org/10.1016/0001-6160(86)90001-5
11. Baranov, Yu.V., Troitsky, O.A., Avramov, Y.S. (2001) *Physical bases of electric pulse and electroplastic processing and new materials*. Moscow, MGIU [in Russian].
12. Stepanov, G.V., Babutskii, A.I., Mameev, I.A. (2004) High-density pulse current-induced unsteady stress-strain state in a long rod. *Strength of Materials*, 36(**4**), 377–381. DOI: https://doi.org/10.1023/B:STOM.0000041538.10830.34
13. Strizhalo, V.A., Novogrudsky, L.S., Vorobyev, E.V. (2008) Strength of materials at cryogenic temperatures taking into account the influence of electromagnetic fields. Vol. 1. *Strength of materials and structures: A series of monographs*. Ed. by V.T. Troshchenko. Kyiv, IPS of the NASU [in Russian].
14. Troitsky, O.A., Kalymbetov, P.U. (1981) Dependence of the electroplastic effect in zinc on the duration of individual pulses. *Fizika Metallov i Metallovedenie*, 51(**5**), 1056–1059 [in Russian].
15. Stepanov, G.V., Babutskii, A.I., Mameev, I.A., Olisov, A.N. (2006) Analysis of pulse current-induced tensile stress relaxation. *Strength of Materials*, 38(**1**), 84–91. DOI: https://doi.org/10.1007/s11223-006-0019-4
16. Strizhalo, V.A., Novogrudskij, L.S. (1997) Determination of the electroplastic strain energy of metals. *Problemy Prochnosti*, **4**, 38–43. https://www.scopus.com/record/display.uri?eid=2-s2.0-0031108852&origin=recordpage
17. Morris, J.W., Fultz, B., Chan, J.W., Mei, Z. (1989) The influence of high magnetic fields on mechanical properties of metastabile austenitic steels. *Fizika Nizkikh Temperatur*, 15(**10**), 1072–1080. DOI: https://doi.org/10.1063/10.0032269
18. Guoyi Tang, Zhuohui Xu, Miao Tang et al. (2005) Effect of a pulsed magnetic treatment on the dislocation substructure of a commercial high strength steel. *Materials Sci. and Eng.: A*, 398(**1–2**), 108–112. DOI: https://doi.org/10.1016/j.msea.2005.03.003
19. Liping Ma, Wenxiang Zhao, Zhiqiang Liang et al. (2014) An investigation on the mechanical property changing mechanism of high speed steel by pulsed magnetic treatment. *Materials Sci. and Eng.*: A, **609**, 16–25. DOI: https://doi.org/10.1016/j.msea.2014.04.100
20. Batainen, O., Klamecki, B., Koepke, B. (2003) Effect of pulsed magnetic treatment on drill wear. *J. of Materials Proc. Techn.*, 134(**2**), 190–196. DOI: https://doi.org/10.1016/S0924-0136(02)01002-6
21. Babutsky, A., Chrysanthou, A., Ioannou, J. (2009) Influence of pulsed electric treatment on corrosion of structural metals. *Strength of Materials*, **4,** 387–391. DOI: https://doi.org/10.1007/s11223-009-9142-3
22. Babutsky, A., Chrysanthou, A., Ioannou, J., Mamuzic, I. (2010) Correlation between the corrosion resistanse and the hardness scattering of structural metals treated with a pulse electric current. *Mater. Technol*., 44(**2)**, 99–102. http://mit.imt.si/izvodi/mit102/babutsky.pdf
23. Bigyan Fang, Jinqiu Wang, Suhong Xiao (2005) Stress corrosion cracking of X-70 pipeline steels by electropulsing treatment in near-neutral pH solution. *J. Mater. Sci. Technol.*, 40(**24)**, 6545–6552. DOI: https://doi.org/10.1007/s10853-005-1813-2
24. Golovin, Yu.I., Morgunov, R.B., Zhulikov, S.E. et al. (1998) Influence of magnetic field on metastable structural defects relaxation and plasticity of crystals. *Vestnik TGU*, 3(**3**), 271–274 [in Russian].
25. Klimov, K.M., Burkhanov, Y.S., Novikov, I.I. (1985) Effect of high conductivity electric current on the process of plastic deformation of aluminum. *Problemy Prochnosti*, **6**, 44–47 [in Russian].
26. Semashko, N.A., Krupsky, R.F., Kupov, A.V. (2004) Acoustic emission during electric pulse deformation of titanium alloys. *Materialovedenie*, **7**, 29–33 [in Russian].
27. Stepanov, G.V., Babutskii, A.I., Mameev, I.A. et al. (2011) Redistribution of residual welding stresses in pulsed electromagnetic treatment. *Strength of Materials*, 43(**3**), 326–331. DOI: https://doi.org/10.1007/s11223-011-9300-2
28. Lobanov, L.M., Pashchyn, M.O, Mikhodui, O.L. et al. (2021) Pulsed electromagnetic field effect on residual stresses and strains of welded joints of AMg6 aluminum alloy. *Strength of Materials*, 53(**6**), 834–841. DOI: https://doi.org/10.1007/s11223-022-00350-1
29. Yanli Song, Lin Hua (2012) Mechanism of residual stress reduction in low alloy steel by a low frequency alternating magnetic treatment. *J. Mater. Sci. Technol*., 28(**9**), 803–808. DOI: https://doi.org/10.1016/s1005-0302(12)60134-0

30. Tsaryuk, A.K., Skulsky, V.Yu., Moravetsky, S.I., Sokirko, V.A. (2008) Influence of electromagnetic treatment on residual welding stresses in welded joints of carbon and low-alloyed steel. *The Paton Welding J.,* **9**, 22–25.
31. Shao Quan, Kang Jiajie, Xing Zhiguo et al. (2019) Effect of pulsed magnetic field treatment on the residual stress of 20Cr2Ni4A steel. *J. of Magnetism and Magnetic Materials*, **476**, 218–224. DOI: https://doi.org/10.1016/j.jmmm.2018.12.105
32. Lobanov, L., Kondratenko, I., Zhiltsov, A. et al. (2018) Development of post-weld electrodynamic treatment using electric current pulses for control of stress-strain states and improvement of life of welded structures. *Materials Performance and Characterization*, 7(**4**), 941–955. DOI: https://doi.org/10.1520/MPC20170092
33. Han Shanguo, Lobanov, L.M., Cai Detao et al. (2016) *Portable welding deformation control equipment and deformation treatment method thereof*. European Pat. Office. Priority Number(s): CN201510142968 20150330. Bibliographic Data: CN104722978 (B) — 2016-04-27 https://worldwide.espacenet.com/publicationDetails/biblio?CC=CN&NR=104722978B&KC=B&FT=D&ND=5&date=20160427&DB=&locale=en_EP
34. Lobanov, L.M., Kondratenko, I.P., Pashchyn, M.O., Volkov, S.S. (2021) *Method for eliminating residual stresses and deformations in welded joints and device for its implementation*. Pat. for Invention 122829, 06.01.2021 [in Ukrainian].
35. Lobanov, L.M., Kondratenko, I.P., Pashchyn, M.O., Volkov, S.S. (2021) *Method for eliminating residual stresses and deformations in welded joints and device for its implementation*. Pat. for Invention 122933, 20.01.2021 [in Ukrainian].
36. Lobanov, L.M., Korzhik, V.M., Pashchin, M.O. et al. (2022) Deformation-free TIG welding of AMg6 alloy with application of electrodynamic treatment of weld metal. *The Paton Welding J.,* **8,** 3–8. DOI: https://doi.org/10.37434/tpwj2022.08.01
37. Dubodelov, V.I., Seredenko, Ye.V., Zatulovskyi, A.S., Seredenko V.A. (2018) Increase of properties of aluminum alloys by the action of a permanent magnetic field on melting at solid state. *The Scientific Technical J. Metal Sci. and Treatment of Metals*, 24(**4**), 3–8. DOI: https://doi.org/10.15407/mom2018.04.003
38. Bobrinsky, V.I., Rodin, N.P., Fomicheva, L.F. et al. (2006) *Fusion welding method*. Pat. 2288823 RF, Publ. 20.12.2006 [in Russian].
39. Akinin, K.P., Antonov, O.E., Petukhov, I.S. et al. (2010) Construction of electromechanical energy converters of increased efficiency. *Instytut Elektrodynamiky NANU: Zb. Nauk. Prats*, **26**, 3–12 [in Ukrainian].
40. Antonov, O.E., Mikhalskyi, V.M., Petukhov, I.S. et al. (2012) Investigation of processes in electromechanical and semiconductor energy converters. *Instytut Elektrodynamiky NANU: Zb. Nauk. Prats,* **32**, 5–19 [in Ukrainian].
41. Lobanov, L.M., Pashchyn, M.O., Mikhodui, O.L. et al. (2025) Scientific principles of magnetic pulse treatment of welded joints in the process of fusion welding. In: *Welding and Related Technologies*. Eds by I.V. Krivtsun et al., 183–187. DOI: https://doi.org/10.1201/9781003518518
42. Bo Jiang, Jingtang Zheng, Shi Qiu et al. (2014) Review on electrical discharge plasma technology for waste water. *Chemical Engineering J.*, **236**, 348–363. DOI: https://doi.org/10.1016/j.cej.2013.09.090
43. Bozhko, I.V., Zozuljov, V.I., Kobylchak, V.V. (2016) SOS-generator for the electric discharge technology used pulse barrier discharge. *Tekhnichna Elektrodynamika*, **2**, 63–68 [in Ukrainian]. DOI: https://doi.org/10.15407/techned2016.02.063
44. Bozhko, I.V., Kondratenko, I.P., Lobanov, L.M. et al. (2023) Pulsed barrier discharge for treatment of surfaces of 25KhGNMT steel plates. *Tekhnichna Elektrodynamika*, **1**, 76–80 [in Ukrainian]. DOI: https://doi.org/10.15407/techned2023.01.076
45. Lobanov, L.M., Knysh, V.V., Pashchin, M.O. et al. (2023) Nondestructive evaluation of residual stresses in welded joints on the base of a combination of ultrasonic testing and speckle-interferometry. *Tekhnichna Diahnostyka ta Neruinivnyi Kontrol*, **2**, 22–27 [in Ukrainian]. DOI: https://doi.org/10.37434/tdnk2023.02.03
46. Lobanov, L.M., Pashchyn, M.O., Mikhodui, O.L. et al. (2022) Stress-strain state of welded joints of AMg6 alloy after electrodynamic treatment during welding. *Strength of Materials*, 54(**6**), 983–996. DOI: https://doi.org/10.1007/s11223-023-00474-y

ORCID
L.M. Lobanov: 0000-0001-9296-2335,
L.I. Nyrkova: 0000-0003-3917-9063,
M.O. Pashchyn: 0000-0002-2201-5137,
O.L. Mikhodui: 0000-0001-6660-7540,
N.L. Todorovych: 0000-0002-3872-5790,
O.M. Syzonenko: 0000-0002-8449-2481,
I.P. Kondratenko: 0000-0003-1914-1383,
V.V. Chopyk: 0000-0002-5046-5223,
O.M. Karlov: 0000-0002-1350-1870

CONFLICT OF INTEREST
The Authors declare no conflict of interest

CORRESPONDING AUTHOR
M.O. Pashchyn
E.O. Paton Electric Welding Institute of the NASU
11 Kazymyr Malevych Str., 03150, Kyiv, Ukraine.
E-mail: svarka2000@ukr.net

SUGGESTED CITATION
L.M. Lobanov, L.I. Nyrkova, M.O. Pashchyn,
O.L. Mikhodui, O.M. Tymoshenko,
N.L. Todorovych, O.M. Syzonenko,
I.P. Kondratenko, V.V. Chopyk, O.M. Karlov (2025)
Research into technological processes of treatment of metals, alloys and welded joints using electromagnetic field (Review).
The Paton Welding J., **11**, 10–18.
DOI: https://doi.org/10.37434/tpwj2025.11.02

JOURNAL HOME PAGE
https://patonpublishinghouse.com/eng/journals/tpwj

Received: 09.06.2025
Received in revised form: 07.08.2025
Accepted: 03.11.2025

DOI: https://doi.org/10.37434/tpwj2025.11.03

RESIDUAL STRESSES IN THE JOINT OF THE COLLECTOR TO THE DN1200 NOZZLE OF THE PGV-1000 STEAM GENERATOR DUE TO LOCAL HEAT TREATMENT

O.V. Makhnenko, O.F. Muzhychenko, I.I. Prudkiy, N.R. Basistyuk

E.O. Paton Electric Welding Institute of the NASU
11 Kazymyr Malevych Str., 03150, Kyiv, Ukraine

ABSTRACT

When assessing the extension of the service life of WWER-1000 NPP power units, the welded joint of the collector to the DN1200 nozzle of the PGV-1000 steam generator is an object of increased attention due to its tendency to the formation of discontinuity defects. In order to obtain more detailed information regarding the loading of this welded joint, mathematical modeling of the kinetics of formation of residual stresses and plastic strains, as a result of local postweld heat treatment in the high-temperature tempering mode, was carried out using the finite element method. The complex geometry of the joint and the local arrangement of the heaters cause significant nonuniformity of heating during heat treatment, which can lead to negative consequences, namely, formation of high residual tensile stresses in the dangerous zones of the welded joint. It is proven that the axisymmetric 2D finite element model of the joint with the shortest length of the DN1200 nozzle provides sufficient conservatism of the results compared to the general 3D model.

KEYWORDS: PGV-1000 steam generator, welded joint No. 111, local heat treatment, residual stresses, plastic strains, mathematical modeling, creep

INTRODUCTION

Over the past twenty years, during the operation of WWER-1000 power units at the Ukrainian NPP, material discontinuity defects have been repeatedly detected in the welded joint between the collector and the DN1200 nozzle of the PGV-1000 steam generators welded joint No.111, which is part of the first and second reactor cooling circuits [1, 2]. To substantiate the possibility of operating steam generators with such defects in the area of welded joint No. 111, at least until the next scheduled preventive maintenance, modern approaches to the mechanics of fracture of structural materials with crack-like defects can be applied to predict their behaviour under different loading conditions [2–6]. To perform such calculations, it is very important to have information on the load of the collector to the DN-1200 nozzle welded joint [7–10], including residual stresses associated with the manufacturing or repair technology [11–13].

Experimental determination of residual stresses in thick-walled structures of existing equipment is possible either on the outer surfaces using a standardized method of tensometry [14] or laser speckle interferometry (ESPI–HD method) [15] when drilling a hole, or requires more in-depth studies of a model specimen in the laboratory, for example, by neutron diffraction [16]. It is also advisable to perform finite element modeling of the distribution of residual stresses in the volume of the welded joint [13, 17], which should be consistent with the results of experimental measurements.

Given the urgency of the problem of damage to welded joint No. 111 for the Ukrainian NPP, it is necessary to determine the reliable distribution of residual technological stresses in the specified joint for the purpose of further calculated justification of its operability with the discontinuity defects identified during operation.

DESIGN, MATERIALS AND MANUFACTURING TECHNOLOGY OF WELDED JOINT No. 111

Figure 1 shows a layout of the collector welded joint to the DN1200 nozzle of the PGV-1000 steam generators. The DN1200 nozzle of the steam generator and collector are made of 10GN2MFA pearlite steel. The welded joint is made by manual or automatic welding. The root of the weld is made manually by argon arc welding using filler wire Sv08G2S. The height of the root pass is 6–8 mm. The main part of the weld is filled by manual welding using TsU-7 or UONI-13/55 electrodes with a diameter of 4 or 5 mm, and in automatic welding Sv08GSMT and Sv10GN1MA wires with a diameter of 2 mm and FTs-16 or AN-17 flux are used.

To relieve residual stresses associated with either welding during manufacture or repair of individual defects in welded joint No. 111 (Figure 1) detected during operation, a local heat treatment procedure is

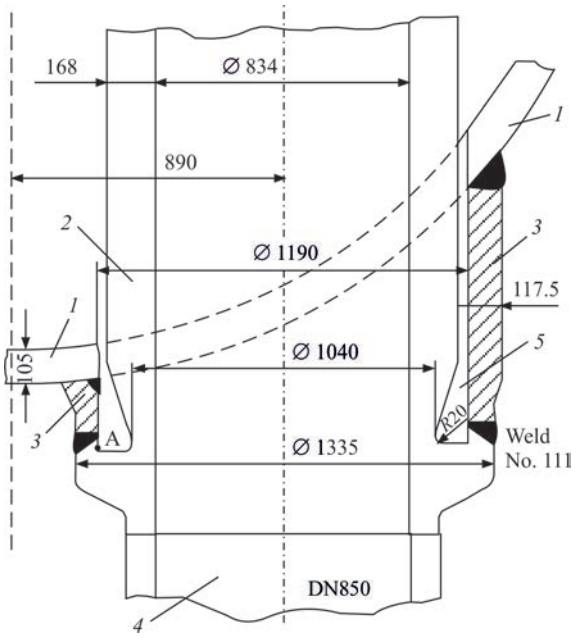

Figure 1. Layout of welded joint No. 111: *1* — steam generator case; *2* — collector; *3* — DN1200 nozzle; *4* — DN850 pipeline; *5* — pocket; *A* — discontinuity defect

performed using a high tempering mode (T_{max} = 650 °C) with ring heaters.

THE AIM

of this paper is to analyse the effect on the residual stress state of local heating of a rather complex geometry of the welded joint between the collector and the steam generator nozzle, which contains an inner pocket between the collector and the nozzle and is not axisymmetric, i.e., has different lengths of the nozzle along the circumferential coordinate. Local postweld heat treatment of such a joint may lead to the formation of new high residual stresses after partial relieving of the residual welding stresses. Therefore, in order to conduct an in-depth analysis of the problem, this paper considers the formation of residual stresses only after local heat treatment, without taking into account the stresses forming after multipass welding. By the method of mathematical modeling in a general three-dimensional formulation, taking into account

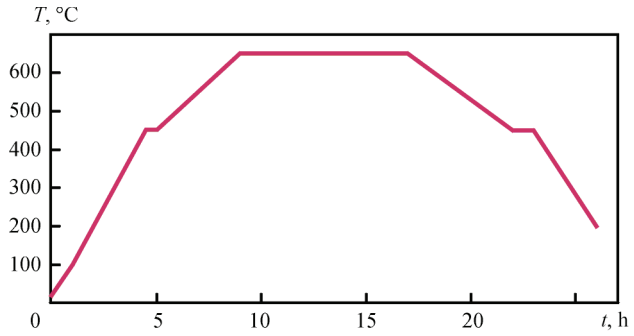

Figure 3. Diagram of varying heat treatment temperature in the high tempering mode

the non-axisymmetry of welded joint No. 111, as well as in a two-dimensional axisymmetric formulation, the distribution of residual stresses as a result of local heat treatment alone was calculated.

Two options of postweld local heat treatment are considered, namely, during the manufacturing process and during in-service repair. These options differ in the number of local heating zones. During the manufacture of the steam generator in the factory conditions, welded joint No. 111 has access to heating from the inside of the collector (Figure 2, *a*). During the repair of welded joint No. 111 at NPP, when the steam generator collector is connected to the DN850 pipeline of the first circuit, there is no possibility of heating from the inside of the collector (Figure 2, *b*), which can significantly affect the temperature distribution during postweld local heat treatment.

In the area where the heating elements are located (Figure 2), the surface temperature changes over time (from the start of the heat treatment operation) in accordance with the diagram in Figure 3. The rest of the heated surface of the joint is subject to convection heat exchange with the environment with appropriate heat transfer coefficients for the outer surface of the joint, which is specially covered with heat-insulating materials, as well as for the inner surface of the pocket, where convection heat exchange is limited.

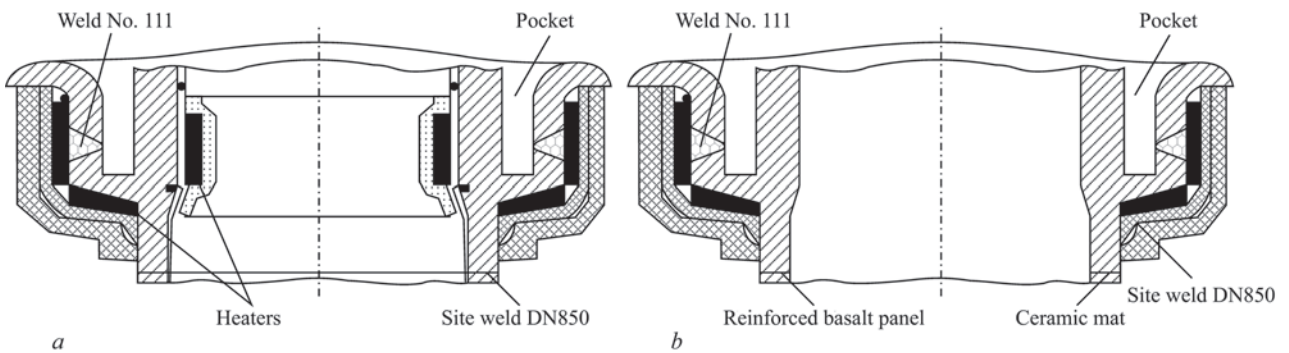

Figure 2. Layout of heaters and heat-insulating materials on welded joint No. 111 during local postweld heat treatment: *a* — during the manufacture of the steam generator in the factory conditions; *b* — during the repair of the welded joint at NPP

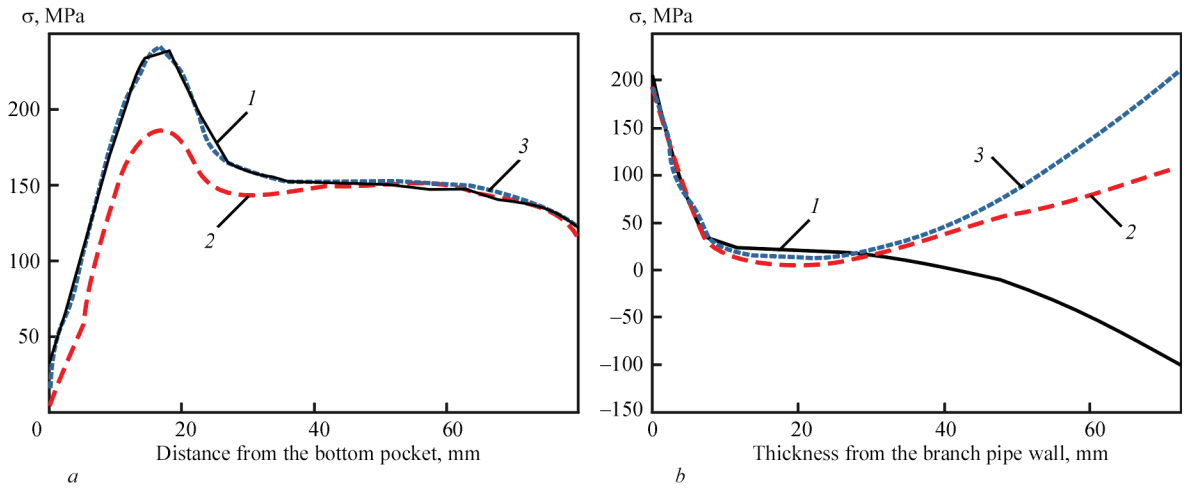

Figure 4. Distribution of axial σ_z (*1*), circumferential σ_β (*2*) and equivalent σ_1–σ_3 (*3*) residual stresses on the surface of the pocket on the side of the nozzle (*a*) and over the thickness of its wall (*b*), starting from the point with the maximum stress (based on the results of two-dimensional calculations [11])

EXISTING DATA ON THE DISTRIBUTION OF RESIDUAL STRESSES

The results of numerical modeling of residual stresses in welded joint No. 111 are shown in Figure 4 [11]. It is seen that at the specified heating areas and modes of factory heat treatment, as well as the physical and mechanical properties of the material (10GN2MFA steel), local heating of the joint causes local temperature expansion of the heated area and the development of plastic compression strains in the axial and tangential directions on the inner surface of the pocket on the side of the nozzle. In the areas of inelastic compression, residual tensile stresses occur during further cooling. The distribution of the axial stress component on the surface of the pocket on the nozzle side has a characteristic maximum in the area of the fillet transition at a distance of about 17 mm from the bottom of the pocket (Figure 4, *a*). In addition to the axial component, high circumferential residual tensile stresses are formed over the thickness of the nozzle closer to the inner surface (Figure 4, *b*). The increased stresses formed as a result of heat treatment, taking into account their concentration in the area of defects, may cause crack initiation.

DEVELOPMENT OF A MATHEMATICAL MODEL FOR DETERMINING RESIDUAL STRESSES AFTER LOCAL HEAT TREATMENT OF WELDED JOINT No. 111

To calculate the residual stresses, a general 3D finite element model of the welded joint of the collector to the DN1200 nozzle was developed, taking into account the variable length of the nozzle along the circumferential coordinate ($H \approx 240$–920 mm) (Figure 5), as well as a simplified axisymmetric 2D model (Figure 6) with the length of the nozzle equal to the minimum value in the actual structure.

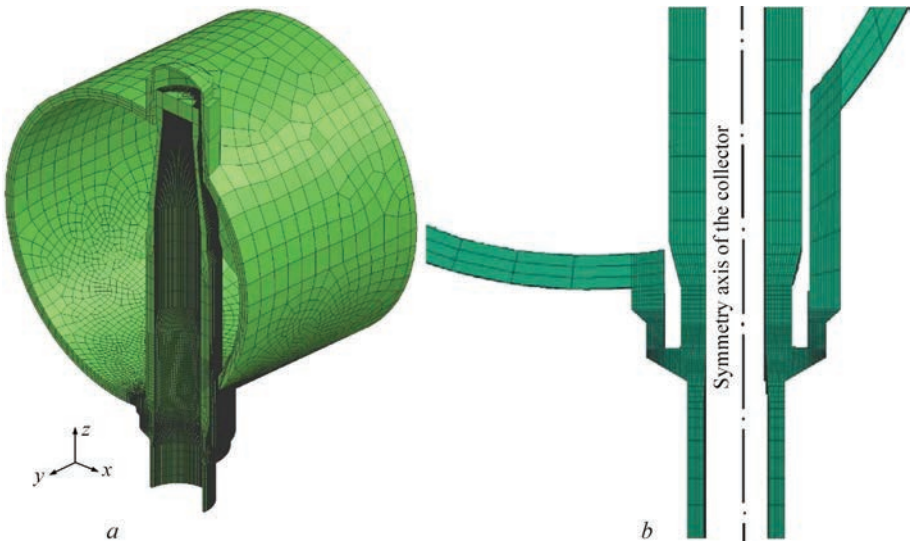

Figure 5. Finite element 3D model of welded joint No. 111 of the PGV-1000 steam generator: *a* — general appearance; *b* — cross section

Figure 6. Finite element axisymmetric 2D model of welded joint No. 111

The ring heating sources (heaters), which provide local heat treatment of the welded joint, were simulated by the corresponding heat flow through the heating surface according to the specified programme, as indicated for the high tempering mode (Figure 3). Schemes of 3D and 2D models of the welded joint and a finite element mesh are shown in Figures 5 and 6, respectively. The temperature dependences of the thermophysical and mechanical properties of 10GN2MFA steel are given in Table 1.

The kinetics of temperature distributions during local heat treatment was determined by solving the nonstationary heat conduction equation:

$$c\rho\frac{\partial T}{\partial t}=\frac{\partial}{\partial x}\left(\lambda\frac{\partial T}{\partial x}\right)+\frac{\partial}{\partial y}\left(\lambda\frac{\partial T}{\partial y}\right)+ +\frac{\partial}{\partial z}\left(\lambda\frac{\partial T}{\partial z}\right), \quad (1)$$

where T is the temperature, °C; c is the specific heat capacity, J/kg·°C; ρ is the density, kg/m^3; λ is the thermal conductivity, W/(m·°C).

The peculiarity of the model of the heating source for local heat treatment is the heat dissipation (heat flux) through the contact surfaces of the heaters. In the absence of data on the heat output of the heaters, the time-varying heat flux on the contact surface of the heaters into the material of the joint was set through the boundary conditions of contact heat exchange with the heater at a temperature $T_H(t)$, as specified for the high tempering mode (Figure 3):

$$q_H(t)=\lambda\frac{\partial T}{\partial n}=-h_H(T_H(t)-T), \quad (2)$$

where h_H is the heat transfer coefficient to the joint material from the heaters, the value of h_H = = 150 W/(m^2·°C) was chosen from the condition of ensuring the heating rate of the welded joint metal of 45–100 °C/h in accordance with the high tempering mode.

Boundary conditions on the surfaces of the models of the joint, taking into account convection heat exchange with the environment, were set in the form:

$$q=\lambda\frac{\partial T}{\partial n}=-h(T_0-T), \quad (3)$$

where q is the heat flux on the surface of the joint elements; T_0 is the ambient temperature; h is the heat transfer coefficient from the surface during convection heat exchange with the environment. Typically, T_0 = 20 °C, h = 15 W/(m^2·°C) from the surface under conditions of natural convection in the air; when installing heat-insulating materials, h = 2 W/(m^2·°C) can be accepted.

The model of thermoviscoplastic deformation of the welded joint material assumes that the total strain tensor is the sum of elastic, plastic and creep strains:

Table 1. Mechanical and thermophysical properties of 10GN2MFA steel depending on temperature [5]

Temperature T, °C	Young's modulus $E\cdot10^{-5}$, MPa	Yield strength $\sigma_y(T)$, MPa	Thermal conductivity λ, J/(cm^3·°C)	Volumetric heat capacity cγ, J/(cm^3·°C)	Poisson's ratio μ	Coefficient of linear expansion α, 1/°C
100	2.01	488	0.375	3.88	0.25	1.14
200	1.96	466	0.370	3.98	0.25	1.18
300	1.90	443	0.360	4.21	0.25	1.22
350	1.87	415	0.355	4.44	0.25	1.25
400	1.85	380	0.350	4.76	0.25	1.30
500	1.78	355	0.337	5.10	0.25	1.34
600	1.70	300	0.320	5.80	0.25	1.39
700	1.60	200	0.305	7.35	0.25	1.42
800	1.50	60	0.285	8.10	0.25	1.47
900	1.35	40	0.280	5.60	0.25	1.52
1000	1.15	20	0.275	5.00	0.25	1.65
1100	1.00	20	0.270	4.90	0.25	1.70
1200	1.00	20	0.267	4.90	0.25	1.62

$$\varepsilon_{ij} = \varepsilon_{ij}^e + \varepsilon_{ij}^p + \varepsilon_{ij}^c \quad (i, j = x, y, z). \tag{4}$$

The components of the stress and elastic strain tensors are related by Hooke's law:

$$\varepsilon_{ij}^e = \frac{\sigma_{ij} - \delta_{ij}\sigma}{2G} + \delta_{ij}(K\sigma + \varphi), \quad i, j = x, y, z, \tag{5}$$

where δ_{ij} is a unit tensor ($\delta_{ij} = 0$ if $i \neq j$, $\delta_{ij} = 1$ if $i = j$); $\sigma = \frac{1}{3}(\sigma_{xx} + \sigma_{yy} + \sigma_{zz})$; $G = \frac{E}{2(1+\nu)}$ is the shear modulus; $K = \frac{1-2\nu}{E}$ is the volume compressibility; E is the Young's modulus; ν is the Poisson's ratio; φ is the function of free relative elongations caused by temperature changes:

$$\varphi = \alpha(T - T_0), \tag{6}$$

α is the coefficient of relative temperature elongation of the material.

Plastic strains are related to the stress state by the equation of the theory of plastic non-isothermal flow and the associated Mises flow condition:

$$d\varepsilon_{ij}^p = d\lambda(\sigma_{ij} - \delta_{ij}\sigma), \quad i, j = x, y, z, \tag{7}$$

where $d\varepsilon_{ij}^p$ is the increment of the tensor ε_{ij}^p, which at a set time t is determined by the history of deformation, stresses σ_{ij} and temperature T; $d\lambda$ is the scalar function determined by the flow conditions:

$$d\lambda = 0, \text{ if } f = \sigma_i^2 - \sigma_T^2(T) < 0 \text{ or } f = 0 \text{ at } df < 0;$$
$$d\lambda > 0, \text{ if } f = 0 \text{ i } df > 0;$$
$$\text{the state f} > 0 \text{ is unacceptable,}$$

σ_i is the stress intensity; $\sigma_T(T)$ is the yield strength of the material at temperature T.

For the creep strains $d\varepsilon_{ij}^c$ the coupling equation in the form of [5] is used:

$$d\varepsilon_{ij}^c = \Omega(\sigma_i, T)(\sigma_{ij} - \delta_{ij}\sigma)dt, \tag{8}$$

where $\Omega(\sigma_i, T)$ is the scalar creep function of the material at temperature T and stress level determined by the stress intensity σ_i.

For this problem, when during heat treatment it is most important to take into account the creep strains $d\varepsilon_{ij}^c$ since the process of stress relieving significantly depends on them, it is rational to choose the function $\Omega(\sigma_i, T)$ on the basis of experiments on deformation at elevated temperatures of specimens of this material.

Accordingly, the creep function in general form as a function of material temperature, starting from a temperature of 550 °C and above, can be approximated by the typical dependence:

$$\Omega(\sigma_i, T) = A \cdot \sigma_i^n \cdot \exp\left(\frac{G}{T + 273}\right), \tag{9}$$

where A, G are constants related to material properties.

The presented model of creep at elevated temperatures is quite general and allows tracing deformation processes during heat treatment not only during holding, but also during heating and cooling at temperatures, for example, 550 °C and above. This model can be effective in simulating residual stress relaxation processes during local heat treatment of welded structures or in the case of furnace heat treatment with a short holding time, when uniform heating to a set holding temperature is not ensured over the volume of the welded structure or joint.

The coefficients of the creep function for the base material of the welded joint (10GN2MFA steel) were determined in [5] based on the processing of existing experimental data [18] in accordance with the degree of relaxation of residual tensile stresses σ_{xx} during the holding period t = 2 h of heat treatment after welding plates made of 10GN2MFA steel, depending on the tempering temperature T = 550–700 °C. Table 2 shows the results of calculating the constants of the creep function (8) using experimental data.

In the mathematical modeling of the stress-strain state in the considered joint, even in the absence of residual stresses before local heat treatment, it is advisable to take into account creep processes, since during local heat treatment, temporary temperature stresses are formed, under the influence of which, during long-term exposure at elevated temperatures, significant plastic strains can be formed by the creep mechanism.

The peculiarities of the mathematical model of non-isothermal deformation of the material during local thermal tempering of welded joint No. 111 at a maximum temperature of up to 650 °C are boundary conditions corresponding to the free fixation of the model; absence of structural phase changes and corresponding volume effects; stress relieving due to the processes of instantaneous ductility and temperature creep of the material, which is taken into account by the creep function $\Omega(\sigma_i, T)$. Since the residual welding stresses are not taken into account, the formation and development of new residual stresses during lo-

Table 2. Parameters of creep function $\Omega(\sigma_i, T)$ for 10GN2MFA steel in the temperature range 550 < T < 700 °C [5]

n	A, MPa$^{-(n+1)}\cdot$h^{-1}	G, °C
5	$8.46 \cdot 10^{17}$	–66394

cal heat treatment occurs due to a significant heating nonuniformity over the volume of the welded joint. During long-term holding (9 h), thermal stresses are partially relieved due to material creep and plastic strains are formed, which can also affect the level of residual stresses.

RESULTS OF THE SIMULATION

Figure 7 shows the distributions of maximum temperatures at holding during local postweld heat treatment in the high tempering mode at T = 650 °C, obtained for 2D and 3D models of welded joint No. 111. Due to the complex geometry of the joint, heating using locally arranged heaters does not ensure uniform temperature distribution in the welded joint zone during heat treatment (Figure 7).

From the point of view of ensuring the integrity of welded joint No. 111 under the stress corrosion failure mechanism, the distributions of circumferential and axial residual stresses on the inner surface of the joint is of particular importance. As a result, significantly nonuniform heating causes the formation of high residual stresses (Figure 8). On the inner surface, the circumferential stresses $\sigma_{\beta\beta}$ reach the level of 350 MPa, and on the outer surface — up to 300 MPa (Figure 8, *a*). The axial tensile stresses σ_{zz} on the inner surface reach 400 MPa, and the compressive stresses on the outer surface reach up to 300 MPa (Figure 8, *b*). The radial stresses in the zone of deposited metal are negligible, but a zone of rather high tensile stresses of up to 100 MPa is formed on the inner surface in the zone of radial transition of the pocket (Figure 8, *c*).

Figure 9 shows the calculated distributions of residual stresses over the thickness of welded joint No. 111 after local heat treatment (factory mode) without simulation of welding process (T = 650 °C, holding time t = 8 h), obtained using 2D and 3D models in comparison with existing data [11]. The results for the axial component σ_{zz} are quite similar in nature of distribution (Figure 9, *a*). Thus, according to the

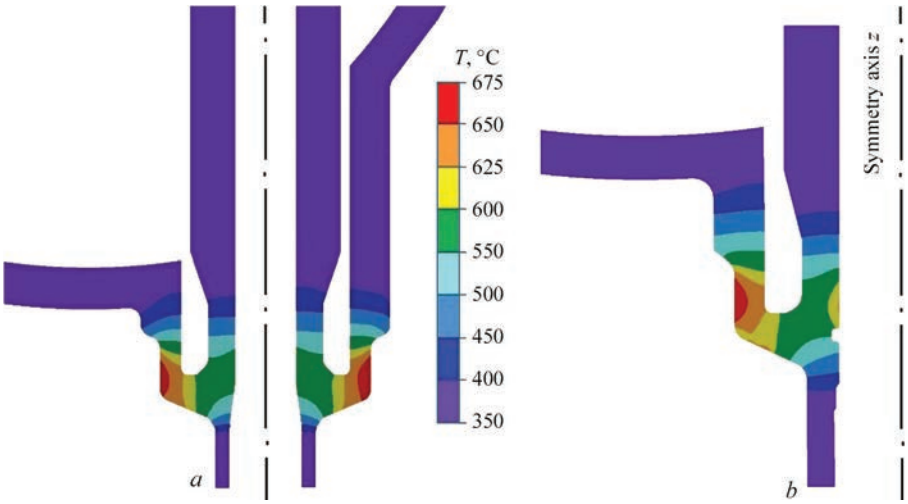

Figure 7. Distributions of maximum temperatures at holding during local heat treatment in the high tempering mode at T = 650 °C: *a* — 3D model, repair heat treatment mode; *b* — 2D model, factory heat treatment mode

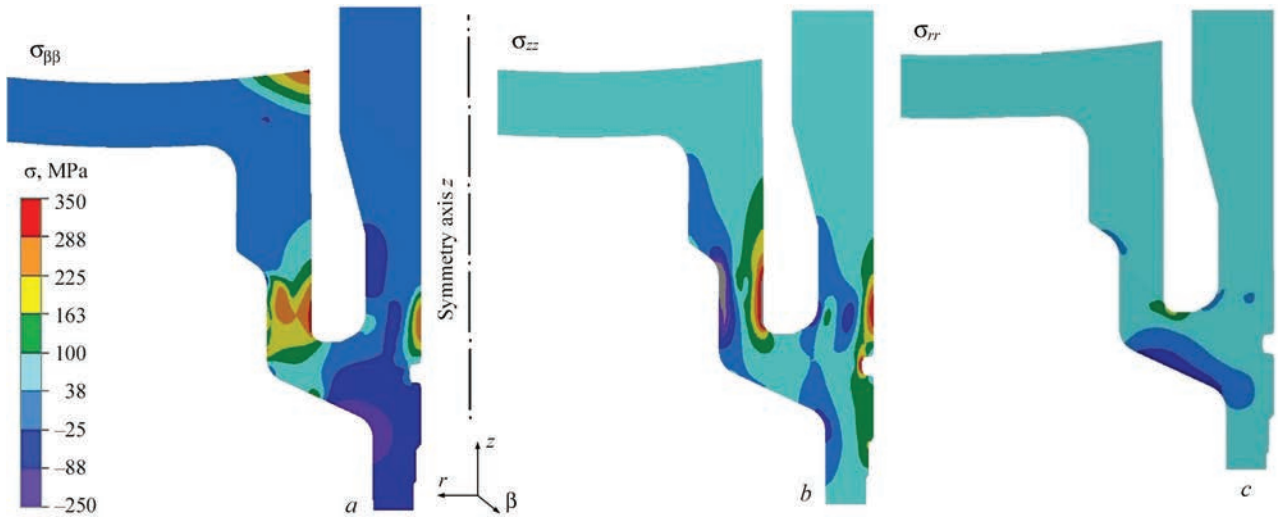

Figure 8. 2D model. Residual stresses in welded joint No. 111 after local heat treatment (factory heat treatment mode) without welding simulation (T = 650 °C, holding time t = 8 h), MPa: *a* — circumferential $\sigma_{\beta\beta}$; *b* — axial σ_{zz}; *c* — radial σ_{rr}

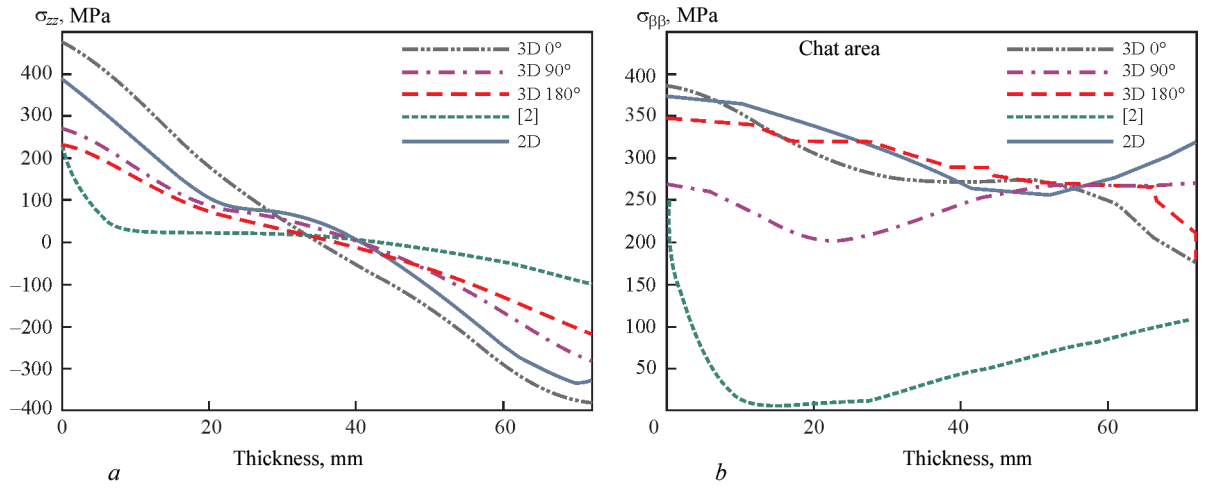

Figure 9. Distribution of residual stresses over the thickness of welded joint No. 111 after local heat treatment (factory mode) (T = 650 °C, holding time t = 8 h): *a* — axial component σ_{zz}; *b* — circumferential component $\sigma_{\beta\beta}$ (for the 3D model, the angular coordinate is calculated from the smallest nozzle length φ = 0°, respectively, the largest nozzle length corresponds to φ = 180°)

obtained data, on the outer surface of the joint, the axial residual stresses are compressive, and on the inner surface they are tensile, but differ significantly in absolute value. According to the existing data, tensile stresses reach 230 MPa, according to the results of the 2D model — almost 400 MPa, and the 3D model gives different values depending on the angular coordinates φ, namely, from 220 MPa in the area with a high nozzle height (φ = 180°) to 480 MPa in the area with a low nozzle height (φ = 0°).

As for the circumferential component $\sigma_{\beta\beta}$ (Figure 9, *b*), according to the existing data, the residual stresses on the inner surface of the joint are tensile of up to 250 MPa, and then drop sharply to almost zero values. The residual stresses obtained using 2D and 3D models are tensile over the entire thickness of the joint, but on the inner surface, according to the 2D model, they are up to 370 MPa, and according to the 3D model, they are from 270 MPa (φ = 180°) to 380 MPa (φ = 0°).

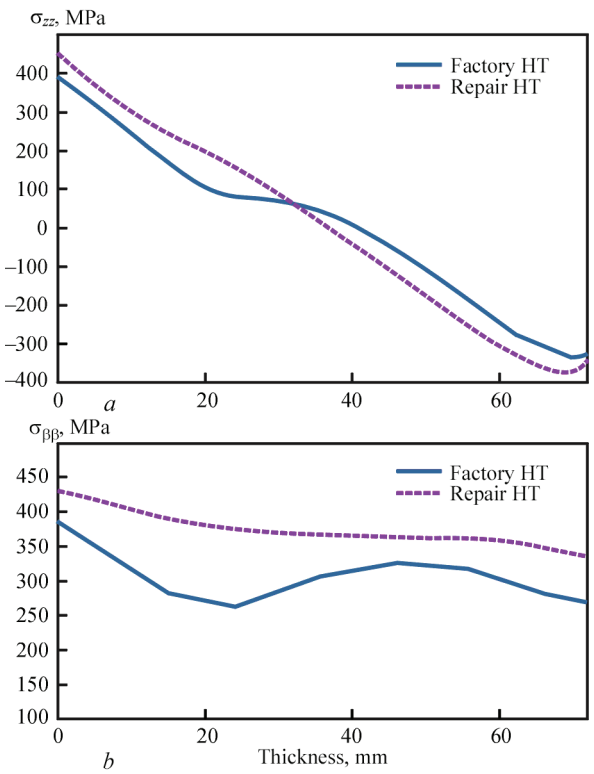

Figure 10. Distribution of residual stresses over the thickness of welded joint No. 111 after local factory or repair heat treatment (T = 650 °C, holding time t = 8 h): *a* — axial component σ_{zz}; *b* — circumferential component $\sigma_{\beta\beta}$

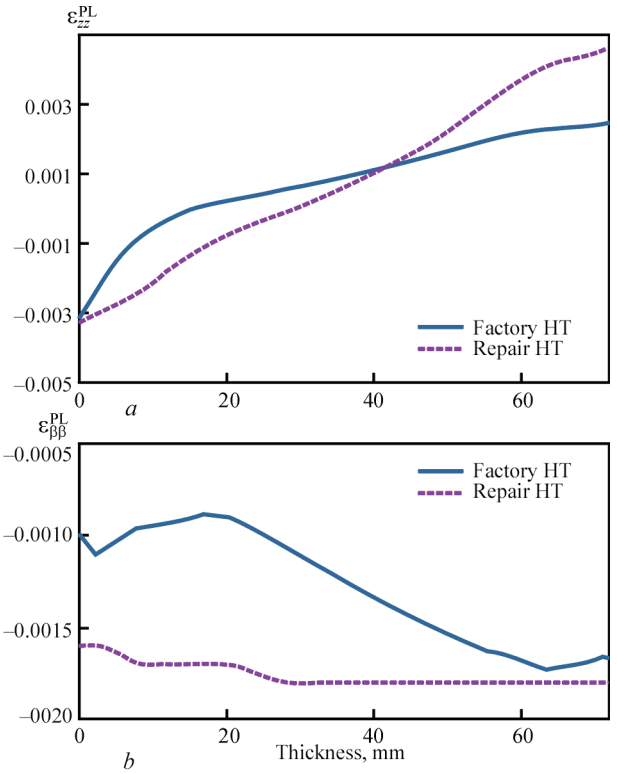

Figure 11. Distribution of plastic strains over the thickness of welded joint No. 111 after local factory or repair heat treatment (T = 650 °C, holding time t = 8 h): *a* — axial component ε_{zz}^{p}; *b* — circumferential component $\varepsilon_{\beta\beta}^{p}$

The presented results showed that, firstly, according to existing data [11], the residual tensile stresses on the inner surface of welded joint No. 111 after local heat treatment are significantly lower than those obtained in this study using 2D and 3D models. Secondly, the use of an axisymmetric 2D model with a short nozzle length provides rather conservative results compared to the 3D model.

Another problem investigated in this work is the difference in residual stresses after local heat treatment in the factory mode, when there is access to the inner surface of the collector, where an additional heater can be placed (Figure 2, *a*), and in the repair mode, when the heaters are located only on the outside of the joint (Figure 2, *b*).

Figures 10 and 11 show the calculated results obtained using the 2D model for the distributions of residual stresses and plastic strains over the thickness of welded joint No. 111 after local heat treatment according to the factory and repair heat treatment modes without simulation of welding process (T = 650 °C, holding time t = 8 h). It can be clearly seen that the repair local heat treatment is associated with a higher level of residual stresses on the inner surface of the joint, by about 10–15 %.

Assuming that the residual welding stresses relieving to a large extent at holding during heat treatment, new residual stresses are formed during cooling. This is especially true in the metal close to the inner surface, where rather high (up to 350–450 MPa) circumferential and axial residual tensile stresses are formed.

The presented results on the study of the effectiveness of the technology of local heat treatment of welded joint No. 111 showed that an unsuccessful choice or limited possibilities for the arrangement of heaters during local heat treatment can lead to negative consequences, namely, the formation of new residual tensile stresses in dangerous areas of the welded joint.

The obtained prediction results apply to all joints No. 111 of both hot and cold collectors, since individual deviations related to the size of the development, the number of passes, the parameters of the welding and heat treatment mode within the considered technological process do not significantly affect the final results. The low efficiency of the considered technology of postweld heat treatment and, possibly, even its negative impact on the integrity of welded joint No. 111 indicate the need in optimizing the technology of local heat treatment using mathematical modeling methods.

CONCLUSIONS

The results of mathematical modeling of the residual stresses of the welded joint of the collector to the DN1200 nozzle of the PGV-1000 steam generators (welded joint No. 111) as a result of local heat treatment under the high tempering mode without taking into account the residual stresses after welding showed that:

1. The inner surface of the joint in the area of welded joint No. 111 has rather high residual tensile stresses (up to 350–450 MPa) both in the circumferential and axial directions due to significant nonuniform heating over the thickness and creep processes during high temperature holding.

2. The axisymmetric 2D finite element model of the joint with a small nozzle DN1200 provides sufficient conservatism of the results compared to the 3D model, significantly reduces the requirements for computational resources and can be used to calculate residual stresses after multipass welding and subsequent local heat treatment.

3. Local heat treatment during the repair of welded joint No. 111 at NPP is associated with a higher level of residual tensile stresses on the inner surface of the joint (by about 10–15 %) than during the manufacture of the steam generator in the factory conditions, when it is possible to access the inner surface of the collector, where an additional heater can be placed.

4. An inappropriate choice or limited possibilities for the arrangement of heaters during local heat treatment of welded joint No. 111 can lead to negative consequences, namely the formation of new high residual tensile stresses in dangerous areas of the welded joint.

REFERENCES

1. Voyevodin, V.N., Ozhigov, L.S., Mitrofanov, A.S. et al. (2014) Identification of defects in the welded joint metal of the case of steam generator to the collector on the WWER-1000. *Voprosy Atomnoi Nauki i Tekhniki*, 4(**92**), 82–87 [in Russian].
2. Dub, A.V., Durynin, V.A., Razygraev, A.N. et al. (2014) Development of ultrasonic testing procedures and determination of performance of the assembly of the jpont of header to steam generator PGV-1000M. *Tekh. Diagnost. i Nerazrush. Kontrol*, **4**, 36–51 [in Russian].
3. Kharchenko, V.V., Chirkov, A.Yu., Kobel'skii, S.V., Kravchenko, V.I. (2017) Improving the computational analysis of stress-strain state and fracture resistance of welded joints between coolant headers and PGV-1000M steam generator vessel of nuclear power station. *Strength of Materials*, **49**, 349–360. DOI: https://doi.org/10.1007/s11223-017-9875-3
4. Makhnenko, V.I., Markashova, L.I., Makhnenko, O.V. et al. (2012) Growth of corrosion cracks in structural steel 10GN2MFA. *The Paton Welding J.*, **8**, 2–5.
5. Makhnenko, V.I. (2006) *Safe service life of welded joints and assemblies of modern structures*. Kyiv, Naukova Dumka [in Russian].
6. Stepanov, G.V., Shirokov, A.V. (2014) Assessment of the kinetics of crack propagation in the header-steam generator connector welded joint No. 111 by plasticity resource. *Strength of Materials*, **46**, 375–382. DOI: https://doi.org/10.1007/s11223-014-9559-1

7. Stepanov, G.V., Kharchenko, V.V., Babutskii, A.I. et al. (2003) Stress-strain state evaluation of a welded joint of hot collector to nozzle of NPP steam generator PGV-1000. *Strength of Materials*, **35**, 536–544. DOI: https://doi.org/10.1023/B:STOM.0000004543.31528.98
8. Kharchenko, V.V., Stepanov, G.V., Kravchenko, V.I. et al. (2009) Redistribution of stresses in the header-PGV-1000 steam generator connector weldment under loading after thermal treatment. *Strength of Materials*, **41**, 251–256. DOI: https://doi.org/10.1007/s11223-009-9130-7
9. Khodakovskii, A.A., Chirkov, A.Yu., Kharchenko, V.V. (2013) Calculation analysis of the stress-strain state of the collector-to-nozzle weld in the steam generator under seismic loading. *Strength of Materials*, **45**, 482–488. DOI: https://doi.org/10.1007/s11223-013-9483-9
10. Banko, S. (2012) Stressed state of the collector-case connection unit of the PGV-1000M steam generator with a cavity. *Visnyk Ternopilskoho NTU*, 67(**3**), 56–63 [in Ukrainian].
11. Stepanov, G.V., Kharchenko, V.V., Babutskii, A.I. (2006) Stress-strain state of the header-steam generator connector weldment induced by local thermal treatment. *Strength of Materials*, **38**, 595–600. DOI: https://doi.org/10.1007/s11223-006-0081-y
12. Muzhychenko, O.F., Makhnenko, O.V. (2019) Mathematical modeling of residual stresses in the collector to nozzle Du1200 welding unit of steam generators PGV-1000. In: *Proc. of the Intern. Conf. on Innovative Technologies and Engineering in Welding and Related Processes PolyWeld 2019, May 23–24, 2019, Kyiv*, 82–83.
13. Makhnenko, O.V., Milenin, O.S., Muzhychenko, O.F. et al. (2023) Mathematical modeling of residual stress relaxation during performance of postweld heat treatment. *The Paton Welding J.*, **6**, 32–40. DOI: https://doi.org/10.37434/tpwj2023.06.05
14. (2015) ASTM E837-13a. *Standard Test Method for Determining Residual Stresses by the Hole-Drilling Strain-Gage Method*. ASTM International.
15. Lobanov, L., Pivtorak, V., Savitsky, V., Tkachuk, G. (2014) Technology and equipment for determination of residual stresses in welded structures based on the application of electron speckle-interferometry. *Mat. Sci. Forum*, **768–769**, 166–173. DOI: https://doi.org/10.4028/www.scientific.net/MSF.768-769.166/
16. Rogante, M. (2020) Inside welds: Advanced characterization of residual stresses by neutron diffraction. *The Paton Welding J.*, **11**, 18–24. DOI: https://doi.org/10.37434/tpwj2020.11.04
17. Senchenkov, I.K., Chervinko, O.P., Banyas, M.V. (2013) Modeling of thermomechanical process in growing viscoplastic bodies with accounting of microstructural transformation: *Encyclopedia of Thermal Stresses*. *Springer Ref.*, **6**, 3147–3157.
18. Hrivnak, I. (1984) *Weldability of steels*. Ed. by E.L. Makarov. Moscow, Mashinostroenie [in Russian].

ORCID

O.V. Makhnenko: 0000-0002-8583-0163,
O.F. Muzhychenko: 0000-0002-4870-3659

CONFLICT OF INTEREST

The Authors declare no conflict of interest

CORRESPONDING AUTHOR

O.V. Makhnenko
E.O. Paton Electric Welding Institute of the NASU
11 Kazymyr Malevych Str., 03150, Kyiv, Ukraine.
E-mail: makhnenko@paton.kiev.ua

SUGGESTED CITATION

O.V. Makhnenko, O.F. Muzhychenko, I.I. Prudkiy, N.R. Basistyuk (2025) Residual stresses in the joint of the collector to the DN1200 nozzle of the PGV-1000 steam generator due to local heat treatment. *The Paton Welding J.*, **11**, 19–27. DOI: https://doi.org/10.37434/tpwj2025.11.03

JOURNAL HOME PAGE

https://patonpublishinghouse.com/eng/journals/tpwj

Received: 27.02.2025
Received in revised form: 18.05.2025
Accepted: 21.11.2025

DOI: https://doi.org/10.37434/tpwj2025.11.04

FEATURES OF THE STRESSED STATE OF WELDED ABSORBER ELEMENTS IN THE CONTROL AND PROTECTION SYSTEM OF WWER-1000 DURING ASSEMBLY AND SUBSEQUENT OPERATION

O.S. Milenin, O.A. Velykoivanenko, H.P. Rozynka, O.O. Makhnenko

E.O. Paton Electric Welding Institute of the NASU
11 Kazymyr Malevych Str., 03150, Kyiv, Ukraine

ABSTRACT

The control and protection system (CPS) with absorber elements (AE) plays a key role in the stable and safe operation of WWER-1000 reactor, ensuring power regulation and emergency shutdown. The reliability of CPS AE directly depends on the integrity of the AE shell components, which are subjected to both welding stresses during assembly and to operational loads. A critical reliability factor for such structures is the stress-strain state at various stages of assembly and operation. This study focuses on the analysis of the SSS in the AE shell components caused by the technological phase of assembly welding and operational loading. Numerical modeling of thermodeformational processes shows that the geometric characteristics of the structure result in the fundamental difference in the stress distribution: a biaxial stressed state forms in the area where the cone is welded to the AE shell, and a triaxial stressed state develops in the zone where the tip is joined to AE shell. It is shown that during reactor emergency shutdown and cooling to room temperature, there is a significant drop in the external coolant pressure and a sharp increase in the maximum stresses within the AE shell wall, indicating an increased risk of integrity loss.

KEYWORDS: nuclear reactor, WWER-1000, control and protection system, absorber elements, welded shells, stressed state, modeling

INTRODUCTION

Nuclear power plant operation is associated with the need to guarantee a high level of safety of both the individual components, and the entire cycle of energy generation. This concerns ensuring the integrity of the structures and components of nuclear reactors and accompanying process equipment, planned running of the processes of nuclear and related reactions, avoiding the release of radioactive substances into the environment, safety of service engineering personnel, etc. The complexity and interrelation of the physical and technological processes, as well as a considerable influence of the human factor necessitates a detailed and comprehensive study of the regularities of their impact on safe operation of nuclear reactors.

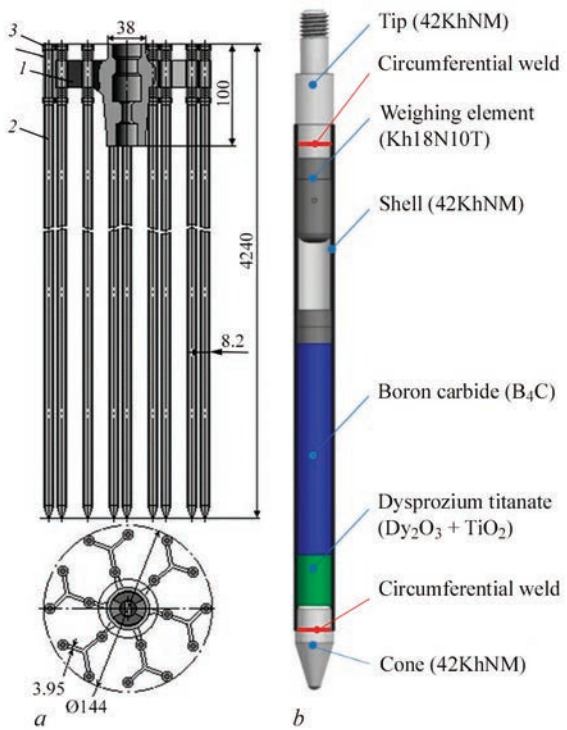

Figure 1. Sketches of CPS absorbing elements AE (*a*) and absorbing rod AR (*b*): *1* — head; *2* — AR; *3* — nut; *4* — spring

An important part of the reactor is the control and protection system (CPS), which includes the absorber elements (CPS AE) (Figure 1, *a*), which have a critical role in ensuring a stable and safe operation of the reactor, fulfilling a range of important functions [1, 2]. First, CPS allows precisely controlling and regulating the reactor power, ensuring its effective and safe operation. It is responsible for starting the reactor and gradual reaching of the specified power level, as well as a change of the reactor operating modes by switching from one power level to another one. Secondly, CPS ensures the possibility of prompt termination of the chain reaction of nuclear fission in the case of emergency situations or the need to quickly reduce the power. This is achieved by dropping the absorbing elements into the AE core, preventing further development of the reaction. Finally, CPS is an important element of general reactor safety, as its functioning

allows eliminating the probability of uncontrolled development of the nuclear reaction, thus preventing the possible emergencies.

Thus, ensuring safe operation of a nuclear reactor is directly related to guaranteeing the integrity of CPS components. The importance of this factor led to formulation of a range of regulatory requirements as to analysis of the technical state and serviceability of individual CPS components, in particular, strength and tightness of absorbing elements (AE) [3–5].

A feature of these AE is their complex profile and presence of assembly welded joints of the shell with the cone and tip. This, in its turn, determines the complex distribution of mechanical stresses under the operation conditions, caused by a nonlinear interaction of residual postweld stresses with the operational stresses. It is known that the magnitude of the stresses characterizes the proneness to brittle, brittle-ductile and fatigue fracture of structural materials [6–8]. Therefore, understanding of the regularities of stress distribution in the cross-section of shell CPS AE at different stages of operation is important for correct prediction of the reliability during design, technical diagnostics of the actual state and extension of the service life for the post-project period.

THE OBJECTIVE

of this study is determination of the influence of the process of assembly welding and thermal-force operational impact on the stress-strain state (SSS) of the shell elements of CPS AE.

AE (Figure 1, *b*) is a rod with a cylindrical shell from chromium-nickel alloy 42KhNM [9] with the outer diameter of 8.2 mm and wall thickness of 0.50–0.55 mm, hermetically sealed with end parts (tip which ensures connection to the CPS AE load-carrying system, and weighing cone) and filled with absorbing material [10].

Temperature dependencies of physical and mechanical properties of corrosion-resistant 42KhNM alloy are given in the Table 1. The yield strength of 42KhNM alloy during manufacture of seamless thin-walled cold-deformed pipes is specified at the level of σ_Y = 520 MPa at T = 20 °C, σ_Y = 245 MPa at T = 375 °C.

The shell sealing is performed by electric arc welding of the upper and lower end parts in inert gas atmosphere. Located inside the shell is an absorber element from a dispersion material, such as boron carbide (B_4C) and dysprosium titanate (Dy_2O_3 + TiO_2) in an aluminium matrix or hafnium [11]. Depletion of these elements and their swelling leads to development of excess internal pressure P_{int} inside the cylindrical shell (close to 3.0 MPa) and under certain

Table 1. Temperature dependencies of physical and mechanical properties of 42KhNM alloy [9]

T, °C	E, GPa	$\alpha \cdot 10^6$, 1/°C	λ, W/(cm·°C)	$c\rho$, J/(cm^3·°C)
20	234	14.5	0.050	3.550
100	223	15.0	0.100	3.686
200	218	15.6	0.130	3.800
300	210	16.0	0.150	3.854
400	204	16.6	0.180	3.955
500	196	17.0	0.205	3.991
600	188	17.5	0.230	4.040
700	143	18.0	0.230	4.043
800	135	18.5	0.230	4.113
900	118	19.0	0.230	4.115
1000	96	19.5	0.230	4.115
1100	46	19.5	0.230	4.115
1200	8	19.5	0.230	4.115

conditions it affects the load-carrying capacity and quantitative indices of the technical state. According to the design conditions of AE operation, there is the external pressure of the coolant P_{ex} = 16 MPa at the temperature of T_0 = 350 °C. In addition to the design mode, it is also necessary to take into account the situation of emergency shutdown of the reactor, when P_{ex} drops to zero, and the temperature decreases to room temperature, T_0 = 20 °C. Summing up the above-said, we can single out three characteristic states of CPS AE, namely: after assembly welding, under the conditions of design operation in the stationary mode and in case of reactor shut-down and its cooling.

As was noted above, a typical characteristic of reliability of critical elements of power-generating equipment, which is determined during assessment of the reactor condition, is the level of mechanical stresses, formed at different stages of operation. For the case of shell CPS AE stress distribution in the structure cross-section is determined by interaction of postweld stresses with external loading and temperature influence. Therefore, in order to predict the stress fields, it is necessary to take into account both the technological aspect of assembly welding, i.e. kinetics of the thermodeformational state of the structure material under the impact of the local heat source down to complete cooling and reaching the residual state, and further heating and loading during operation.

Spatial heterogeneity and nonlinear kinetics of the physical and mechanical processes, which determine the current and residual SSS of the structure during assembly welding and further operation, complicates the use of simplified analytical methods of analysis. More over, small scale of CPS AE components and their geometric shape make the use of instrumental NDT methods more complicated. Therefore, it is expedient to apply the methods of mathematical

modeling and computer simulation of the respective technological processes based on multiphysical mathematical models and finite element means of their numerical implementation.

In this paper the problem of numerical prediction of the temperature field kinetics and development of elastoplastic deformations was considered within the framework of formulation of the boundary problem of nonstationary thermoplasticity. The temperature field kinetics was described by numerical solution of the nonstationary heat-conductivity equation, namely [12]:

$$c\rho(r,\beta,z,T)\frac{\partial T(r,\beta,z)}{\partial \tau} = \nabla\left[\lambda(r,\beta,z,T)\nabla T(r,\beta,z)\right], \quad (1)$$

where λ, $c\rho$ is the heat conductivity and volumetric heat capacity of the structure material in this point, respectively, as a function of spatial coordinates and temperature.

The heat source is the Gaussian surface heat flux from the welding arc into the area of the assembly joint of the tip with the shell and of the cone with the shell. Heat dissipation through the surface in welding occurs due to Newton–Richmann's (convective heat transfer) and Stefan–Boltzmann laws (infrared radiation), and it is described by the respective heat flows. Thus, the boundary conditions as to the formulated problem (1) are as follows [12]:

$$-\lambda(T)\frac{\partial T}{\partial n} = -q_W + \alpha_T(T - T_C) + \varepsilon\sigma_{SB}\left(T^4 - T_C^4\right), \quad (2)$$

where n is the normal to the surface; a_T is the heat transfer coefficient; T_C is the ambient temperature; ε is surface emissivity; σ_{SB} is the Stephan-Boltzmann constant; q_W is the welding heat energy flow.

Mathematical consideration of the unified problem of the kinetics of the temperature field and SSS development is based on the finite element description, using eight-node finite elements (FE). Within the FE volume, the distributions of temperatures, stresses and strains are taken to be homogeneous, and the increment of the strain tensor can be represented according to the following expression [13]:

$$d\varepsilon_{ij} = d\varepsilon_{ij}^e + d\varepsilon_{ij}^p + \delta_{ij}d\varepsilon_T, \quad (3)$$

where $d\varepsilon_{ij}^e, d\varepsilon_{ij}^p, \delta_{ij}\cdot d\varepsilon_T$ are the components of strain tensor increment, due to the elastic mechanism of deformation, instantaneous plasticity strains and kinetics of a heterogeneous temperature field, respectively.

Tensors of mechanical stresses σ_{ij} and elastic strains $d\varepsilon_{ij}^e$ are related to each other by the generalized Hooke's law, i.e. [14]:

$$\varepsilon_{ij}^e = \frac{\sigma_{ij} - \delta_{ij}\sigma}{2G} + \delta_{ij}(K\sigma + \varphi), \quad (4)$$

where σ is the mean value of normal components of stress tensor σ_{ij}, i.e. $\sigma = \frac{(\sigma_{\beta\beta} + \sigma_{zz} + \sigma_{rr})}{3}$, $K = \frac{1-2\nu}{E}$ is the bulk modulus, G is the shear modulus.

Increment of instantaneous plasticity strain $d\varepsilon_{ij}^p$ from the stressed state in a specific FE can be calculated using a linear dependence of scalar function Λ and deviator component of the stress tensor, namely [14]:

$$d\varepsilon_{ij}^p = d\Lambda(\sigma_{ij} - \delta_{ij}\sigma). \quad (5)$$

Specific value of function Λ depends on the stressed state in the considered area of the structure, as well as on the shape of the material yield surface, which is characterized by stresses σ_x:

$$d\Lambda = 0, \text{ if } \sigma_i < \sigma_s,$$
$$d\Lambda > 0, \text{ if } \sigma_i = \sigma_s,$$
$$\text{state } \sigma_i > \sigma_s \text{ is inadmissible.} \quad (6)$$

Proceeding from the above, the increments of the strain tensor can be represented in the form of superposition of the increment of the respective components:

$$\Delta\varepsilon_{ij} = \Psi\left(\sigma_{ij} - \delta_{ij}\sigma\right) + \delta_{ij}\left(K\sigma + \Delta\varepsilon_T\right) - \frac{1}{2G}\left(\sigma_{ij} - \delta_{ij}\sigma\right)^* - \left(K\sigma\right)^*, \quad (7)$$

where symbol "*" refers the respective variable to the previous tracking step; Ψ is the function of the material state, which determines the condition of plastic flow of the material according to von Mises criterion [15]:

$$\Psi = \frac{1}{2G}, \text{ if } \sigma_i < \sigma_s = \sigma_Y,$$
$$\Psi > \frac{1}{2G}, \text{ if } \sigma_i = \sigma_s,$$
$$\text{state } \sigma_i > \sigma_s \text{ is inadmissible.} \quad (8)$$

Function Ψ is determined by iteration at each step of digital tracing within the boundary problem of nonstationary thermoplasticity, which allows solving the nonlinearity by the plastic yield of the material.

Computer implementation of the given algorithms allowed performing analysis of the regularity of

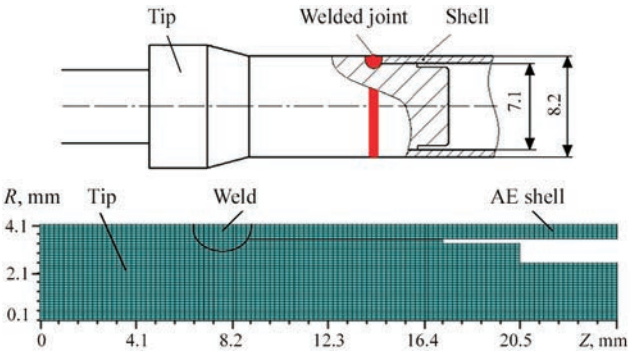

Figure 2. Sketch and finite element model of a welded joint of CPS AE shell with a tip [10]

formation of CPS AE SSS at the stage of assembly welding and further operation. Welding the tip to the shell (Figure 2) in an argon atmosphere is performed in the following mode according to [10]: U = 120 V; I = 20 A; v_w = 13 m/h. Welding of the assembled cone to the shell (Figure 3) in an argon atmosphere occurs in the following mode: U = 10 V; I = 30 A; v_w = 12 m/h.

As shown by the calculation results (Figure 4, *a*), the shape of penetration in the area of joining the cone to the shell of the AE ensures a proper permanent joint of these components. Residual postweld stresses are characterized by an increase in the normal stresses in the circumferential ($\sigma_{\beta\beta} \approx 590$ MPa) and axial ($\sigma_{zz} \approx 540$ MPa) directions in the area close to the middle of the cone wall thickness (Figure 5). In addition, the zone of tensile stresses extends right up to the internal surface of the shell in the area of the joint with the cone. Contrarily, the external surface is characterized by compressive normal stresses. The maximum values of circumferential stresses are close to those of the material yield strength, according to von Mises plasticity criterion. In contrast to this, the radial component of stress is almost five times lower ($\sigma_{rr} \approx 105$ MPa). Such a biaxiality of the stress field, in general, is characteristic for the cylindrical shell el-

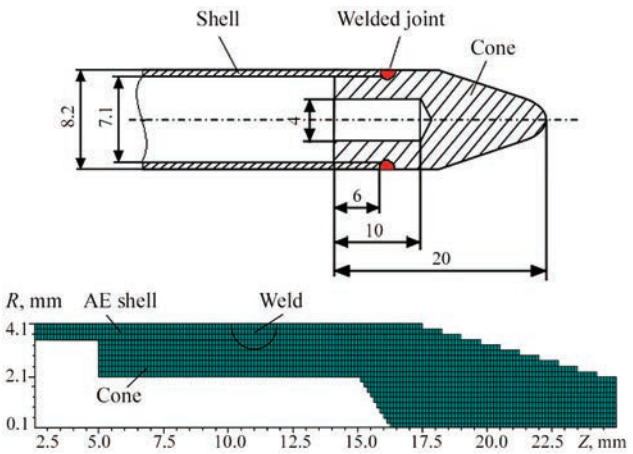

Figure 3. Sketch and finite element model of a welded joint of the CPS AE shell with the cone [10]

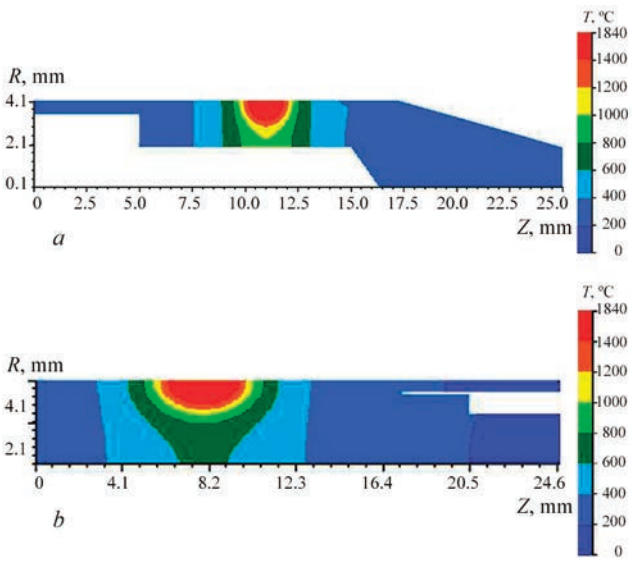

Figure 4. Calculated distribution of maximum temperatures in the zone of the welded joint of CPS AE shell with the cone (*a*) and with the tip (*b*)

ements, joined by a circumferential weld, while the features of stress distribution are due to the ratio of the wall thickness to the cylinder radius.

Under operating load conditions according to the design stationary mode (T_0 = 350 °C, P_{ex} = 16 MPa, P_{int} = 3 MPa) the stress distribution does not change in principle (Figure 6). However, a certain reduction of maximum stresses ($\sigma_{\beta\beta} \approx 500$ MPa, $\sigma_{zz} \approx 470$ MPa, $\sigma_{rr} \approx 85$ MPa) is observed, caused by the natural lowering of the yield strength at the temperature of

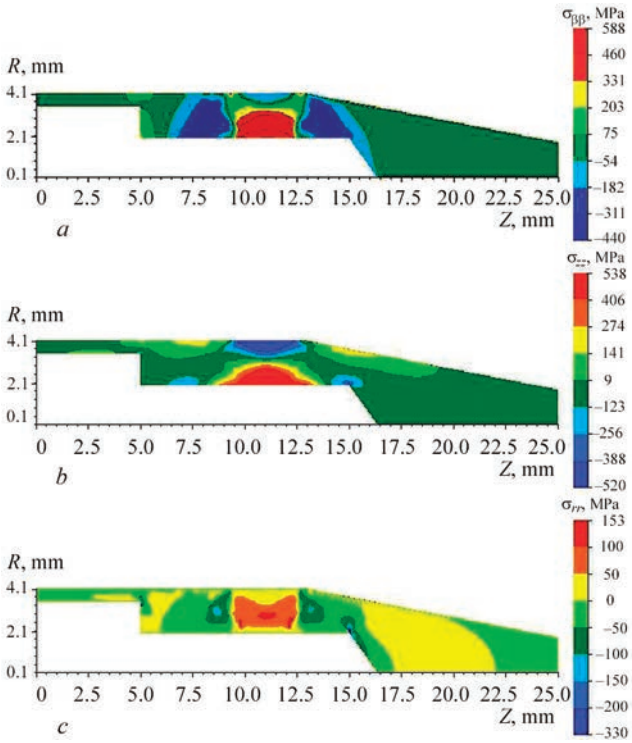

Figure 5. Calculated distributions of residual postweld stresses in the zone of the welded joint of the cone with CPS AE shell: *a* — circumferential component; *b* — axial component; *c* — radial component

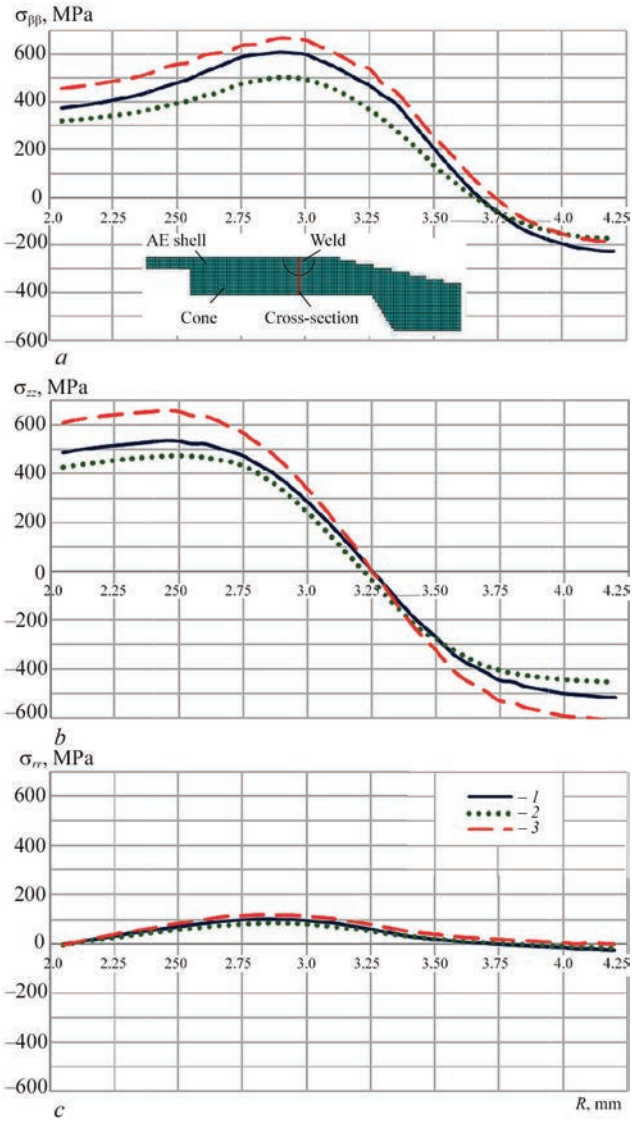

Figure 6. Calculated distributions of residual and operational stresses in the cross-section of the welded joint of the cone with the AE shell; circumferential (*a*), axial (*b*), radial (*c*): *1* — residual stresses; *2* — T_0 = 350 °C, P_{int} = 3 MPa, P_{ext} = 16 MPa; *3* — T_0 = 20 °C, P_{int} = 3 MPa

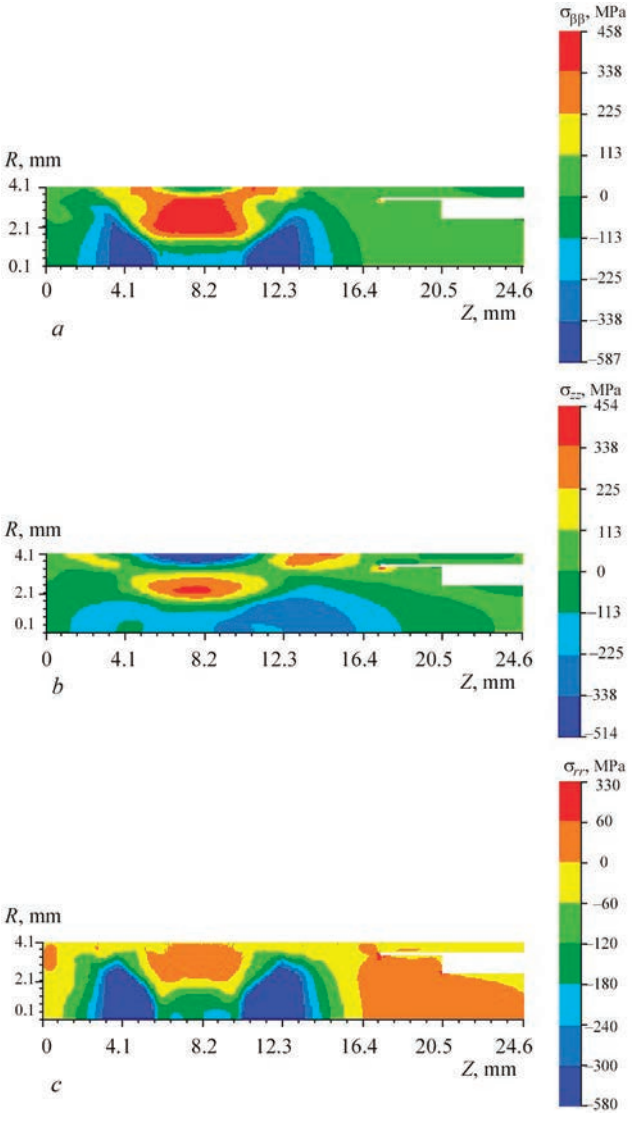

Figure 7. Calculated distributions of residual postweld stresses in the zone of the welded joint of the tip with the CPS AE shell: circumferential (*a*), axial (*b*) radial (*c*)

350 °C, compared to room temperature, at which the process of assembly welding was conducted. The operational situation of reactor shutdown, CPS AE cooling to room temperature and lowering of external pressure (P_{int} = 3 MPa, P_{ext} = 0 MPa, T_0 = 20 °C) leads to a significant increase of maximum stresses ($\sigma_{\beta\beta} \approx 670$ MPa, $\sigma_{zz} \approx 660$ MPa, $\sigma_{rr} \approx 120$ MPa) in the shell wall (Figure 6) for the reason that the internal pressure from the filler is not compensated by the external pressure of the coolant, so that it can be considered as the most unfavourable in terms of strength of the welded joint of AE shell with the cone.

Distribution of maximum temperatures in the area of joining the tip to the shell demonstrates significant penetration, which ensures a proper permanent joint of individual parts (Figure 4, *b*). A fundamental difference in the residual stress distribution (Figure 7) is the fact that the welded joint is located in the CPS AE solid part, so that the area of high postweld circumferential and axial stresses forms in the subsurface zone, where maximum lowering of the joint strength is to be expected. In addition, compared to the welded joint of the shell with the cone a lower level of maximum residual stresses is observed ($\sigma_{\beta\beta} \approx 460$ MPa, $\sigma_{zz} \approx 350$ MPa, $\sigma_{rr} \approx 35$ MPa).

Similar to the case of the area of the joint of the cone with the shell, under the conditions of design operation a certain lowering of stresses ($\sigma_{\beta\beta} \approx 420$ MPa, $\sigma_{zz} \approx 300$ MPa, $\sigma_{rr} \approx 10$ MPa) is observed in the area of the joint of the tip with the shell (Figure 8), while the most hazardous stressed state develops during reactor shutdown (Figure 8), when there are no compensating compressive forces from external pressure, while redistribution of stresses with increase of the yield strength as a result of temperature lowering from 350 °C to room temperature causes an increase of nor-

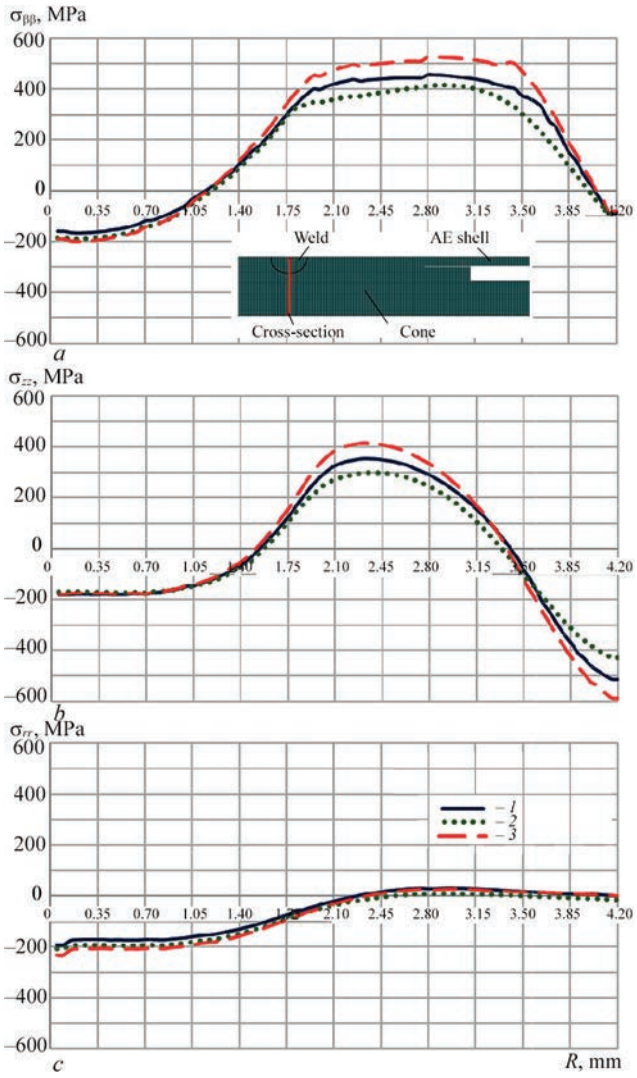

Figure 8. Calculated distributions of residual and operational stresses in the cross-section of a welded joint of the AE tip with the shell: circumferential (*a*), axial (*b*), radial (*c*): *1* — residual stresses; *2* — T_0 = 350 °C, P_{int} = 3 MPa, P_{ext} = 16 MPa; *3* — T_0 = 20 °C, P_{int} = 3 MPa

mal stresses by more than 100 MPa ($\sigma_{\beta\beta} \approx 530$ MPa) $\sigma_{zz} \approx 410$ MPa, $\sigma_{rr} \approx 30$ MPa).

CONCLUSIONS

1. A model was developed of the kinetics of the temperature field and stress-strain state of CPS AE of WWER-1000 during assembly welding of the cone to the AE shell and of the tip to the AE shell was developed. Used for this purpose, was a numerical solution of a nonstationary equation of heat conductivity alongside with successive tracking of the development of elastoplastic strains of a continuous medium by finite element solution of the boundary problem of nonstationary thermoplasticity.

2. It is shown that development of a thermodeformational state of CPS AE structure during welding of the cone to the shell leads to formation of a biaxial SSS, characteristic for welding thick-walled pipes, with considerable prevalence of circumferential and longitudinal stresses. In the zone of connection of the CPS AE tip to the shell, the weld is located in the solid part of the structure which leads to formation of a subsurface area of intensive postweld circumferential and axial stresses. The maximum radial stresses rise to the level of other components of the stress tensor. As a result, this area of the structure is in the state of triaxial stress.

3. During operation, the total pattern of stress distribution is preserved, but their maximum values become lower. This phenomenon is related to the fact that at the working temperature of 350 °C the material yield strength decreases, compared to its room temperature value, at which assembly welding was performed. As a result, the material becomes more susceptible to plastic strains, which promotes partial redistribution of stresses.

4. During the reactor shutdown and its cooling to room temperature a significant lowering of the external pressure takes place. As the internal pressure of the filler is no longer balanced by the coolant pressure, it causes an abrupt increase of maximum stresses in the wall of CPS AE shell. Such a situation creates the most unfavourable conditions for strength of welded joints, increasing the risk of defect development and deterioration of the operational reliability of the structure.

REFERENCES

1. Misak, J. (2024) History, specific design features, and evolution of WWER reactors. *Nuclear Power Reactor Designs: From History to Advances*, **2024**, 57–91. DOI: https://doi.org/10.1016/B978-0-323-99880-2.00004-7
2. Pyrohov, T., Korolev, A., Inyushev, V., Kurov, V. (2020) Analysis of accidents of the WWER-1000 reactor in which emergency cooling heat exchangers operate. *Technology Audit and Production Reserves*, 5(**55**), 43–47. DOI: https://doi.org/10.15587/2706-5448.2020.213227
3. (2013) *Guidelines for integrity and lifetime assessment of components and piping in WWER nuclear power plants* (VERLIFE). Vienna, Int. At. Energy Agency.
4. PNAE G-7-002–86: *Standards for strength calculation of equipment and pipelines of nuclear power installations* [in Ukrainian].
5. (2016) API 579-1/ASME FFS-1: Fitness-For-Service. Washington, American Petroleum Institute, American Society of Mechanical Engineers.
6. Lemaitre, J., Desmorat, R. (2005) *Engineering damage mechanics. Ductile, creep, fatigue and brittle failures*. Berlin, Springer-Verlag.
7. Amsterdam, E., Grooteman, F. (2016) The influence of stress state on the exponent in the power law equation of fatigue crack growth. *Inter. J. Fatigue*, 82(**3**), 572–578. DOI: https://doi.org/10.1016/j.ijfatigue.2015.09.013
8. Dormieux, L., Kondo, D. (2016) *Micromechanics of fracture and damage*. Vol. 1. London: ISTE Ltd.
9. (1967) *Physical properties of steels and alloys used in power engineering:* Refer. Book. Ed. by B.E. Neimark. Moscow, Energiya [in Russian].
10. Kushtym, A.V., Zihunov, V.V., Hrytsyna, V.M. et al. (2023) Characteristics of welded joints of absorbing elements from

42KhNM alloy for control and protection system rods of WWER-1000. *Yaderna ta Radiatsiina Bezpeka*, 4(**100**), 38–48 DOI: https://doi.org/10.32918/nrs.2023.4(100).04 [in Ukrainian].
11. Risovani, V.D., Zakharov, A.Z., Muraleva, E.M. et al. (2019) Dysprosium hafnate as absorbing material for control rods. *J. of Nuclear Materials*, 355(**1–3**), 163–170. DOI: https://doi.org/10.1016/j.jnucmat.2006.05.029
12. Karkhin, V.A. (2019) *Thermal processes in welding*. Singapore, Springer Singapore.
13. Velikoivanenko, E.A., Milenin, A.S., Rozynka, G.F. et al. (2019) Prediction of susceptibility of welded joints of titan γ-aluminide based alloy to cold cracking in electron-beam welding. *Tekhnologicheskie Sistemy*, **3**, 73–80. DOI: https://dx.doi.org/10.29010/88.9
14. Velikoivanenko, E.A., Milenin, A.S., Popov, A.V. et al. (2019) Methods of numerical forecasting of the working performance of welded structures on computers of hybrid architecture. *Cybernetics and Systems Analysis,* 55(**1**), 117–127. DOI: https://doi.org/10.1007/s10559-019-00117-8
15. Makhnenko, V.I. (2006) *Safe operation resource of welded joints and assemblies of modern structures. Kyiv*, Naukova Dumka [in Russian].

ORCID
O.S. Milenin: 0000-0002-9465-7710,
O.A. Velykoivanenko: 0009-0007-3704-2000,
H.P. Rozynka: 0009-0009-1750-7266,
O.O. Makhnenko: 0000-0003-2319-2976

CONFLICT OF INTEREST
The Authors declare no conflict of interest

CORRESPONDING AUTHOR
O.S. Milenin
E.O. Paton Electric Welding Institute of the NASU
11 Kazymyr Malevych Str., 03150, Kyiv, Ukraine.
E-mail: asmilenin@ukr.net

SUGGESTED CITATION
O.S. Milenin, O.A. Velykoivanenko, H.P. Rozynka, O.O. Makhnenko (2025) Features of the stressed state of welded absorber elements in the control and protection system of WWER-1000 during assembly and subsequent operation.
The Paton Welding J., **11**, 28–34.
DOI: https://doi.org/10.37434/tpwj2025.11.04

JOURNAL HOME PAGE
https://patonpublishinghouse.com/eng/journals/tpwj

Received: 10.06.2025
Received in revised form: 24.07.2025
Accepted: 19.11.202

DOI: https://doi.org/10.37434/tpwj2025.11.05

USE OF THE HOUGH TRANSFORMATION METHOD FOR THE METALLOGRAPHIC STUDIES OF FERRITIC-BAINITIC STEELS MICROSTRUCTURE

V.V. Holovko[1], **O.O. Shtofel**[1,2], **D.Yu. Korolenko**[1]

[1]E.O. Paton Electric Welding Institute of the NASU
11 Kazymyr Malevych Str., 03150, Kyiv, Ukraine
[2]National Technical University of Ukraine "Igor Sikorsky Kyiv Polytechnic Institute"
37 Prosp. Beresteiskyi, 03056, Kyiv, Ukraine

ABSTRACT

High-strength low-alloy steels are a promising material for the manufacture of welded metal structures, but their widespread use is hampered by their increased susceptibility to defects that arise during the welding process. Therefore, a fundamental aspect of developing the technology for welding these steels is understanding how the properties of the metal change during the welding process and identifying the main microstructural characteristics that explain these changes. Research on high-strength ferritic-bainitic steels, which concerns the microstructural characteristics and mechanical properties, is aimed at determining the total angle of structural grains misorientation, using the electron backscatter diffraction (EBSD) method, which can be implemented on electron microscopes, and requires special software installation. The metallographic analysis method using the Hough transformation, which can be implemented on optical microscopes and does not require special software, should be considered as an alternative to the EBSD method.

KEYWORDS: high-strength low-alloy steel, welding, microstructure, metallographic analysis, grain boundaries, structural grains misorientation, Hough transformation

INTRODUCTION

Recently, in Ukrainian industry, there has been a significant increase in the volume of work involving the use of high-strength low-alloy steels (HSLA) manufactured at leading metallurgical enterprises in the EU, Great Britain, USA, and Canada. Working with such materials presents new challenges for both industrial engineers and researchers. Preliminary results have shown that the complex of mechanical properties of modern foreign high-strength steels can be significantly superior compared to traditional domestically produced steels. A limiting factor for steels with higher strength is their increased susceptibility to defect formation resulting from welding. Therefore, a fundamental aspect of developing welding technology for these materials is understanding how the metal properties change during the welding process and identifying the main microstructural characteristics that explain these changes.

It is generally known that the mechanical properties of metallic materials correlate with microstructural dimensions, most commonly with the average grain size, according to the Hall–Petch relationship [1, 2]:

$$\sigma = \sigma_0 + kd^{1/2},$$

where σ_0 is the lattice friction stress required to move individual dislocations; k is a material-dependent constant known as the slope of the Hall–Petch curve; d is the average grain size. The Hall–Petch relationship applies to a wide variety of materials and their properties, such as hardness, stress-strain state properties, and endurance limit [3, 4]. However, in addition to the average grain size, for weld metal characterized by stochastic grain orientation, it is necessary to consider other specific factors, such as differences in the orientation of ferrite plates within the body of structural grains, in order to predict material properties in the general case.

It is known that the strength and toughness of most steels at low temperatures can be improved through grain refinement during a controlled thermomechanical process. Numerous studies have shown that under the influence of thermal cycles, due to the peculiarities of metal crystallization process, anisotropy of structural and mechanical properties of the metal may occur, particularly low-temperature toughness, which may impose certain limitations on the selection of technological parameters for its processing [5–7]. Most studies on HSLA steels concern the microstructural characteristics and mechanical properties of the metal [8, 9], whereas the relationship between structural grain size, their orientation, and fracture toughness is still far from being understood due to the complex ferritic-bainitic-martensitic microstructure and the absence of a macroscopic numerical value that reflects this relationship.

Due to the fact that HSLA steels have an increased susceptibility to brittle fracture, the design of their welding technology requires the development of specific mechanisms that suppress crack formation and growth. Although microscopic defects, such as initial crack nuclei, are always present in weld metal, particular attention must be paid to mechanisms that help prevent their formation and branching, arrest their propagation, or even close cracks that are capable of growing or have already begun to grow. A fundamental review [10] demonstrates (Figure 1) that for HSLA steels, internal interfaces represent a relatively weak link with respect to crack formation and growth. This is related to the fact that elementary crack growth occurs through delamination and dislocation emission at the crack tip, that is, through decohesion of atomic bonds and the material's ability to create a zone of plastic relaxation around the propagating crack tip. Due to lower lattice coherency in grain boundary zones compared to their interior, cracks in high-strength steels can often propagate more easily along grain boundaries than through their interior.

Plastic slip at intergranular boundaries is determined by the competition between three microforces at the interface: the volume-induced microforce associated with bulk densities; the dissipative microforce associated with resistance to slip at the interface; and the energetic microforce associated with the Burgers vector of the network, which tends to counteract the accumulation of residual defects at the interface. Greater misorientation of adjacent grains retards normal slip at the interface and reduces the slip rate, increasing the strain hardening rate. At smaller grain sizes, larger deformation gradients develop, leading to the initiation of slip at the interface at lower shear strain.

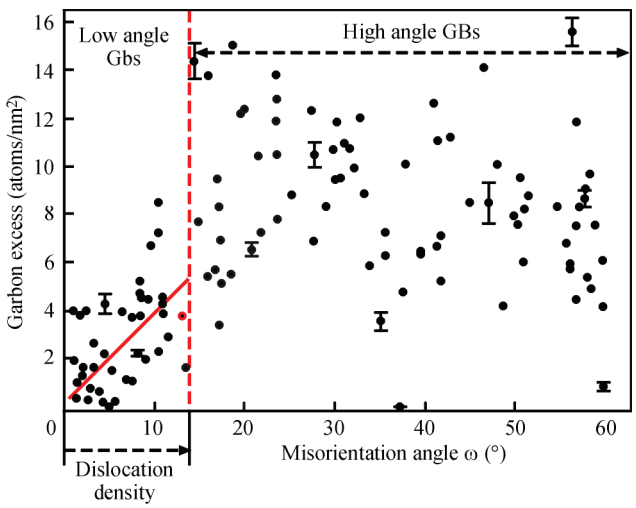

Figure 1. Schematic method for quantitative assessment of carbon segregation in ferrite [10]

The current viewpoint of some researchers is that the structural units that affect the toughness of ferritic-bainitic steels are grains with misorientation angles at grain boundaries greater than 15°. This is related to the fact that high-angle grain boundaries (HAGBs) with grain boundary misorientation angles greater than 15° are effective grains that contribute to crack arrest or its deflection at a large angle upon encountering an intergranular boundary during crack propagation [11, 12]. For BCC metals, a cleavage crack always propagates along {100} cleavage planes. The angles between adjacent grains will affect the ability to change the crack propagation direction, which is confirmed by the nature of fracture facets. For example, the authors of [13, 14] found that structural blocks with low grain boundary misorientation angles less than 15° (LAGBs) are microstructural units that control cleavage fracture and the increase in ductile-to-brittle transition temperature.

Direct studies of the effect of grain boundary misorientation on hydrogen transport, the results of which are presented in [15], showed that grain boundaries are pathways with high flux of dislocations and associated hydrogen, where the flux magnitude typically increases with increasing trap binding energy at grain boundaries. Modeling of hydrogen penetration in the early stages of deformation showed (Figure 2) that high-angle grain boundaries are faster pathways than low-angle ones.

It should be noted that currently, the volume of experimental data is insufficient to establish a relationship between toughness and structure in different directions of acicular ferritic-bainitic steels through analysis of {100} cleavage plane angles.

A large number of experiments show that cracks can propagate both directly through structural grains and through grain boundaries. Therefore, the effective grain size d according to the Hall–Petch relationship requires certain refinements with respect to ferritic-bainitic structures of HSLA steels. According to Professor Derek Raabe and colleagues from the Max Planck Institute in Düsseldorf [16], proper understanding and quantitative characterization of various interrelated effects of grain boundaries and associated effects are conditions for nanoscale engineering of damage-resistant HSLA steels.

In metallographic studies, the electron backscatter diffraction (EBSD) method is used as a criterion for characterizing grain boundaries to determine the overall misorientation angle of structural grains — an analytical method integrated with a scanning electron microscope. EBSD is a powerful microstructure characterization method that allows obtaining important information about grain orientation, phase identifica-

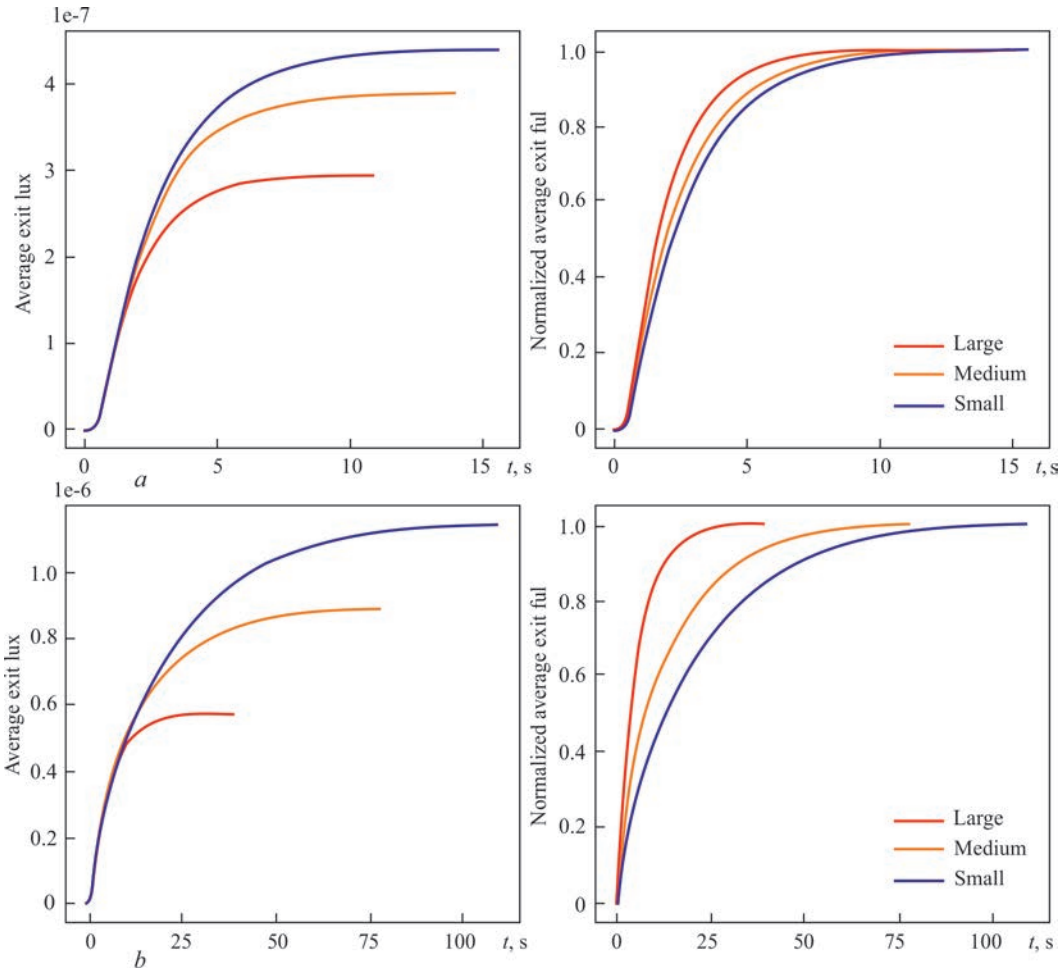

Figure 2. Curves of average and normalized output flux through low-angle (*a*) and high-angle (*b*) grain boundaries [15]

tion, and local deformation distribution. The method plays an increasingly important role in improving our understanding of material behavior. Modern computer programs for EBSD analysis allow processing of high-resolution images, enabling the analysis of fine-scale microstructures and obtaining detailed grain boundary characteristics. In addition, EBSD allows measurement of orientation gradients, which are necessary for understanding deformation mechanisms.

The EBSD method is widely used for characterizing the microstructure of martensitic and bainitic steels, allowing understanding of phase transformations and grain boundary characteristics. These capabilities are crucial for optimizing the mechanical properties of steels, such as strength, toughness, and ductility [17–20].

Reference [21] provides an example of automated identification and quantitative statistical analysis of bainite microstructural boundaries using EBSD data. The results indicate that crystallographic differences between different bainitic and martensitic structures provide a theoretical basis for understanding differ-

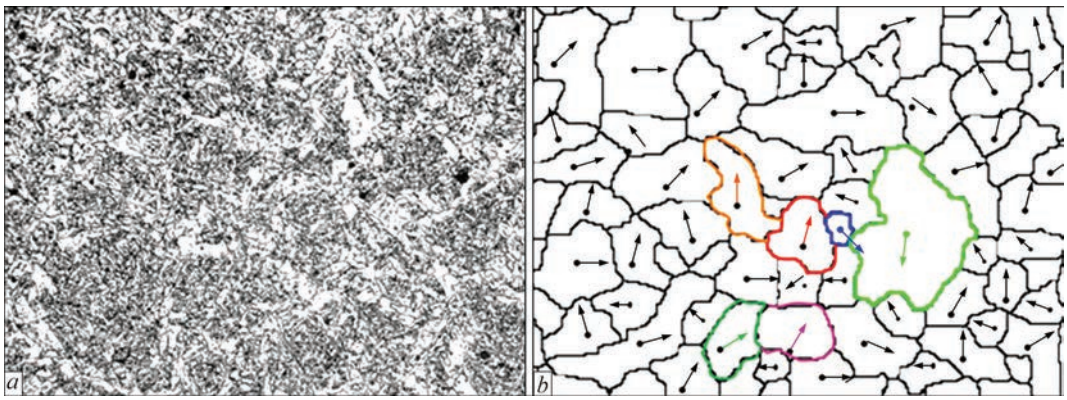

Figure 3. Microstructure of the base weld metal of 09G2S steel (×200) (*a*). Results of determining the principal orientation direction of structural grains and examples of misorientation of the principal vector of two adjacent grains at an angle not exceeding 15° (*b*)

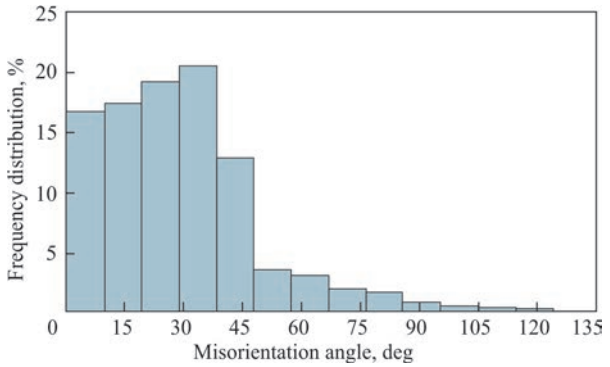

Figure 4. Distribution of misorientation angle at the boundary of two adjacent grains in the weld metal structure

ences in the mechanical properties of metal and allow high-throughput statistical analysis of these relationships. Another important aspect of EBSD is the determination of grain orientation angles in polycrystalline material, which define crystal orientation relative to the reference coordinate system. Determination of orientation angles allows obtaining a more accurate relationship between microstructural characteristics of the metal and its mechanical properties. Based on [21], EBSD can be effectively used for feature extraction and quantitative statistical analysis of microstructural information, and machine learning methods can become the foundation for establishing the relationship between microstructure and metal properties.

It should be noted that the EBSD method can be implemented on an electron microscope and requires installation of specialized software for processing Kikuchi patterns. As an alternative, a method based on Hough transformations can be considered, which allows detecting angular orientations of crystallographic planes in the microstructure. The Hough transformation calculation program is freely available, and in this case, the analysis is performed on images of metallographic structures obtained with optical microscopes. Such an approach can be used to determine not only the overall pattern of grain or crystal orientation angle distribution in the metal structure, but also at intergranular boundaries, which are among the most probable origines for brittle fracture nucleation. Exactly at these boundaries the possibility of crack transition from one grain to another or a change in its propagation direction is determined. According to this methodology, a computer program [22, 23] identifies each ferrite plate in the microstructure image, determines its area and the coordinates of the plane center, draws the maximum diagonal through the center, constructs a perpendicular to this diagonal, and determines the angle of its intersection with a specified axis (for example, the abscissa axis). Thus, each ferrite plate in the image is described by two parameters — ρ and θ (ρ is the distance from the origin to the line, and θ is the angle between the line perpendicular to the specified one and the positive direction of the abscissa axis). However, such an approach, considering the density distribution of ferrite plates in the grains of structural constituents of low-alloy steels, requires processing and analysis of a large volume of information. Modern computer analysis methods involving AI allow solving this problem.

An attempt to use the Hough transformation for metallographic studies of the weld metal microstructure of HSLA steel was described in [24]. The authors implemented a visual method for analyzing the orientation and misorientation of microstructural constituents using the Python programming language. Using AI, the position of the principal orientation vector of each structural grain was found (Figure 3) based on the Principal Component Analysis (PCA) method, which allows determining the main direction of grain orientation.

Based on this analysis, statistical data on grain misorientation angles were obtained (Figure 4), enabling analysis of the studied zone for the presence of such a critical parameter as the relative density distribution of LAGBs in the metal microstructure.

The permissible limits of grain misorientation in metallic structures depend on the specific material, its operating conditions, and manufacturing technology.

As can be seen from the data presented in Figure 4, approximately 20 % of boundaries between adjacent structural grains are characterized by a misorientation angle of no more than 35°. Such grain boundaries in-

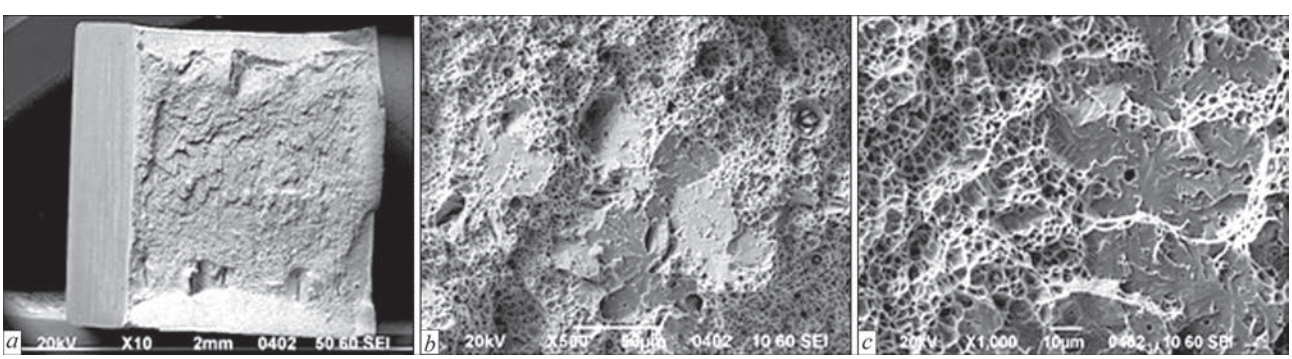

Figure 5. Fractographs of fracture surface of 09G2S steel weld metal specimen after impact bending test at a temperature of –20 °C

hibit crack propagation along grain boundaries and promote transcrystalline fracture. Figure 5 shows images of fractographs of a weld metal specimen fractured during impact bending tests at a temperature of –20 °C, which were obtained using a Jeol JSM35CF scanning electron microscope (Jeol, Japan). As can be seen from these images, the nature of crack propagation indicates precisely such a fracture process development — approximately one-third of cracks in this case have a transgranular nature.

Despite the agreement between the determination of misorientation angles at intergranular boundaries of the microstructure and the results of fractal analysis, such data are insufficient to establish a critical level of LAGB density in the metal microstructure as a "brittleness criterion". Such conclusions will only be possible after accumulating a substantial database of experimental data, their statistical processing, and through analysis. This should be the task of future research, the results of which will provide an opportunity not only to expand our knowledge base regarding the mechanisms of metal microstructure formation, but also to increase the level of mechanical properties of welded joints in HSLA steels.

CONCLUSIONS

A limiting factor in the adoption of modern high-strength low-alloy steels is their susceptibility to defect formation resulting from welding, which occurs during the welding process. Therefore, a fundamental aspect of developing their welding technology is understanding how metal properties change during the welding process and identifying the main microstructural characteristics that explain these changes.

When determining the influence of structural parameters on the properties of weld metal, it is necessary to consider such specific factors as differences in the orientation of ferrite precipitates within the body of structural grains.

The metallographic analysis method using Hough transformation, which can be implemented on optical microscopes, does not require specialized software on one hand, and allows determining the orientation of ferrite plates within the body of structural grains and, accordingly, the misorientation angle at the boundary of two contacting grains on the other hand, and should be considered as an alternative to the EBSD method.

Simplification of the procedure, through the use of AI tools, for determining structural grain orientation angles and misorientation angles at intergranular boundaries significantly increases the database of experimental data for establishing the critical level of LAGB density in metal microstructure as a "brittleness criterion".

The obtained results can be used in developing technological solutions when, in addition to structural grain size, attention is paid to forming a mixed microstructure with a balanced distribution of low-angle and high-angle grain boundaries, which will allow increasing both the strength and toughness of weld metal.

REFERENCES

1. Hall, E.O. (1951) The deformation and ageing of mild steel: III Discussion of results. *Proc. Phys. Soc. B*, 64(**9**), 747–753. DOI: http://doi.org/10.1088/0370-1301/64/9/303
2. Petch, N.J. (1953) The cleavage strength of polycrystals. *J. Iron Steel Inst*., **174**, 25–28.
3. Chapetti, M., Miyata, H., Tagawa, T. et al. (2004) Fatigue strength of ultra-fine grained steels. *Mater. Sci. Eng. A*, **381**, 331–336. DOI: https://doi.org/10.1016/j.msea.2004.04.055
4. Hansen, N. (2004) Hall–Petch relation and boundary strengthening. *Scr. Mater.,* **51**, 801–806. DOI: https://doi.org/10.1016/j.scriptamat.2004.06.002
5. Yang, X.L., Xu, Y.B., Tan, X.D., Wu, D. (2014) Influences of crystallography and delamination on anisotropy of Charpy impact toughness in API X100 pipeline steel. *Mater. Sci. Eng. A*, **607**, 53–62. DOI: https://doi.org/10.1016/j.msea.2014.03.121
6. Joo, M.S., Suh, D.-W., Bae, J.H., Bhadeshia, H.K.D.H. (2012) Toughness anisotropy in X70 and X80 pipeline steels. *Mater. Sci. Eng. A*, **556**, 601–606. DOI: http://dx.doi.org/10.1179/1743284713Y.0000000371
7. Jabr, H.M.A., Speer, J.G., Matlock, D.K. et al. (2013) Anisotropy of mechanical properties of API X70 spiral welded pipe steels. *Mater. Sci. Forum*, **753**, 538–541. DOI: http://dx.doi.org/10.4028/www.scientific.net/MSF.753.538
8. Sanchez, N., Petrov, R., Bae, J.H., Kim, K. (2010) Texture dependent mechanical anisotropy of X80 pipeline steel. *Adv. Eng. Mater*., **12**, 973–980. DOI: http://dx.doi.org/10.1002/adem.201000065
9. Cheng, S., Zhang, X., Zhang, J. et al. (2016) Effect of start cooling temperature on microstructure and properties of X80 pipeline steel. *Mater. Sci. Eng. A*, **666**, 156–164. DOI: https://doi.org/10.1016/j.msea.2016.04.066
10. Herbig, M., Raabe, D., Li, Y.J. et al. (2014) Atomic-scale quantification of grain boundary segregation in nanocrystalline material. *Physical Review Letters*, **112**, 126103. DOI: https://doi.org/10.1103/PhysRevLett.112.126103
11. Duan, Q., Yan, J., Zhu, G.H., Cai, Q.W. (2013) Effects of grain size and misorientation on anisotropy of X80 pipeline steel. *Hot Working Tech*., **24**, 107–109. https://caod.oriprobe.com/articles/41006381/Effects_of_Grain_Size_and_Misorientation_on_Anisot.htm
12. Masoumi, M., Silva, C.C., Abreu, H.F.G.D. (2018) Effect of rolling in the recrystallization temperature region associated with a post-heat treatment on the microstructure, crystal orientation, and mechanical properties of API 5L X70 pipeline steel. *J. Mater. Eng. Perfor*., **27**, 1694–1705. DOI: http://dx.doi.org/10.1590/1980-5373-mr-2016-0651
13. Deng, C.M., Li, Z.D., Sun, X.J., Yong, Q.L. (2014) Influence mechanism of high angle boundary on propagation of cleavage cracks in low martensite steel. *Mater. Mech. Eng*., **38**, 20–24.
14. Shen, J.C., Luo, Z.J., Yang, C.F., Zhang, Y.Q. (2014) Effective grain size affecting low temperature toughness in lath structure of HSLA steel. *J. Iron Steel Res. Int*., **26**(**7**), 70–76.
15. Hussein, A., Kim, B., Verbeken, K., Depover, T. (2024) The effect of grain boundary misorientation on hydrogen flux

using a phase-field based diffusion and trapping model. *Advanced Eng. Materials*, 26(**22)**, 2401561. DOI: https://doi.org/10.1002/adem.202401561
16. Raabe, D., Herbig, M., Sandlöbes, S. et al. (2014) Grain boundary segregation engineering in metallic alloys: A pathway to the design of interfaces. *Current Opinion in Solid State and Materials Sci.*, **18**, 253–261. DOI: https://doi.org/10.1016/j.cossms.2014.06.002
17. Stojanovic, N., Glisovic, J., Abdullah, O.I. et al. (2022) Particle formation due to brake wear, influence on the people health and measures for their reduction: A review. *Environ Sci. Pollut. Res.,* **29**, 9606–9625. DOI: https://doi.org/10.1007/s11356-021-17907-3
18. Vincentis, N.S., Roatta, A., Bolmaro, R.E., Signorelli, J.W. (2019) EBSD analysis of orientation gradients developed near grain boundaries. *Materials Research*, 22(**1**), e20180412. DOI: https://doi.org/10.1590/1980-5373-MR-2018-0412
19. Pauli, L., Heikki, R. (2022) EBSD characterisation of grain size distribution and grain sub-structures for ferritic steel weld metals. *Welding in the World*, **66**, 363–377. DOI: https://doi.org/10.1007/s40194-021-01225-w
20. Hwang, B., Kim, Y.G., Lee, S. et al. (2005) Effective grain size and Charpy impact properties of high-toughness X70 pipeline steels. *Metallurgical and Materials Transact. A*, **36**, 2107–2114. DOI: https://doi.org/10.1007/s11661-005-0331-9
21. Stojanovic, N., Belhocine, A., Abdullah, O.I., Grujic, I. (2023) The influence of the brake pad construction on noise formation, people's health and reduction measures. *Environ Sci. Pollut. Res.*, **30**, 15352–15363. DOI: https://doi.org/10.1007/s11356-022-23291-3
22. Li, X.C., Zhao, J.X., Cong, J.H. et al. (2021) Machine learning guided automatic recognition of crystal boundaries in bainitic/martensitic alloy and relationship between boundary types and ductile-to-brittle transition behavior. *J. Mater. Sci. Technol.,* **84**, 49–58. DOI: https://doi.org/10.1016/j.jmst.2020.12.024
23. Atiquzzaman, M. (1992) Multiresolution Hough transform an efficient method of detecting patterns in images. *IEEE Transact. on Pattern Analysis and Machine Intelligence*, 14(**11**), 1090–1095. DOI: https://doi.org/10.1109/34.166623
24. Zhuravel, I.M., Maksymovych, V.M. (2018) Quantitative analysis of orientation and elongation of grains on metallographic images using Hough transformations. *Naukovyi Visnyk NLTU Ukrainy*, 28(**5**), 135–139 [in Ukrainian]. DOI: https://doi.org/10.15421/40280528

ORCID
V.V. Holovko: 0000-0002-2117-0864,
O.O. Shtofel: 0000-0003-0965-6340,
D.Yu. Korolenko: 0009-0008-8582-5904

CONFLICT OF INTEREST
The Authors declare no conflict of interest

CORRESPONDING AUTHOR
V.V. Holovko
E.O. Paton Electric Welding Institute of the NASU
11 Kazymyr Malevych Str., 03150, Kyiv, Ukraine.
E-mail: v_golovko@ukr.net

SUGGESTED CITATION
V.V. Holovko, O.O. Shtofel, D.Yu. Korolenko (2025) Use of the Hough transformation method for the metallographic studies of ferritic-bainitic steels microstructure. *The Paton Welding J.*, **11**, 35–40. DOI: https://doi.org/10.37434/tpwj2025.11.05

JOURNAL HOME PAGE
https://patonpublishinghouse.com/eng/journals/tpwj

Received: 21.02.2025
Received in revised form: 16.07.2025
Accepted: 18.11.2025

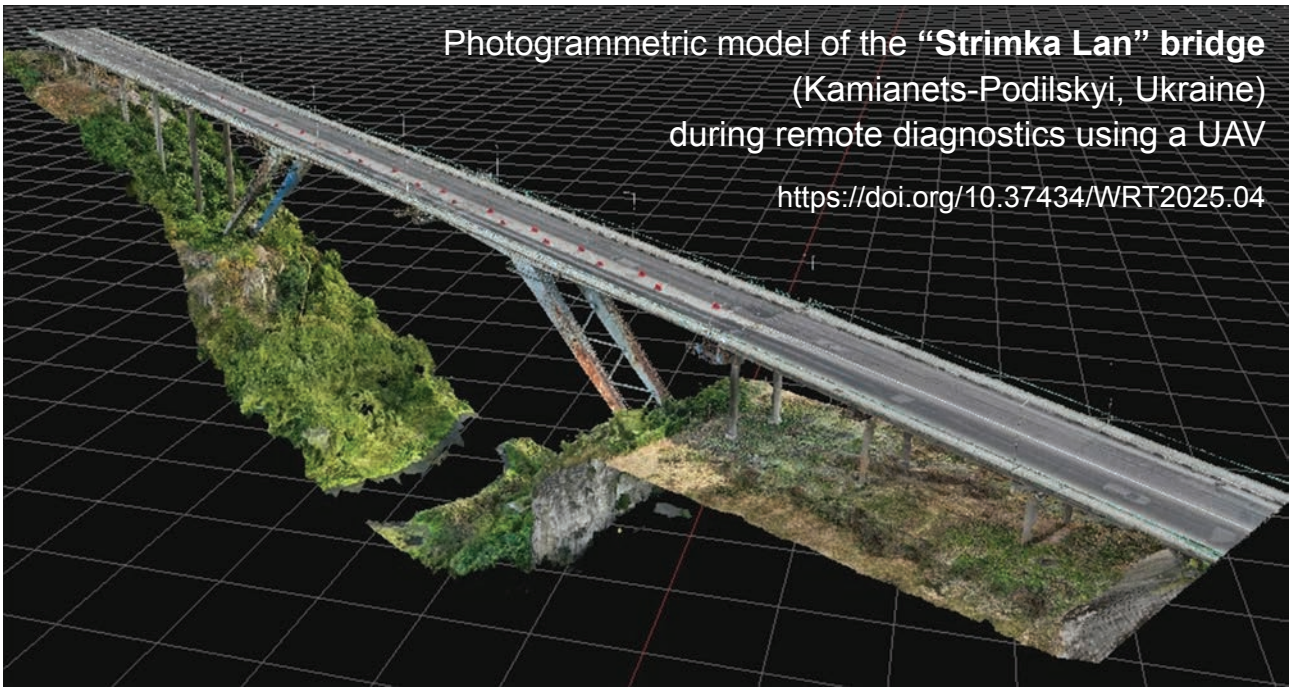

DOI: https://doi.org/10.37434/tpwj2025.11.06

EXPERIMENTAL STUDIES OF MEASURING COMBINED ULTRASONIC STRAIGHT ELECTROMAGNETIC-ACOUSTIC TRANSDUCERS WITH PULSED MAGNETIZATION

G.M. Suchkov, M.E. Kalnytskyi, A.V. Donchenko, O.I. Kurando, A.H. Aleksiiv, O.M. Borodenko, O.I. Butenko, A.O. Rybalko

National Technical University "Kharkiv Polytechnic Institute"
2 Kyrpychova Str., 61002, Kharkiv, Ukraine

ABSTRACT

At present, a wide variety of designs for electromagnetic-acoustic transducers (EMATs) are known, which are intended for measurements, quality control, and diagnostics of materials and products. Such transducers generate and receive pulses of all known ultrasonic wave types in metal products, both ferromagnetic and non-ferromagnetic. Recently, there has been intensive development of transducers that use powerful pulsed magnetic fields. On one hand, these are structurally more complex under the same conditions, but on the other hand, they offer a significant advantage when measuring characteristics of ferromagnetic objects, since they practically eliminate mutual attraction forces. The complexity of EMAT designs with pulsed magnetization necessitates research into optimal parameters and the application of new operating methods, considering the simultaneous interaction of dynamic magnetic and high-frequency electromagnetic fields in the surface layer of the metal product — during both the excitation and reception of ultrasonic wave pulses. It is especially important to account for such interaction in widely used measuring combined ultrasonic straight EMATs with pulsed magnetization. Therefore, it is advisable to conduct mandatory experimental studies to determine the optimal parameters, as the available theoretical works do not provide sufficiently accurate results needed for the development of technologies and the design of new measurement and control tools operating with pulsed magnetization.

KEYWORDS: experimental research, ferromagnetic product, ultrasonic pulses, electromagnetic-acoustic, measurement, control, diagnostics, magnetic field, electromagnetic field, pulsed magnetization

INTRODUCTION

Ultrasonic methods of measurement, quality control and diagnostics are the most common in non-destructive testing (NDT) [1, 2]. Traditional testing using a couplant is not always acceptable, as it requires constant costs for cleaning the surface of the tested object and the couplant [3, 4]. The state of the environment also deteriorates [2, 4].

Application of electromagnetic-acoustic (EMA) methods and means of NDT allows greatly improving the situation [5–9]. However, application of EMA transducers (EMAT) with constant magnetization [5, 10], when studying the quality of ferromagnetic tested objects (TO) leads to EMAT damage, because of strong mutual attraction and excitation of coherent interference from the ferromagnetic particles, for instance scale. EMAT with pulsed magnetic fields allow solving the above problems [11–17]. Such devices, however, have their drawbacks [15, 17]: dynamic interaction of the pulsed magnetic field and the high-frequency magnetic field in time and space is insufficiently investigated; design and technological parameters of EMA transducers and their power supply devices, which significantly affect the testing results, are insufficiently studied; optimal values of the design and technological parameters are not established, primarily by experimental methods. This is particularly important for instruments with portable combined straight EMATs for thickness measurement and testing of ferromagnetic TO by pulses of shear ultrasonic waves [9, 15], both during their manufacture and during operation in the enterprises and in the field conditions [17].

THE OBJECTIVE OF THE RESEARCH

is to improve the EMAT for portable ultrasonic devices during excitation and reception of pulses of shear ultrasonic waves normal to the surface of ferromagnetic TO due to pulsed magnetization.

EXPERIMENTAL RESEARCH OF A DEVICE FOR PULSED MAGNETIZATION AS PART OF A MODEL OF COMBINED STRAIGHT EMAT FOR EXCITATION AND RECEPTION OF SHEAR PACKET ULTRASONIC PULSES NORMAL TO THE SURFACE OF THE FERROMAGNETIC METAL PRODUCT

In [18] it was shown that in case of application of a source of a constant magnetic field made in the form of a parallelepiped, its optimal height should be close to 60 mm, and the size of the pole turned to the TO,

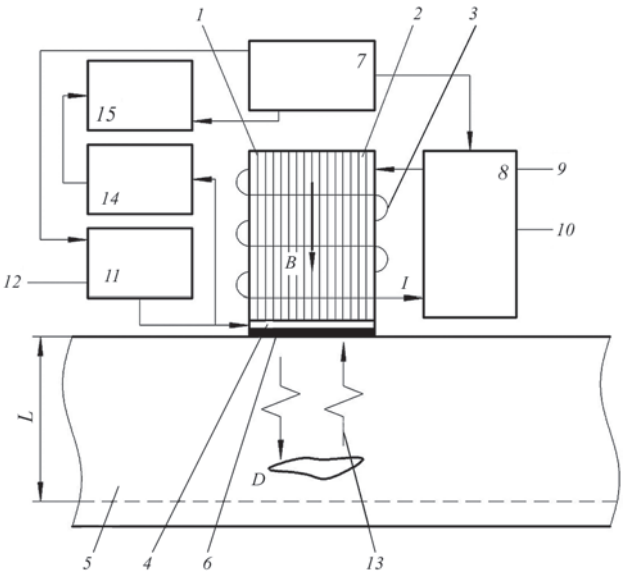

Figure 1. A simplified model of portable ultrasonic device for studying the characteristics of EMAT and its elements

should be in the range of 30×30–50×50 mm^2. Accordingly, in [14] it is shown by simulation that with pulsed magnetization when ensuring a quasistationary time of the magnetic field impact during a specified interval the results of [18] as to the sizes of the pulsed magnet core can be used. Such conclusions, however, should be confirmed experimentally. For this purpose, a special stand was developed [19], which envisages regulation of the main characteristics of EMAT with pulsed magnetization during the research performance. The high-frequency part of the stand remains the same as for EMA transducer with a constant magnetic field [3, 5, 18].

The proposed approach can be realized using an experimental portable device, a simplified model of which is given in Figure 1, where: *1* is the pulsed magnet; *2* is the laminated core of the pulsed magnet made from insulated from each other ferromagnetic plates with a high saturation inductance; *3* is the magnetization coil; *4* is the flat high-frequency induction coil; *5* is the ferromagnetic electrically conducting metal product; *6* is the local area of the surface layer of the metal product, in which ultrasonic pulses are excited and received from TO, accordingly; *7* is the synchronizer; *8* is the supply unit of the magnetization coil *3*; *9* is the regulator of setting the time of the beginning of the magnetization pulse; *10* is the regulator of setting the time of the end of the magnetization pulse; *11* is the generator of powerful high-frequency packet pulses of supply current of the high-frequency induction coil *4*; *12* is the regulator of clock position of the high-frequency packet pulses of supply current of the high-frequency induction coil relative to the time of the beginning of the magnetization pulse; *13* are the ultrasonic pulses, which propagate in the volume of TO *5*; *14* is the amplifier of the received ultrasonic pulses *13*; *15* is the block of data processing, recording and displaying; *L* is the distance from area *6* of the surface with the excited pulsed magnetic field to the end of the ultrasonic testing zone in the volume of TO *5*; *I* is the current in coil *3* of pulsed magnet *1*; *B* is the magnetic field induction; *D* is the defect in the volume of the ferromagnetic electrically conducting metal product being tested.

Considering the above, we will choose the dimensions of the pulsed magnet laminated core of 36×36×60 mm^3 from the above-mentioned range. Here, it should be noted that manufacturing a laminated core of the pulsed magnet leads to reduction of the coefficient of its filling with metal. Accordingly, this factor will lead to reduction of the magnitude of the induction of the forming magnetic field. A contradiction arises: on the one hand bringing the laminated magnet core closer to a flat high-frequency coil should enhance the magnetic field induction in the TO surface, and on the other hand the core lamination leads to decrease in the magnetic field induction. The influence of this factor should be additionally studied experimentally.

In [11] it is shown that in order to shorten the time of the magnetization pulse increase, and accordingly, also reduce the power losses, the inductive component of the pulsed magnet should be minimal. Another contradiction arises. On the one hand, increase of the metal volume in the magnet core and of the number of the magnetization coil turns [17] enhances the magnet coil inductance, and on the other hand, in order to reduce the inductance of the magnetic field source, it is rational to reduce the number of turns in the magnetization coil. As we have determined the geometric dimensions of the pulsed magnet core, its parameters can be changed only due to the parameters of the magnetization coil, its position on the core and characteristics of the pulsed supply current. However, there is a contradiction here too. In [12] it is shown that the magnetization coil should enclose the core along its entire height of 60 mm. On the other hand, in keeping with the results of [11], the magnet core should be enclosed by the magnetization coil only partially, which reduces the inductance of the pulsed magnetic field source. Such a contradiction requires verification by experimental research into the height of the magnetization coil position relative to that of the core with all other conditions being the same.

Thus, it is necessary to experimentally study the influence of the following parameters on EMAT effectiveness: magnetization coil parameters; pulsed magnet supply voltage; relative time relationships of the magnetization pulse and the high-frequency signal, etc.

EXPERIMENTAL RESEARCH PROCEDURE

At the first stage a coil was wound on the pulsed magnet core with 1.2 mm wire with a lacquer coating up to filling along the entire height. Then the number of turns was reduced, as shown in Figure 2.

All together pulsed magnets with the number of turns of 45, 30, 15, 9 and 6 pcs were manufactured with copper wire of 1.2 mm diameter. When the number of turns was reduced, they were located in the lower part of the core, as proposed in [11]. Research was conducted on a specimen from 09G2S steel of 100×100×40 mm^3 size without cleaning the surfaces from scale. The degree of maximal roughness of the specimen surface was up to 0.5 mm in some areas.

The main criteria of the pulsed magnet effectiveness were determined as follows: magnitude of magnetomotive force [17] and duration of quasiconstant magnitude of the magnetic field, sufficient for excitation and reception of ultrasonic pulses from a ferromagnetic specimen of the specified thickness. In its turn, the values and duration of a quasiconstant magnitude of the magnetic field were clearly determined by the strength of current in the magnetization coil.

During investigations the pulsed magnet was placed with one pole plane on the specimen surface through a lavsan gasket 0.2 mm thick. A 30 V voltage was applied to the magnetization coil with a pulse of 400 μs duration through an electronic key. The current in the circuit was measured with a shunt from nichrome of 1 mm diameter with 0.13 Ohm resistance.

Examples of the shape and strength of current in the magnetization coil with different supply voltages of the discharge key circuit are given in Figure 3.

Analysis of the data, given in Figure 3, allows the following conclusions to be drawn. When the number of turns of the pulsed magnet winding is reduced, first, a "shelf" is gradually formed with time duration sufficient for TO measurement, control and diagnostics, and, secondly, the rate of current rise in the coil is significantly increased. That is, it is possible to shorten the magnetization pulse, and, accordingly, reduce

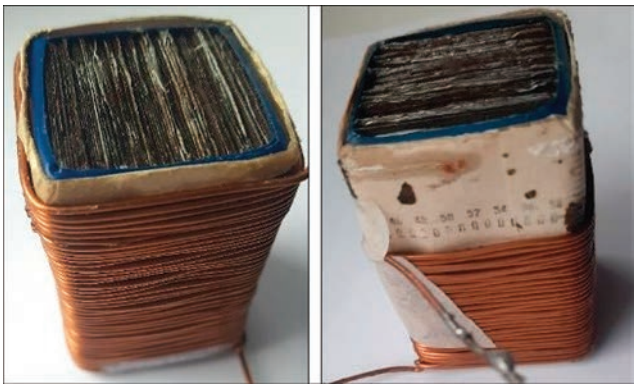

Figure 2. A pulsed magnet for EMAT with 36×36×60 mm^3 laminated core with winding of 45 and 15 turns from 1.2 mm copper wire

the consumption of the device battery power and optimize the pulsed magnet temperature mode.

It should be noted that it is not rational to shorten the duration of the magnetization pulse by reducing the capacitance of the discharge capacitors, as it is necessary to form the working "shelf" with the time duration, sufficient for taking the measurements of the TO parameters. Then, reduction of the magnetization coil inductance is possible practically only due to reduction of the number of turns of the magnet coil, with other conditions being equal, and it cannot be achieved through reduction of the volume of the magnet core metal as it is determined [3, 5, 19] by the dimensions of the working area of the EMAT high-frequency inductance coil which should be maximal possible [5].

Calculations of the magnetomotive force, which can be used in a certain approximation [17] showed that for the given variants of pulsed magnets MMF is equal to: for 45 turns — 1575, for 30 turns — 3090, for 15 turns — 6000; for 9 turns — 5965, and for 6 turns — 4800.

During experiment performance it was found that placing a small number of turns of the pulsed magnet magnetization coil along the entire core height yield a significant MMF increment. A magnetization coil from a thin wire overheats even at small numbers of probing

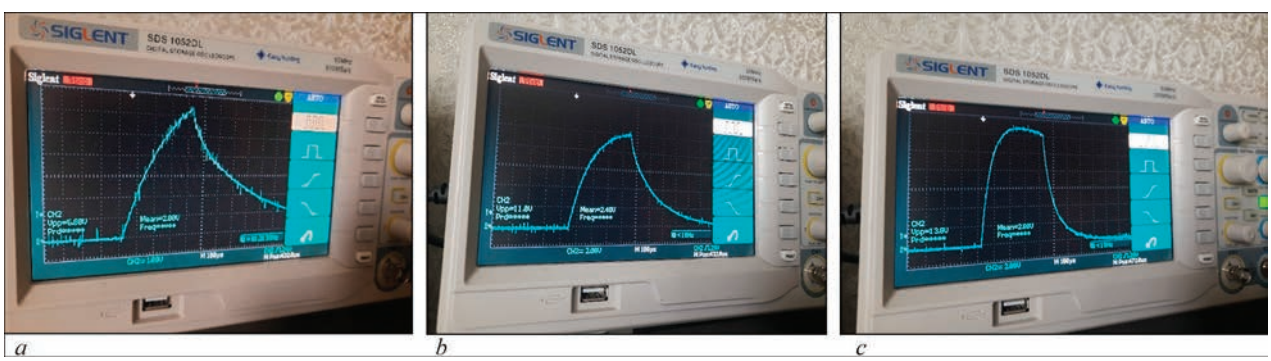

Figure 3. Signals equivalent to current in the pulsed magnet coils, depending on the number of turns of 1.2 mm wire in the core lower part: *a* — 15 turns; *b* — 9 turns; *c* — 6 turns

Figure 4. Pulsed magnet winding with 8.5 turns made from 60×0.5 mm^2 strip along the height of 60 mm of 36×36 mm^2 laminated core

Figure 6. Model of a pulsed magnet with a coil made from 10×1 mm^2 copper bus, 6.75 turns

pulses. Therefore, in order to eliminate the above factor, the induction coils were made from a copper strip 60 mm wide and 0.5 mm thick with the turn number of 8.5 (Figure 4) and from a copper strip 60 mm wide and 0.1 mm thick with the turn number of 5.75 pcs.

In order to measure the current in a magnetization coil with a low resistance, a specially produced shunt with the resistance of 0.4 mOhm was made, which was calibrated using a standard shunt 75ShSMM3-200-0.5 with the resistance of 0.375 mOhm. The resistance of the coil in Figure 4 which was measured at direct current with E6-15 milliohmeter was equal to 1.51 mOhm. Winding inductance is equal to 10 mH (measured with E7-22 instrument at 120 Hz frequency, which can be conditionally considered a close value to the fundamental frequency of pulsed current). The results of measurement of the strength of current, and, accordingly, of the magnetic field inductance of coils from strips of different thickness, are given in Figure 5 in case of application of 0.4 mOhm shunt.

Analysis of the data in Figure 5 shows that the maximal MMF for such magnetization coils is higher than 11000. With the number of turns close to 6 the working "shelf" of quasiconstant inductance of the magnetic field forms earlier. That is, it is necessary to reduce the number of the magnetization coil turns. Further reduction of the number of coil turns below 6 leads to decrease in the MMF value. Moreover, a disadvantage was revealed: the thermal mode of the pulsed magnet deteriorated, which is due to insufficient heat transfer by the coil internal turns and magnet core.

To preserve the MMF, reduce the resistance and improve the temperature mode, the magnetization coil was made from a 10×1 mm^2 copper bus (Figure 6). The inductance of the coil on the core was equal to 0.008 mH (measured at the frequency of 1 kHz). Resistance of the direct current coil was 40 mOhm. Such a magnetization coil was used for further research.

Influence of supply voltage of the key discharge stage on the results of current measurement is shown in Figure 7. Its maximal value in the working area was

a *b*

Figure 5. Voltage equivalent to current on 0.4 mOhm shunt with the pulsed magnet winding of: *a* — 8.5 turns from 60×0.5 mm^2 strip; *b* — 5.75 turns from 60×0.1 mm^2 strip. Supply voltage of the discharge key of 30 V

Figure 7. Current in the magnetization coil, equivalent to the magnetic field, when the key stage is powered by voltage of, V: *a* — 30; *b* — 20; *c* — 10. Magnetization pulse duration of 400 μs

equal to 2.5 kA. Accordingly, MMF has the value of approximately 16800, which is much higher than the value determined in [17], as sufficient for testing.

Comparative analysis of the results given in Figures 5 and 7 leads to the conclusion that in order to increase the MMF the number of turns in the magnetization coil should be close to 5–6 pcs. Shortening of the magnetization pulse enables saving the battery power of the portable devices and decreasing the thermal load on the pulsed magnet. Open surface of the coil in Figure 6 increases the heat transfer.

However, the main characteristic of EMAT with pulsed magnetization is the information signal amplitude [5, 11], by the magnitude of which the TO quality is determined. To measure the information (bottom) signal of the EMA pulse, the transducer was mounted so that the direction of ultrasonic pulse emission was normal to the specimen plane, i.e. measurement was conducted across a 40 mm thickness. Testing was performed through a lavsan gasket between the TO and EMAT 0.2 mm thick.

During research performance, the frequency of ultrasonic vibrations was equal to 2.3 MHz, the duration of the packet probing high-frequency pulse was 3 periods of the filling frequency, and the peak current strength in the flat high-frequency induction coil was 400 A. Supply voltage of the key stage of the stand (Figure 1) was equal to 30 V. The duration of the magnetization pulse was 400 μs. Measurement results are given in Figure 8.

Analysis of the results presented in Figure 8, confirms the high effectiveness of excitation and reception of ultrasonic pulses of EMA transducer with pulsed magnetization. The ratio of the amplitude of the first bottom pulse to that of interference is more than 30 times, which is more than sufficient for effective operation of the ultrasonic thickness meter [5] or flaw detector [3, 16]. Recoding of a significant number of bottom pulses is indicative of sufficient duration of the "working area" of current excited in the pulsed coil. It should be noted that the derived results were not processed by any method, i.e. they are preliminary.

During research performance, the influence of a very important factor was established. An acceptable value of bottom pulses is recorded by the oscillograph not immediately after the beginning of the magnetization pulse. First, the bottom pulses, depending on the delay of the time of excitation of the high-frequency pulse relative to the beginning of the magnetization pulse, are absent at the minimal level, and then their amplitude is gradually increased (Table 1).

During performance of research, 30 V supply voltage of the discharge key and 0.4 mOhm shunt were used for the magnetization coil with 5.75 turns of 60×10 mm^2 size. The formed "working shelf" of current in the pulsed magnet coil is effective, starting from 200 μs after the beginning of the magnetization pulse. Maximal amplitude of the high-frequency current pulse was equal to 400 A with the duration of 3 filling periods with the frequency of 2.3 MHz.

Thus, it is rational to choose the number of the magnetization coil turns close to 6 pcs with the laminated core of 60×36×36 mm^3 size, made from transformer steel with plates 0.5 mm thick or thinner, which ensures absence of coherent interference from the pulsed magnet core.

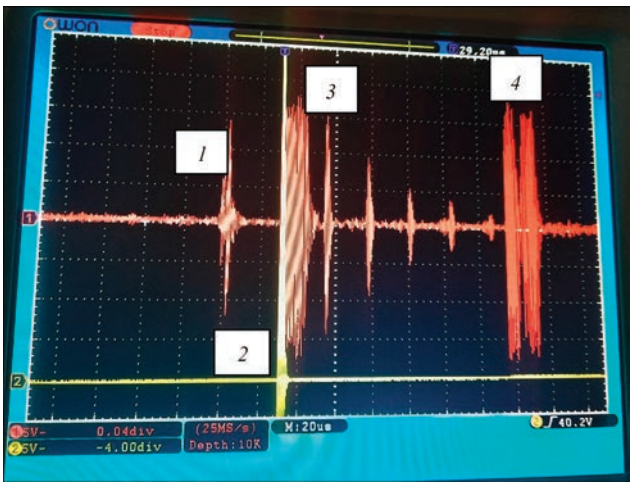

Figure 8. Time sweep with bottom pulses reflected from TO, obtained during operation of EMAT with pulsed magnetization on the screen of a dual-beam oscilloscope on a specimen from 09G2S steel 40 mm thick: *1* — induced signal of the magnetization pulse beginning; *2* — probing high-frequency packet pulse with the duration of 3 periods of filling frequency of 2.3 Hz; *3* — reflected from the specimen first bottom pulse, after which the second, third, fourth and fifth bottom pulses reflected in the TO, are successively recorded; *4* — induced signal from the magnetization pulse finesh

Table 1. Dependence of the amplitude of bottom pulses A_1 on the time of the high-frequency packet pulse delay relative to the beginning of the magnetization pulse of 400 μs duration when supplying 30 V voltage to the initial key stage

Parameter	Time of high-frequency pulse delay relative to the beginning of the magnetization pulse							
Delay time, μs	50	100	150	200	250	300	350	390
Amplitude of the first bottom pulse A_1 relative to interference level, times	8	18	26	34	34	34	34	34

Table 2. Dependence of the amplitude of bottom pulses A_1 and the maximum current in the magnetization coil on the key stage supply voltage with the magnetization pulse duration of 225 μs

Parameter	Parameter value					
Supply voltage of the initial key stage, V	5	10	15	20	25	30
Amplitude of the first bottom pulse, A, relative to interference level, times	2	10	19	28	32	36
Maximal current in the magnetization coil, A	325	775	1100	1600	2000	2250

Analysis of the data given in Table 1 also leads us to the conclusion about the rationality of shortening the magnetization pulse, which allows saving the battery power of the device and improving the pulsed magnet temperature mode.

The influence of the supply voltage of the key cascade on the investigation results under the previous conditions are given in Table 2. The duration of the magnetization pulse was reduced to 225 μs. The shape of such a magnetization pulse is shown in Figure 9.

Analysis of the data in Table 2 and in Figure 7 gives grounds to assert that increase of the supply power of the magnetization coil raises the rate of the pulsed magnetic field increase, which, in its turn, enables shortening the magnetization pulse. MMF increases to almost 13000 ampere-turns.

During performance of experimental research it was determined that the maximum of the magnetization current clearly correlates with the maximum of the magnetic field inductance in the surface layer of the metal, which determines the maximum of the amplitude of ultrasonic information (bottom) pulses.

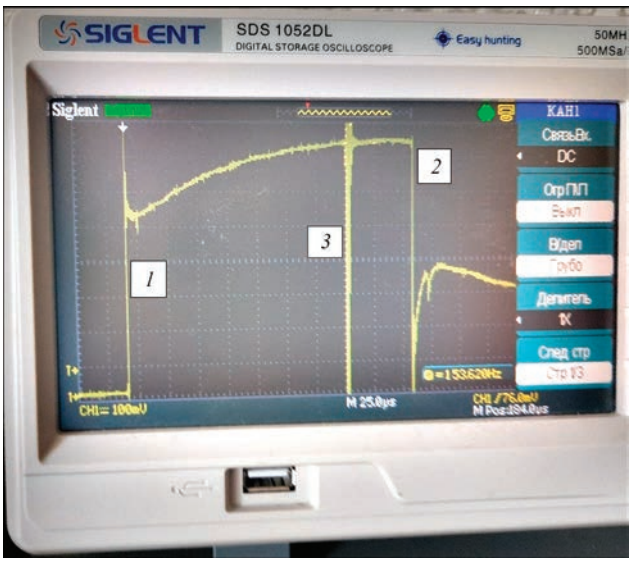

Figure 9. Shape of magnetization pulse of 225 μs duration with an induced high-frequency pulse: *1* — beginning of the magnetization pulse; *2* — end of the magnetization pulse; *3* — high-frequency pulse

An effective advantage of EMA transducers is the possibility of measurement and control through a layer of a dielectric coating, for instance, paint coating. The thickness of such a coating, as a rule, can reach 1–2 mm. That is why, the influence of dielectric interlayers between the EMAT and TO (Table 3), as well as between the pulsed magnet core and high-frequency induction coil was studied (Table 4). The thickness of the dielectric base, on which high-frequency coil is mounted, was 3 mm.

The data in Table 3 demonstrate that the influence of the distance between the EMAT and TO surface on the ultrasonic pulse amplitude is quite significant. However, at typical thicknesses of paint coatings of 0.1–0.3 mm, the EMAT of the developed type will be effective.

During performance of the above-mentioned research, the frequency of the high-frequency packet pulses was equal to 2.3 MHz, probing frequency was 4 Hz, the maximal current in the magnetization coil was 2250 A, number of periods of filling frequency in the packet pulse was 3, duration of the magnetization pulse was 225 μs, time of the high-frequency pulse delay relative to the beginning of the magnetization pulse was 175 μs, supply voltage of the initial key stage was 30 V.

Analysis of the data in Table 4 allows us to draw a conclusion that the distance from the pulsed magnet core to the high-frequency coil does not affect the magnitude of ultrasonic pulses that much. However, this distance should be set minimal. “Ringing” after the probing high-frequency pulse does not change with increase of the distance from the core to the high-frequency coil.

With increase of the thickness of the dielectric interlayer between the EMAT and TO from 0.2 to 1.7 mm the magnitude of ”ringing” becomes great-

Table 3. Influence of the dielectric interlayer thickness on the metal on the amplitude of the first ultrasonic bottom pulse

Parameter	Parameter value			
Thickness of the dielectric interlayer between the metal and EMAT, mm	0.2	1.5	2.2	3.7
Amplitude of the first bottom pulse A_1 relative to the interference level, times	34	28	26	24

Table 4. Influence of the thickness of the dielectric interlayer between the core and EMAT high-frequency induction coil on the amplitude of ultrasonic bottom pulses

Parameter	Parameter value						
Thickness of the dielectric interlayer between the core and the high-frequency induction coil, mm	0.2	0.4	0.6	0.8	1.0	1.2	1.7
Amplitude of the first bottom pulse A_1 relative to the interference level, times	34	34	32	32	30	30	26

Table 5. Influence of the duration of the high-frequency pulse packet on the amplitude of the ultrasonic bottom signal

Parameter	Parameter value					
Number of periods of filling frequency of the packet supply pulse of the high-frequency coil, pcs	1	2	3	4	5	6
Amplitude of the first bottom pulse A_1 relative to interference level, times	26	34	35	36	36	36

er, and the "dead zone" increases from 18 to approximately 35 mm, respectively. This is essential for evaluation of the quality of the metal product, so that it is necessary to develop devices for more effective inhibition of the amplitude and duration of "ringing".

Another parameter, which can affect the amplitude of ultrasonic pulses, is the duration of the high-frequency package, which is determined by the number of the filling frequency periods. The results of studying this parameter are given in Table 5.

Analysis of the data in Table 5 suggests that for excitation and reception of ultrasonic pulses it is sufficient to use a packet high-frequency pulse of the duration of 3 or more periods of frequency filling with the above-established magnitude and duration of the magnetization pulse.

CONCLUSIONS

A stand was developed for experimental research of the factors which determine the effectiveness of the device for ultrasonic testing of ferromagnetic materials during pulsed magnetization of EMAT.

Performed research showed that the useful signal value essentially depends on the clock position of the high-frequency pulse relative to the beginning of the magnetization pulse. The value of the high-frequency pulse delay should be determined experimentally for a specific ferromagnetic material of the TO.

It was proved that the pulsed magnet inductance should be minimal, and the magnetization coil resistance should also be minimal. As a result, the duration of the magnetization pulse does not exceed 200–300 μs, with the working part of the magnetization pulse which enables measurement, control and diagnostics of the ferromagnetic steel metal products up to 150–200 mm thick. For portable EMA instruments the consumption of supply power will be minimal.

It is shown that it is rational to manufacture an effective pulsed magnet of the EMA transducer from plates of transformer steel so that the plate planes were normal to the working part of the conductors of the high-frequency coil. It is rational to choose the core size of 30×30×60–50×50×60 mm^3. The number of turns in the pulsed magnet coil should be approximately equal to 6 pcs with conductor size of 10×1 mm^2.

Increase of the pulsed magnet supply voltage significantly shortens the time of the magnetic field increase, and, accordingly, reduces the duration of the magnetization pulse, which is important for maintaining the EMAT temperature mode.

REFERENCES

1. Liutak, I.Z. (2011) *Control of elastic properties of the metal wall of main pipelines by acoustic methods*: PhD Thesis. Ivano-Frankivsk [in Ukrainian].
2. Tsapenko, V.K., Kuts, Yu.V. (2010) *Fundamentals of ultrasonic nondestructive testing*: Textbook. Kyiv [in Ukrainian].
3. Pliesnetsov, S.Yu. (2021) *Development of methods and means for electromagnetic and acoustic inspection of rod, tube and sheet metal products*: PhD Thesis. Kharkiv[in Ukrainian].
4. Karpash, M.O., Rybitskyi, I.V., Koturbash, T.T. et al. (2012) *Acoustic control of structures and equipment in the oil and gas industry:* Monograph. Ivano-Frankivsk, IFNTUOG [in Ukrainian].
5. Desiatnichenko, O.V. (2015) *Electromagnetic and acoustic thickness gauge for inspection of metal products with dielectric coatings*: PhD Disc. Kharkiv [in Ukrainian].
6. NORDINKRAFT. The quality guard. www.nordinkraft.de

7. Kogia, M., Gan, T.H., Balachandran, W. et al. (2016) High temperature shear horizontal electromagnetic acoustic transducer for guided wave inspection. *Sensors*, 16(**4**), 582. DOI: https://doi.org/10.3390/s16040582
8. Mirkhani, K., Chaggares, C., Masterson, C. et al. (2004) Optimal design of EMAT transmitters. *NDT E Int.*, **37**, 181–193. DOI: https://doi.org/10.1016/j.ndteint.2003.09.005
9. Boughedda, H., Hacib, T., Chelabi, M. et al. (2015) Electromagnetic acoustic transducer for cracks detection in conductive material. In: *Proc. of 4th Inter. Conf. on Electrical Engineering (ICEE)*, 1–4. DOI: https://doi.org/10.1109/INTEE.2015.7416717
10. Suvorova, M.D. (2019) Development of magnetic sources for EMO converters on the basis of powerful permanent magnets. *Visnyk NTU KhPI. Seriia: Elektroenerhetyka ta Peretvoriuvalna Tekhnika*, **1**, 63–73 [in Ukrainian]. https://repository.kpi.kharkov.ua/server/api/core/bitstreams/b622d95b-faa3-4ee4-afce-ae6a33c54c67/content
11. Bussi Salam (2020) *Electromagnetic and acoustic transducers for ultrasonic inspection of metal products*: PhD Thesis, NTU KhPI [in Ukrainian].
12. Donchenko, A.V., Myhushchenko, R.P. Suchkov, H.M., Kropachek O.Yu. (2024) *Surface-mounted combined electromagnetic and acoustic transducer with pulse magnetization for control of ferromagnetic metal products*. Pat. UA for Utility Model 156088. Publ. 08.05.2024 [in Ukrainian].
13. Fortunko, C.N. Maclauchlan, D. *Pulsed electromagnets for EMATS*. Fracture and Deformation Division National Bureau of Standards Boulder, CO 80303.
14. Suchkov, H.M., Myhushchenko, R.P., Pliesnetsov, S.Yu. et al. (2024) Modelling of pulsed magnetic field sources of portable ultrasonic electromagnetic-acoustic transducers for measurement, control and diagnostics. *Metrolohiia ta Prylady*, **1**, 28–31 [in Ukrainian]. DOI: https://doi.org/10.30837/2663-9564.2024.1.06
15. Suchkov, H.M., Myhushchenko, R.P., Koshkarov, Yu.Yu. et al. (2023) The state of development of portable electromagnetic-acoustic transducers for measurement, control and diagnostics of ferromagnetic metal products (Review). *Podilskyi Visnyk: Silske Hospodarstvo, Tekhnika, Ekonomika. Silskohospodarski, Tekhnichni, Ekonomichni i Veterynarni Nauky*, 4(**41**), 54–61 [in Ukrainian]. DOI: https://doi.org/10.37406/2706-9052-2023-4.8
16. Suchkov, H.M., Donchenko, A.V. (2023) Improvement of electromagnetic-acoustic transducers for ultrasonic quality control of ferromagnetic metal products. In: *Abstr. of Papers of Inter. Sci. Inter. Conf. on Technological, Economic and Technical Aspects of Formation, 6–7 February 2023, Ternopil-Perevorsk*, **74**, 192–194 [in Ukrainian].
17. Suchkov, H.M., Myhushchenko, R.P., Pliesnetsov, S.Iu. et al. (2025) Increasing the sensitivity of electromagnetic-acoustic transducers for testing, measurement and diagnostics of ferromagnetic metal products via increase in the value of magnetic field induction (Overview). *Tekhnichna Elektrodynamika*, **2**, 85–95 [in Ukrainian]. DOI: https://doi.org/10.15407/techned2025.02.085
18. Bolyukh, V.F., Suchkov, G.M., Mygushchenko, R.P., Kalnytskyi, M.E. (2025) Determination of parameters of an autonomous source of a constant magnetic field for a portable electromagnetic-acoustic transducer. *Electrical Engineering & Electromechanics*, **4**, 72–79. DOI: https://doi.org/10.20998/2074-272X.2025.4.09
19. Suchkov, H., Kalnytskyi, M., Dmytrenko, M., Bobrov, O. (2025) Universal test bench and equipment for studying electromagnetic-acoustic transducers with a pulsed source of polarizing magnetic field. *Metody ta Prylady Kontroliu Yakosti*, 1(**54**), 13–28 [in Ukrainian]. DOI: https://doi.org/10.31471/1993-9981-2025-1(54)-13-28

ORCID

G.M. Suchkov: 0000-0002-1805-0466,
M.E. Kalnytskyi: 0009-0000-5056-2085,
A.V. Donchenko: 0009-0006-0559-0160,
O.I. Kurando: 0009-0008-6687-3126,
A.H. Aleksiiv: 0009-0001-1878-526X,
O.M. Borodenko: 0009-0001-1878-526X,
O.I. Butenko: 0009-0009-9636-8734,
A.O. Rybalko: 0009-0003-9560-4404

CONFLICT OF INTEREST

The Authors declare no conflict of interest

CORRESPONDING AUTHOR

G.M. Suchkov
National Technical University
"Kharkiv Polytechnic Institute"
2 Kyrpychova Str., 61002, Kharkiv, Ukraine.
E-mail: suchkov@gmail.com

SUGGESTED CITATION

G.M. Suchkov, M.E. Kalnytskyi, A.V. Donchenko, O.I. Kurando, A.H. Aleksiiv, O.M. Borodenko, O.I. Butenko, A.O. Rybalko (2025) Experimental studies of measuring combined ultrasonic straight electromagnetic-acoustic transducers with pulsed magnetization. *The Paton Welding J.*, **11**, 41–48. DOI: https://doi.org/10.37434/tpwj2025.11.06

JOURNAL HOME PAGE

https://patonpublishinghouse.com/eng/journals/tpwj

Received: 07.07.2025
Received in revised form: 07.08.2025
Accepted: 18.11.202